Spectroscopy and Wavelength Conversion by Four-Wave Mixing in Semiconductor Optical Amplifiers

Thesis by

Guido H. Hunziker

In Partial Fulfillment of the Requirements

for the Degree of

Doctor of Philosophy

California Institute of Technology

Pasadena, California

1998

(Defended May 12, 1998)

To Veronique

And To My Family

Acknowledgments

My deep gratitude goes to my advisor, Prof. Kerry Vahala, for providing such a generous and inspiring environment for my graduate work. His talents as a mentor, scientist and teacher are genuine and unique. Learning and working with him has been the most enriching and fruitful experience.

Most of the work presented in this thesis was done in collaboration with Roberto Paiella. I am very grateful to him for the excellent collaboration and the good time we have had working together for the past four years. My special thanks go to Alessandro D'Ottavi, David Geraghty, Robert Lee, and Jianhui Zhou for the stimulating discussions and for sharing their expertise with the system experiments. Other members of the Vahala group helped me make my Ph.D. pursuit enjoyable and rewarding : Prof. Minyu Yao, Masashi Fukazawa, Dr. Charles Tsai, Dr. Renato Camata, Elizabeth Boer, Dr. David Dougherty, Ashish Bhardwaj, Ming Cai and Michael Shumway. I would also like to thank Rosalie Rowe for her help with administrative matters.

Outside of the Vahala group, my deep gratitude goes to Paul Bridger, a friend with whom I have shared many enlightening and fruitful discussions and who accepted to proofread this thesis. My appreciation also goes to Jana Mercado, Linda Dosza, Ali Ghaffari, Larry Begay, Rey Johnson and the members of Prof. Atwater's group for their help in various situations.

I would further like to say thank you to Dr. Norman Kwong and Dr. Thomas Schranz from Ortel Corp. for sharing their expertise as well as for letting us use their DFB lasers, rf-amplifiers and detectors. Special thanks are due to Dr. Uzi Koren

at Lucent for the SOAs used in most of this work. I would also like to thank Dr. James Whiteaway from Nortel, for the stimulating discussions we had in Haifa and for generously donating SOAs for our research. Thanks also to Dr. Marc Verdiell and Dr. Mehrdad Ziari from SDL Inc. for providing the fiber pigtailed Bragg grating devices as well as their expertise for some of our experiments.

I am extremely grateful to Dr. Chris Harder at Uniphase Corp. for his advice and friendship, for encouraging me to come to Caltech as well as for his help during my graduate years. Thanks also to my great friends from Switzerland and California and for their support: Denis and Sandra Poffet, Yann and Barbara Caloz-Sartori, Edouard Bugnion, Andre and Agnes Simon, Amish Desai, Bill and Elaine Butler.

I am immensely grateful to my parents and to my sister for their unconditional patience, support and encouragement through the many years of my education.

My deepest thanks, of course, go to Veronique, for the love, the fun and the good life we have had in the past few years. Her support, understanding and encouragement in the past years were the greatest.

Abstract

The first part of this thesis is dedicated to the study of the physics of the four-wave mixing (FWM) optical non-linearity in semiconductor optical amplifiers (SOAs). We focus our attention on the polarization properties of FWM and spectroscopic measurements of ultrafast carrier dynamics in these amplifiers. The second part presents investigations of FWM applications in the context of high-speed optical communication systems.

The detuning and polarization dependence of the third-order non-linear susceptibility is presented with a model based on the density matrix formalism. Experimental verifications of the model for the polarization properties of the four-wave mixing are presented using an alternating compressive and tensile strained multiquantum-well semiconductor optical amplifier. The polarization selection rules are then used for spectroscopic measurements of the carrier dynamics in quantum well SOAs. In particular, we present new techniques to measure the stimulated carrier lifetime, the inter quantum-well transport lifetime as well as the intrinsic escape and capture time constants for quantum wells. The capture lifetime is further studied in a separate experiment involving wavelength resolved spectroscopy.

We then demonstrate that strongly saturated and long SOAs (1.5 mm) are very effective wide span wavelength converters. We present bit error rate measurements for 30 nm wavelength down-conversion and 15 nm wavelength up-conversion at 10 Gb/s. We also present an application of the polarization selection rules to generate a polarization independent conversion at 2.5 Gb/s. Then, we introduce two different

configurations where we use a lasing optical amplifier with a fiber Bragg grating to enhance the conversion efficiency and simplify the converter design. In the first case, we used the laser mode as pump wave and in the second case the lasing mode is injection locked to the FWM signal generated within the cavity. Finally, we present a new paradigm to perform wavelength encoded logic operations on a byte-wide WDM bus. Again, we use the polarization properties of the FWM to perform the logic operations.

Contents

List of Figures

Chapter 1

Introduction

In the past years, research and development efforts on semiconductor optical amplifiers have shifted their focus from the linear to the non-linear operation regime. In the 1.55 μm telecommunication wavelength range, the supremacy of Erbium doped fiber amplifiers as linear repeaters is so strong that semiconductors are almost exclusively considered for non-linear applications in these systems. Wavelength conversion is currently the most common system application in this context, but more sophisticated signal processing functions have been demonstrated. Another important aspect of the study of optical non-linearities in semiconductor optical amplifiers is spectroscopy and the study of ultrafast carrier dynamics in these devices. This work is aimed at a better understanding of the physics underlying the operation of these devices, both for laser and amplifier applications.

This thesis investigates the four-wave mixing (FWM) non-linearity in InGaAs/ InGaAsP semiconductor optical amplifiers (SOAs). There are two objectives for this work, the first is the study of ultrafast relaxation mechanisms in these semiconductors,

and the second, to demonstrate system level applications of FWM for wavelength conversion and all-optical signal processing. In particular, we are focusing on the polarization properties of the four-wave mixing. The results of this study are applied to spectroscopic investigations of semiconductors and practical system applications.

Chapter 2 contains a theoretical model for the four-wave mixing non-linearity, based on the density matrix formalism. We show how the different relaxation mechanisms contribute to the third order susceptibility and explain its structure in terms of a simple physical picture.

Chapter 3 is focused on the polarization properties of the mixing, and we explain how the polarization selection rules affect the conversion efficiency for arbitrary polarizations of the input waves. The physical explanation of the selection rules is given as well as experimental verifications of our model.

Chapter 4 shows how the polarization selection rules can be used in spectroscopic four-wave mixing experiments to investigate recombination and transport dynamics in the active region of the semiconductor. We present the results of measurements of the stimulated carrier lifetime, the inter quantum-well transport lifetime as well as the quantum escape and capture rates.

Chapter 5 introduces wavelength resolved four-wave mixing, and the result of an experiment to further investigate the capture process in quantum well structures. In the second part of this chapter, below-gap wavelength resolved four-wave mixing is used to measure the contribution to four-wave mixing due to carrier heating by free carrier absorption.

Chapter 6 presents results of a broad-band wavelength conversion system experiment where we demonstrate wavelength conversion of a digitally modulated signal at 10 Gb/s over a 30 nm range. Further, we present a polarization independent dual-pump four-wave mixing configuration and use this to convert the wavelength of a signal at 2.5 Gb/s.

Chapter 7 describes a new four-wave mixing device where the pump is internally generated through laser oscillation with a fiber pigtailed Bragg grating. This very simple wavelength conversion device is analyzed and used to shift a signal at 2.5 Gb/s by 9 nm with very low input power requirements. In a different configuration, we show how this device can produce very high conversion efficiency and signal to noise by resonnantly enhanced conversion through injection locking.

Finally, in chapter 8, we describe a new method to perform ultra-fast all-optical logic operations on a wavelength multiplexed optical bus using four-wave mixing.

The work presented in this thesis is contained in the published articles and conference proceedings given at the end of this chapter.

Bibliography

[1] G. Hunziker, R. Paiella, U. Koren, and K. J. Vahala, "Four-Wave Mixing Mediated by the Capture of Carriers in Semiconductor Quantum-Well Amplifiers," to be presented at the *Conference on Laser and Electro-Optics*, San Francisco, California, May 3–8, 1998, paper CThR3.

[2] R. Paiella, G. Hunziker, M. Ziari, A. Mathur, and K. J. Vahala, "Resonance Enhancement of the Four-Wave Mixing Efficiency by Injection Locking in a Fiber-Bragg-Grating Coupled Semiconductor Laser," to be presented at the *Conference on Laser and Electro-Optics*, San Francisco, California, May 3–8, 1998, paper CWC5.

[3] K. J. Vahala, R. Paiella, G. Hunziker, and U. Koren, "Direct Measurement of Capture and Escape Rates in Quantum Well Active Layers," *OSA Victoria Topical Meeting on Integrated Photonics Research*, Victoria, British Columbia, Canada, March 29–April 1, 1998, paper ITuG4 (**Invited Paper**).

[4] G. Hunziker, R. Paiella, A. D'Ottavi, P. Spano, R. Dall'Ara, G. Guekos, and K. J. Vahala, "30 nm Wavelength Conversion at 10 Gb/s by Four-Wave Mixing in

a Semiconductor Optical Amplifier," *Optical Fiber Communication Conference*, San Jose, California, February 22–27, 1998, paper WB7.

[5] R. Paiella, G. Hunziker, M. Ziari, A. Mathur, and K. J. Vahala, "Wavelength Conversion by Four-Wave Mixing in a Folded-Path, Self-Pumped Semiconductor Optical Amplifier," *Optical Fiber Communication Conference*, San Jose, California, February 22–27, 1998, paper WB8.

[6] R. Paiella, G. Hunziker, M. Ziari, A. Mathur, and K. J. Vahala, "Wavelength Conversion Devices Based on Four-Wave Mixing in Semiconductor Lasers with a Bragg Mirror," to be submitted to the *IEEE J. Quantum Electron.*.

[7] A. D'Ottavi, G. Hunziker, R. Paiella, R. Dall'Ara, G. Guekos, P. Spano, and K. J. Vahala, "30 nm Wavelength Conversion at 10 Gb/s by Four-Wave Mixing in a Semiconductor Optical Amplifier," to be published on the June 1998 issue of *IEEE Photon. Technol. Lett.*.

[8] R. Paiella, G. Hunziker, M. Ziari, A. Mathur, and K. J. Vahala, "Wavelength Conversion by Cavity-Enhanced Injection-Locked Four-Wave Mixing in a Fiber-Bragg-Grating Coupled Diode Laser," to be published on the June 1998 issue of *IEEE Photon. Technol. Lett.*.

[9] R. Paiella, G. Hunziker, K. J. Vahala, and U. Koren, "Four-Wave Mixing Mediated by the Capture of Electrons and Holes in Semiconductor Quantum-Well Laser Amplifiers," *Appl. Phys. Lett.*, vol. 71, pp. 3601–3603, 1997.

[10] K. J. Vahala, R. B. Lee, D. F. Geraghty, G. Hunziker, R. Paiella, M. Ziari, and A. Mathur, "Tera-Hertz Carrier Dynamics and Application to All-Optical Wavelength Conversion," *IEEE Lasers and Electro-Optics Society Annual Meeting*, San Francisco, California, November 10–13, 1997, paper MN5 (**Invited Paper**).

[11] G. Hunziker, R. Paiella, M. Ziari, A. Mathur, and K. J. Vahala, "Folded-Path, Self-Pumped Wavelength Converter Based on Four-Wave Mixing in a Semiconductor Optical Amplifier," *IEEE Photon. Technol. Lett.*, vol. 9, pp. 1352–1354, 1997.

[12] K. J. Vahala, R. Paiella, and G. Hunziker, "Ultrafast WDM Logic," *IEEE J. Select. Topics in Quantum Electron.*, vol. 3, pp. 698–701, 1997.

[13] R. Paiella, G. Hunziker, U. Koren, and K. J. Vahala, "Polarization-Dependent Optical Nonlinearities of Multiquantum-Well Laser Amplifiers Studied by Four-Wave Mixing," *IEEE J. Select. Topics in Quantum Electron.*, vol. 3, pp. 529–540, 1997.

[14] K. J. Vahala, R. Paiella, G. Hunziker, R. B. Lee, and D. F. Geraghty, "Ultrafast Semiconductor Carrier Dynamics Probed by Four-Wave Mixing and Application to All-Optical Signal Processing in WDM Systems," *OSA Spring Topical Meeting on Ultrafast Electronics and Optoelectronics*, Incline Village, Nevada, March 17–19, 1997, paper UMC1 (**Invited Paper**).

[15] G. Hunziker, R. Paiella, K. J. Vahala, and U. Koren, "Measurement of the Stimulated Carrier Lifetime in Semiconductor Optical Amplifiers by Four-Wave

Mixing of Polarized ASE Noise," *IEEE Photon. Technol. Lett.*, vol. 9, pp. 907–909, 1997.

[16] R. Paiella, G. Hunziker, K. J. Vahala, and U. Koren, "Measurement of the Interwell Carrier Transport Lifetime in Multiquantum-Well Optical Amplifiers by Polarization-Resolved Four-Wave Mixing," *Appl. Phys. Lett.*, vol. 69, pp. 4142–4144, 1996.

[17] G. Hunziker, R. Paiella, K. J. Vahala, and U. Koren, 'Interwell Carrier Transport Rate Measured by Four-Wave Mixing," *IEEE International Semiconductor Laser Conference*, Haifa, Israel, October 13–18, 1996, paper PDP4 (**Postdeadline Paper**).

[18] K. J. Vahala, R. B. Lee, D. F. Geraghty, G. Hunziker, R. Paiella, "Wavelength Conversion by Four-Wave Mixing in Semiconductor Amplifiers," *Optical Society of America Annual Meeting*, Rochester, New York, October 20–24, 1996, paper MDD2 (**Invited Paper**).

[19] G. Hunziker, R. Paiella, D. F. Geraghty, K. J. Vahala, and U. Koren, "Polarization-Independent Wavelength Conversion at 2.5 Gb/s by Dual-Pump Four-Wave Mixing in a Strained Semiconductor Optical Amplifier," *IEEE Photon. Technol. Lett.*, vol. 8, pp. 1633–1635, 1996.

[20] R. Paiella, G. Hunziker, J. Zhou, K. J. Vahala, U. Koren, and B. I. Miller, "Polarization Properties of Four-Wave Mixing in Strained Semiconductor Optical Amplifiers," *IEEE Photon. Technol. Lett.*, vol. 8, pp. 773–775, 1996.

[21] R. Paiella, G. Hunziker, J. Zhou, K. J. Vahala, U. Koren, and B. I. Miller, "Using Tensor Properties of Four-Wave Mixing in Semiconductor Optical Amplifiers for Polarization-Independent Wavelength Conversion or Pump Suppression," *Conference on Laser and Electro-Optics*, Anaheim, California, June 2–7, 1996, paper CFF1.

Chapter 2

Four-wave mixing in semiconductor optical amplifiers

2.1 Introduction

Semiconductor optical amplifiers (SOAs) are unique because of their large optical gain per unit length. A weak optical signal can be amplified by up to 3 orders of magnitude in a 1 mm long device. Since large optical gain is associated with a short spontaneous carrier lifetime, and low saturation power, operation in a non-linear amplification regime is therefore almost inevitable, even for relatively low optical power levels (a few miliwatts) and high (GigaHertz) modulation speeds. Therefore, these devices are relatively unattractive for linear signal amplification in a fiber-optic transmission link, especially when compared to Erbium doped fiber amplifiers. However, their non-linear behavior has successfully been exploited for all-optical signal processing and wavelength conversion through using the optical gain compression and its very

fast recovery to transfer information from one wavelength to another. There are three phenomena responsible for the optical gain compression in semiconductors. In order of decreasing strength, they are : carrier density depletion, carrier heating and spectral hole burning. The first phenomenon is due to electron-hole recombination via stimulated emission, which reduces the inversion population of the optical medium. Second, the stimulated emission and to a lesser extent the free carrier absorption induce an increase in the quasi-equilibrium temperature of the charge carriers in the bands. The weakest contribution to the gain compression is spectral hole burning in which the optical waves 'dig' a hole into the carrier distribution within the bands.

Four-wave mixing (FWM) involves the photomixing of two harmonic waves in this non-linear semiconductor medium. A typical FWM experiment is schematically depicted in Fig. 2.1. A strong pump wave at angular frequency ω_p (and with complex field amplitude $\vec{E}^{(p)}$) is combined with a weaker probe wave at angular frequency ω_q ($\vec{E}^{(q)}$). The non-linear interaction of these two waves generates a modulation of the gain (and the refractive index through the Kramers-Kronig relation) in the amplifier at the detuning frequency $\Omega = \omega_p - \omega_q$. The pump wave and probe waves are scattered by this time varying gain medium into two FWM sidebands, which occur at frequencies $\omega_p \pm \Omega$ and $\omega_q \pm \Omega$. The FWM signal of interest in most of this work is the one occurring at $\omega_p + \Omega$ shown in Fig. 2.1. Quantum mechanically, this signal is generated in a four-photon process in which two pump photons are absorbed while a probe and a FWM photon are emitted, hence the name four-wave mixing. Physically, this non-linearity comes about through the optical intensity dependence

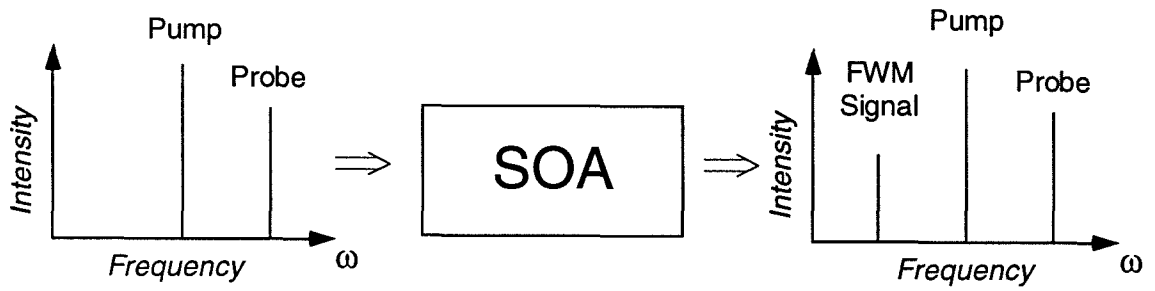

Figure 2.1: Four-wave mixing in a semiconductor optical amplifier. The graph on the left shows the input spectrum with the the pump and probe frequencies, and the graph on the right shows the output spectrum with the new frequency component to the left of the pump, due to the four-wave mixing.

of the total carrier density, the carrier temperature and the electron occupation probability. Since the optical intensity in the amplifier has a term at the pump-probe detuning frequency, all three quantities will have a frequency component at Ω. The gain and index of the amplifier in turn depend strongly on the carrier density, temperature and electron occupation probability, and it will therefore contain a modulation component at Ω from each contribution. At low detuning frequencies, the dominant FWM non-linearity stems from the carrier density modulation (CDM). As the detunig frequency exceeds the stimulated recombination rate of the carriers (typically a few GigaHertz), this contribution becomes weaker, and eventually the carrier heating (CH) contribution will be the dominant one. This in turn will be damped as the detuning frequency exceeds the rate at which the carrier temperature relaxes to the lattice temperature through electron-phonon interactions (typically at a few hun-

dred GigaHertz). Finally, at detuning frequencies on the order of a TeraHertz, the spectral-hole burning (SHB) contribution will become dominant, until the damping through the electron-electron scattering ultimately limits the modulation rate. The measurement of the FWM signal versus detuning reveals the corner frequency associated with each mechanism. The wide detuning frequency range available through photomixing of standard tunable semiconductor lasers translates into a time resolution of less than 100 fs, which makes this technique attractive to study ultrafast relaxation mechanisms within semiconductors.

The study of these mechanisms is important in many device applications based on these semiconductor amplifiers. In this context, the non-linearity associated with the interaction of the light with the carrier density as a whole is the stongest and most important one. In amplifiers, it is not only responsible for most of the static gain compression, but also for the cross-talk between different wavelength channels traveling though the amplifier. When amplifying picosecond pulses, it also produces pulse distortion and frequency chirping [1]. In a semiconductor laser, this interaction produces a resonant enhancement of the intensity and phase fluctuations at the laser resonance frequency [2]. While the non-linearity associated with the carrier density modulation may be detrimental to the operation of SOAs as in-line repeaters or laser sources, it can be used very effectively as a cross-gain or cross-phase wavelength conversion device as well as for all-optical signal regeneration [3]. The principle is to use a modulated beam to saturate the amplifier gain, and to inject a weaker signal at a different wavelength into the amplifier, which will be amplitude and phase

modulated as it travels through the gain medium. For cross-phase modulators, this is usually done in an interferometer to translate the phase modulation into an amplitude modulation.

Unlike cross-gain and cross phase modulation, FWM is a coherent wavelength conversion process in which the amplitude and the phase of the converted signal are directly related to those of the probe wave. Since the generation of the gain and index modulation as well as the scattering of the pump are instantaneous processes the wavelength conversion is transparent to the modulation format and the bit rate of the input signal. Another important characteristic of the FWMs wavelength converters is that they produce a phase conjugate replica of the input, and can therefore be used to compensate for group velocity dispersion in optical fibers by mid-span optical phase conjugation. Finally, FWM wavelength converters can be used to convert the wavelength of multiple channels simultaneously.

2.2 The four-wave mixing susceptibility

In this section, we will outline the derivation of the general expression for the four-wave mixing susceptibility tensor $\tilde{\tilde{\chi}}^{(3)}$. As in Refs. [5, 6], the semiconductor medium is modeled as a collection of inhomogeneously broadened two-level systems, and we consider the interaction of this medium with two harmonic input waves, a pump and a probe. Our objective is to show how the different relaxation processes enter the detuning dependence of the four-wave mixing. We want to obtain an expression for the third-order non-linear susceptibility which contains all three contributions responsible

for the four-wave mixing. The starting point is the density matrix equations of motion for occupation probabilities of the electrons in the conduction band (ρ_c) and in the valence band (ρ_v) at a given wave vector $\vec{k}$ coupled to the electromagnetic field $\vec{E(t)}$ though the electric dipole moment $\vec{\mu}_{cv}$ [8, 9] :

$$\dot{\rho}_v + \frac{1}{\tau_1}(\rho_v - f_v) = \frac{i}{\hbar}(\vec{\mu}^*_{cv}\rho_{cv} - \rho^*_{cv}\vec{\mu}_{cv}) \cdot \vec{E}(t) \tag{2.1}$$

$$\dot{\rho}_c + \frac{1}{\tau_1}(\rho_c - f_c) = -\frac{i}{\hbar}(\rho_{cv}\vec{\mu}^*_{cv} - \vec{\mu}_{cv}\rho^*_{cv}) \cdot \vec{E}(t), \tag{2.2}$$

where we have omitted the explicit $\vec{k}$-dependence of ρ and $\vec{\mu}$ to simplify the notation. The second term on the left in these equations describes the relaxation of the occupation probabilities to the quasi-equilibrium Fermi function in each band $f_{c,v}$ due to the carrier-carrier scattering, with a characteristic time constant τ_1 (assumed to be the same for both bands). The time evolution of the off-diagonal polarization function, ρ_{cv}, is given by

$$\dot{\rho}_{cv} + \left(i\omega_{cv} + \frac{1}{\tau_{cv}}\right)\rho_{cv} = \frac{i}{\hbar}(\vec{\mu}_{cv}\rho_v - \rho_c\vec{\mu}_{cv}) \cdot \vec{E}(t) \tag{2.3}$$

where $\hbar\omega_{cv}$ is the transition energy and τ_{cv} is the dipole dephasing lifetime.

The quasi-equilibrium Fermi functions of the electrons in each band depend on the total carrier density and the carrier temperature for that band, $f_{c,v} = f_{c,v}(N(t), T_{c,v}(t))$. To obtain a closed set of equations, we need the time evolution of both these macroscopic quantities. By definition, the total carrier density is

$$N(t) = \frac{1}{V} \sum_{\vec{k};x=v,c} \rho_x(t). \tag{2.4}$$

By summing up the equations of motion for the density matrix, we obtain the rate equation of the carrier density

$$\dot{N} + \frac{N}{\tau_s} = -\frac{i}{\hbar}\frac{1}{V} \sum_{\vec{k},v,c} (\rho_{cv}\vec{\mu}^*_{cv} - \vec{\mu}_{cv}\rho^*_{cv}) \cdot \vec{E}(t). \tag{2.5}$$

The rate $1/\tau_s$ is introduced to account for the interband recombination processes, which tends to restore the steady state carrier density, determined by electrical pumping. Alternatively, this could have been introduced explicitly in the equations of motion for ρ_c, ρ_v [6].

To obtain the time evolution of the temperature, we first compute the energy density in each band

$$U_x(t) = \frac{1}{V} \sum_{\vec{k}} \epsilon_x \rho_x(t), \tag{2.6}$$

where $x = c, v$ is the band index. We expand this in terms of the independent variables N and T_x, and subsequently eliminate N with Eq. 2.5. The result is

$$\dot{T}_x + \frac{T_x - T_L}{\tau^x_h} = -\frac{i}{\hbar}\frac{1}{V} \sum_{\vec{k},v,c} \frac{\epsilon_x - \mu_x}{h_x} (\rho_{cv}\vec{\mu}^*_{cv} - \vec{\mu}_{cv}\rho^*_{cv}) \cdot \vec{E}(t), \tag{2.7}$$

where we have again introduced a phenomenological relaxation term on the left hand side, $1/\tau^x_h$, which reflects the equilibration rate of the carrier temperature with the lattice temperature T_L through carrier-phonon interactions within each band. The term on the right hand side reflects the change in temperature due to stimulated

emission, where μ_x and h_x are the chemical potential and heat capacity of subband x = c, v. This term can be interpreted as follows : the change in temperature is proportional to the change in energy in the band (referenced to the quasi-Fermi energy), divided by the heat capacity appropriate for that band. The quantities μ_x and h_x appear through the expansion of the energy density U_x in terms of the independent variables N and T_x.

We are interested in the situation where two input waves are coupled into this active region, a pump wave $\vec{E}^{(p)}$ of frequency ω_p and a probe wave $\vec{E}^{(q)}$ of frequency ω_q. The four-wave mixing signal is generated by the induced non-linear polarization density at a frequency $\omega_s = 2\omega_p - \omega_q$, given by $P_i^{(s)} = \chi_{ijkl} E_j^{(p)} E_k^{(p)} (E_l^{(q)})^*$, where the indices i, j, k, l refer to the polarization components of the waves, and $\vec{P}$ is related to the density matrix through

$$\vec{P}(t) = \frac{1}{V} \sum_{\vec{k},v,c} \rho_{cv}(t) \vec{\mu}_{cv}^{*}. \tag{2.8}$$

In the presence of the two detuned excitation frequencies, the carrier density, the carrier temperature and the occupation probabilities are all modulated through their dependence on the intensity of the total input fields. We therefore look for solutions of the form

$$N = N^{(0)} + \left(N^{(\Omega)} e^{-i\Omega t} + c.c. \right),$$

$$T_x = T_x^{(0)} + \left(T_x^{(\Omega)} e^{-i\Omega t} + c.c. \right),$$

$$\rho_x = \rho_x^{(0)} + \rho_x^{(\Omega)} e^{-i\Omega t} + \rho_x^{(-\Omega)} e^{i\Omega t},$$

$$\rho_{cv} = \rho_{cv}^{(\omega_p)} e^{-i\omega_p t} + \rho_{cv}^{(\omega_q)} e^{-i\omega_q t} + \rho_{cv}^{(\omega_s)} e^{-i\omega_s t} \tag{2.9}$$

where $\Omega = \omega_p - \omega_q$ is the detuning frequency. These solutions are substituted into the equations of motion for the density matrix, carrier density and temperature. The Fermi functions are expanded in a Taylor series in N and $T_{c,v}$ about the equilibrium values, and only the terms up to the third order in the input field amplitudes are kept. This procedure is described in detail in Ref. [6], and the result for the non-linear susceptibility tensor is found to be

$$\tilde{\tilde{\chi}}^{(3)} = \tilde{\tilde{\chi}}^{(3)}|_{CDM} + \tilde{\tilde{\chi}}^{(3)}|_{CH} + \tilde{\tilde{\chi}}^{(3)}|_{SHB} \tag{2.10}$$

where the individual contributions from carrier density modulation (CDM), carrier heating (CH), and spectral hole burning (SHB) are given by :

$$\begin{aligned}
\tilde{\tilde{\chi}}^{(3)}|_{CDM} &= \frac{\tau_s}{1 - i\Omega\tau_s}\, \xi_{CDM}\, \tilde{\tilde{\mu}}_{CDM} \\
\tilde{\tilde{\chi}}^{(3)}|_{CH} &= \frac{\tau_h}{1 - i\Omega\tau_h}\, \xi_{CH}\, \tilde{\tilde{\mu}}_{CH} \\
\tilde{\tilde{\chi}}^{(3)}|_{SHB} &= \frac{\tau_1}{1 - i\Omega\tau_1}\, \xi_{SHB}\, \tilde{\tilde{\mu}}_{SHB}.
\end{aligned} \tag{2.11}$$

The relevant detuning frequency dependence for each process is given by the first order pole containing the equilibration time constant for the corresponding relaxation (we have assumed that the electrons in the conduction band and in the valence band have the same heating time constant). The complex amplitude of each contribution to the non-linearity is contained in the ξ factors which reflect how effectively the gain and index can be modulated by each process; their explicit expression is not essential here, and can be found in [8]. The $\tilde{\tilde{\mu}}$ tensors contain the polarization dependence of the

susceptibility, and will be discussed in detail in the next chapter. In order write the above expressions for the susceptibility, we have neglected the $|\vec{k}|$-dependence of the optical matrix elements and assumed a parabolic in-plane dispersion relation, which is a valid assumption for the highly strained quantum well amplifiers used for all the experiments involving the polarization properties of FWM.

The experimental verification of the detuning dependence for co-polarized pump and probe waves is shown in Fig. 2.2, where both the frequency up- and down-converted FWM signal are measured as a function of detuning frequency. The graph also shows the fit to the data with the three relevant time constants and ξ used as parameters. The frequency up-conversion has a better conversion efficiency because the phases of the ξ coefficients add constructively in this case.

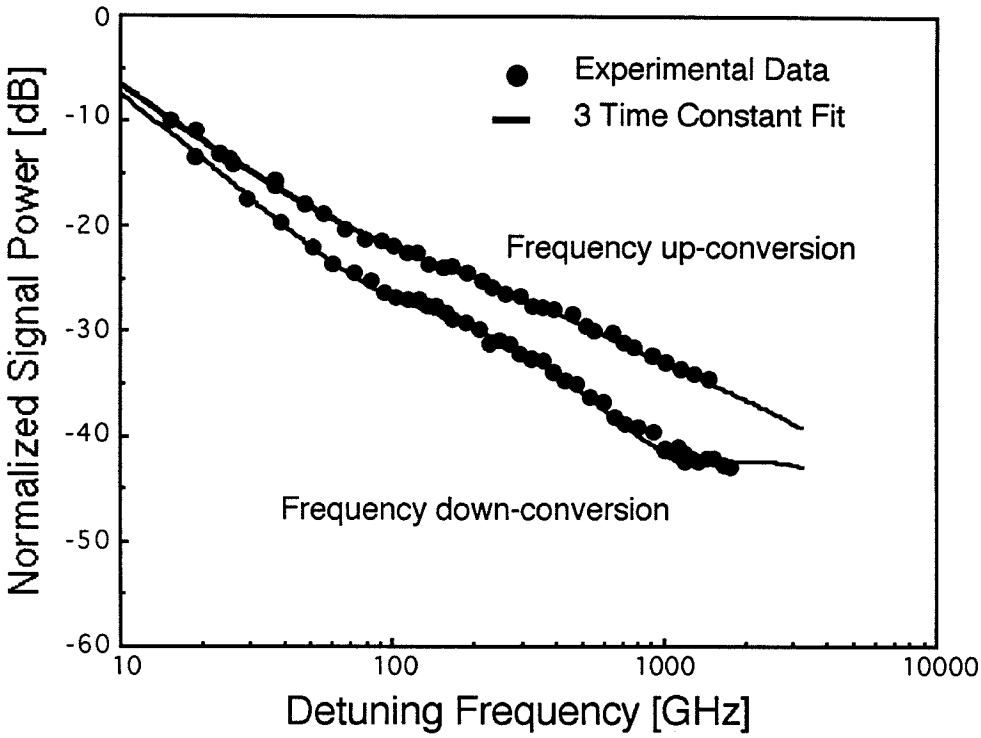

Figure 2.2: Measurement of the four-wave mixing efficiency versus detuning with the three time constant fit corresponding to the carrier density modulation, carrier heating and spectral hole burning. Data from J. Zhou in Ref. [10].

Bibliography

[1] N. Olsson, G. Agrawal, *Appl. Phys. Lett.*, **55**, p. 13 (1989).

[2] B. Daino, P. Spano, M. Tamburrini, S. Piazzola, *IEEE Journal of Quantum Electronics*, **19**, p. 266, 1983.

[3] by C. Joergensen, S. Danielsen, K. Stubkjaer, M. Schilling, K. Daub, P. Doussiere, F. Pommerau, P. Hansen, H. Poulsen et al. *IEEE J.of Selected Topics in Quantum Electronics* **3**, p. 1168, (1997).

[4] A. Bogatov, P. Eliseev, B. Sverdlov, *IEEE Journal of Quantum Electronics*, **11**, p. 510, 1974.

[5] G. P. Agrawal, *J. Opt. Soc. Am. B*, **5**, p. 147, 1988.

[6] A. Uskov, J. Mϕrk, and J. Mark, *IEEE Photon. Technol. Lett.* **30**, p. 1769, 1994.

[7] A. Mecozzi, S. Scotti, A. D'Ottavi, E. Iannone, P. Spano, *IEEE Journal of Quantum Electronics*, **31**, p. 689, 1995.

[8] R. Paiella, G. Hunziker, U. Koren, K. Vahala, *IEEE J.of Selected Topics in Quantum Electronics* **3**, p. 529, (1997).

[9] K. Vahala, Caltech Aph 190, Class notes, 1996.

[10] J. Zhou, PhD Thesis, Caltech 1995.

[11] K. Hall, A. Darwish, E. Ippen, U. Koren, G. Raybon, *Appl. Phys. Lett.*, **62**, p. 1320 (1993).

Chapter 3

Polarization properties of FWM

3.1 Introduction

In the previous chapter, we have shown how the FWM susceptibility depends on the pump-probe detuning frequency. We have found that there are three contributions to the mixing, and introduced a tensor $\tilde{\mu}$ for each contribution to account for the polarization dependence of the signal components on the input waves. In this chapter, we give the explicit form of this tensor for each mechanism and explain the physical meaning of the polarization selection rules of the four-wave mixing. We then focus our attention to highly strained quantum well structures, where the optical transitions involve uncoupled states of the valence band (heavy holes or light holes). The polarization selection rules are then inserted into the susceptibility tensor, and the corresponding coupled mode equations of the FWM are solved. The results of the model are confirmed by experimental data, and we demonstrate the power of this theory in two practical cases.

3.2 The polarization tensor

In order to account for arbitrary input polarizations for the pump and the probe waves, the model presented in the previous chapter has to be expanded to include explicitly the two spin degenerate states of each band. We will show that this is necessary, as we will see that four-photon processes involving separately distinct spin states at a given $\vec{k}$ transition are important to explain the features of the polarization properties.

The inclusion of the spin-degenerate states is straightforward, since the equations of motions for states of opposite spins are the same. However, the density matrix will contain important new off-diagonal elements, namely $\rho_{cc'}$ and $\rho_{vv'}$, which describe the (optically induced) coherence between states of opposite spins. The equation of motion for these off-diagonal elements is given by

$$\dot{\rho}_{cc'} + \frac{1}{\tau_{cc'}}\rho_{cc'} = -\frac{i}{\hbar}\sum_{v'}\left(\rho_{cv'}\vec{\mu}^{*}_{c'v'} - \vec{\mu}_{cv'}\rho^{*}_{c'v'}\right)\cdot\vec{E}(t), \tag{3.1}$$

and similarly for the valence band (with a + sign on the right hand side). The relaxation rates $1/\tau_{cc'}$ and $1/\tau_{vv'}$ reflect the rate at which collisions dephase the spin coherence of a state, and are presumably faster than the usual dipole dephasing rate $1/\tau_1$ [1]. We will assume $1/\tau_{cc'} = 1/\tau_{vv'} = 1/\tau_2$ in the remainder.

As for the occupation probability, we expect $\rho_{cc'}$ and $\rho_{vv'}$ to contain an oscillatory component at Ω through their dependence on the intensity for a third order non-linearity. We thus perform the same expansions as in Eq. 2.2, and derive the expression for $\tilde{\tilde{\chi}}^{(3)}$ as before. With the exception of SHB, which we will discuss at the

end of this section, the general expressions for $\tilde{\tilde{\chi}}^{(3)}$ remain the same as in Eq. 2.11, but the expressions for the polarization tensors $\tilde{\tilde{\mu}}$ now contain all the possible transitions for the four level system at a given $\vec{k}$.

For the carrier density modulation and the carrier heating, the polarization tensor is given by

$$\mu_{ijkl}|_{CDM} = \mu_{ijkl}|_{CH} = \left\langle \sum_{v,c} (\vec{\mu}_{cv})_j (\vec{\mu}_{vc})_i \right\rangle \left\langle \sum_{v,c} (\vec{\mu}_{cv})_k (\vec{\mu}_{vc})_l \right\rangle \tag{3.2}$$

where $(\vec{\mu}_{vc})_i$ is the i-th component of $\vec{\mu}_{vc}$ ($i = 1, 2$ for TE, TM components), $\langle ... \rangle$ denotes the average over all $\vec{k}$ directions in the quantum well plane. The nature of FWM by CDM and CH as a two step process, the generation of the dynamic grating followed by the scattering of the pump, is reflected in this expression.

The second term of the tensor, involving the l-th component of the probe together with k-th component of the pump reflects the generation of the carrier density and carrier temperature modulation. The first term of the tensor, involving the i-th component of the FWM signal together with j-th component of the pump, reflects the polarization selection rule for the scattering of the pump. Notice that each of these contributions appear as a separate sum over all states, indicating that the two processes are decoupled and do not in general involve the same transition. Fig. 3.1 is an illustration of these two processes. In the left panel, the emission of a probe photon and simultaneous absorption of a pump photon creates a modulation of the occupation probability of the state $\bar{c}$. The resulting carrier density and temperature modulation is then responsible for the two-photon process shown in the right panel,

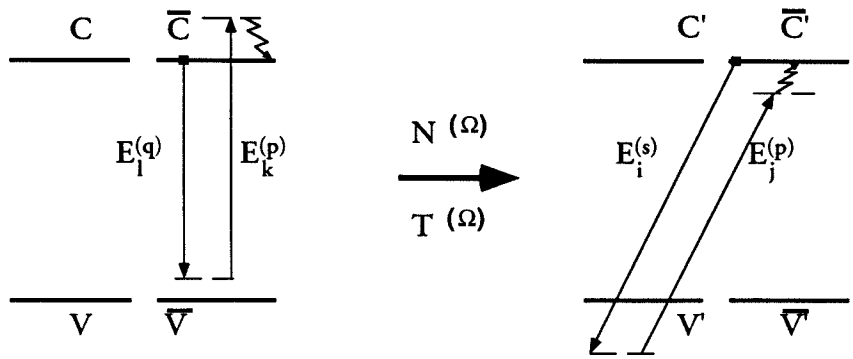

Figure 3.1: Diagram illustrating the photon transitions involved FWM by carrier density modulation and carrier heating. The two-photon process responsible for generation of the modulation is shown on the left, and the two-photon process responsible scattering of the pump is shown on the right. Notice that the electronic transition can be different for each process.

where the pump is scattered into the FWM signal, occurring at a different transition $\bar{c}', v'$. The important point here is that for CDM and CH, the final state for the individual 2-photon processes has to be the same, but they can each occur at a different transition, even in a different physical location of the semiconductor (as for example in the interwell transport experiment of chapter 4).The polarization tensor for SHB is given by

$$\tilde{\tilde{\mu}}|_{SHB(1)} = \left\langle \sum_{v,c,v'} (\vec{\mu}_{cv})_j (\vec{\mu}_{vc})_i (\vec{\mu}_{cv'})_k (\vec{\mu}_{v'c})_l + \sum_{v,c,c'} (\vec{\mu}_{vc})_i (\vec{\mu}_{cv})_j (\vec{\mu}_{vc'})_l (\vec{\mu}_{c'v})_k \right\rangle$$

$$\tilde{\tilde{\mu}}|_{SHB(2)} = \left\langle \sum_{v,c,v'} (\vec{\mu}_{\bar{c}v})_j (\vec{\mu}_{vc})_i (\vec{\mu}_{cv'})_k (\vec{\mu}_{v'\bar{c}})_l + \sum_{v,c,c'} (\vec{\mu}_{vc})_i (\vec{\mu}_{c\bar{v}})_j (\vec{\mu}_{\bar{v}c'})_l (\vec{\mu}_{c'v})_k \right\rangle \quad (3.3)$$

where for a given spin state c (v), $\bar{c}$ $(\bar{v})$ denotes the opposite spin. The detuning dependence of $\tilde{\tilde{\mu}}|_{SHB(1)}$ is as in Eq. 2.11, but for $\tilde{\tilde{\mu}}|_{SHB(2)}$ the prefactor has to be

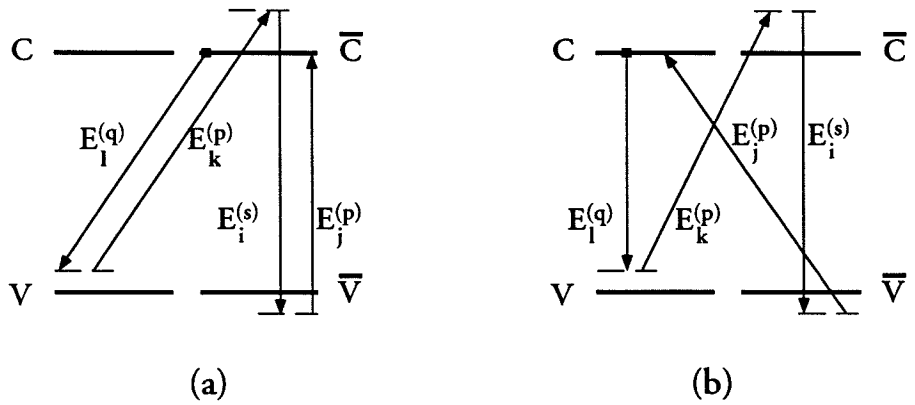

Figure 3.2: Photon transitions illustrating the photon transitions involved FWM by spectral hole burning. The diagram in (a) shows the spectral hole burning process where the occupation probability of the initial state is modulated. The diagram in (b) shows a the case where the spectral hole burning is generated by modulation of the relative coherence of the spin-degenerate states of the valence band.

modified to $\frac{\tau_2}{1-i\Omega\tau_2}$. In contrast to the case of CDM and CH, the SHB polarization tensor cannot be divided into two contributions. This is because FWM by SHB occurs through a single 4-photon process at a given set of levels $c, \bar{c}, v, \bar{v}$. Furthermore, the inclusion of the spin-degenerate states and the corresponding coherence modulation functions has lead to an additional contribution to the mixing (SHB(2)), with a frequency cutoff given by $1/2\pi\tau_2$. SHB(1) is the 'ordinary' contribution to the FWM, which results from modulation of the occupation probability of the initial electronic state of the process. Since in this case the second intermediate state is the same as the initial state, the polarization selection rules and their interpretation are the same as for CDM and CH. An example of a 4-photon process which would contribute to SHB(1) is illustrated in Fig. 3.2(a). Compare this with the process shown in Fig. 3.1,

where the same spin states are involved, but now the process is no longer mediated by carrier density or temperature, but occurs at a single $\vec{k}$ transition through the modulation of the occupation probability of the initial state.

SHB(2) on the other hand describes FWM processes where the second intermediate state is the spin-opposite of the initial state (see Fig. 3.2(b)). This results in a modulation of the relative coherence between these two states, generated for example by the absorption of a pump photon and the emission of an orthogonally polarized probe photon. As we will show in the next section, the polarization selection rules for this process are the opposite from SHB(1).

3.3 Highly strained quantum wells

In order to evaluate the sums appearing in the expressions for $\tilde{\tilde{\mu}}$, we need to specify the states c and v for the optical transitions involved in the FWM. In general, they are the appropriate eigenstates of the Luttinger Hamiltonian, as given in Ref. [2] for instance. Since all the polarization work presented in this thesis was done with highly (1%) strained quantum well (QW) structures, we will use the total angular momentum eigenstates, and neglect valence band mixing. This approximation is valid if the transitions are close to the band edge. As an example, we quote the result for the sum appearing in Eq. 3.2 for a tensile strained QW :

$$\left\langle \sum_{v,c} \vec{\mu}_{cv}\vec{\mu}_{vc} \right\rangle = |\langle S,\uparrow |ex|X,\uparrow \rangle|^2 |\langle f_k^e|f_k^{lh}\rangle|^2 \left(\frac{1}{3}\hat{x}\hat{x} + \frac{4}{3}\hat{z}\hat{z}\right) \tag{3.4}$$

where $M = \langle S,\uparrow |ex|X,\uparrow \rangle$ is the Kane Matrix element and $O = \langle f_k^e|f_k^{lh}\rangle$ is the

envelope function overlap between an electron in the conduction band and a hole in the valence band. $\hat{x}$ and $\hat{z}$ denote the TE and TM directions respectively. Writing out all the other sums appearing in the expressions for $\tilde{\tilde{\mu}}$ then leads to the following selection rules :

$$\mu_{ijkl}|_{CDM} = \mu_{ijkl}|_{CH} = \mu_{ijkl}|_{SHB(1)} = |M|^4 \, |O|^4 \, \delta_{1,i}\delta_{1,j}\delta_{1,k}\delta_{1,l} \tag{3.5}$$

for the compressively strained wells, and

$$\mu_{ijkl}|_{CDM} = \mu_{ijkl}|_{CH} = \mu_{ijkl}|_{SHB(1)} = |M|^4 \, |O|^4 \, \delta_{ij}\delta_{kl} \, \frac{1}{9} \begin{bmatrix} 1 & 4 \\ 4 & 16 \end{bmatrix}$$

$$\mu_{ijkl}|_{SHB(2)} = |M|^4 \, |O|^4 \, \frac{2}{9} \left(\delta_{ik}\delta_{jl} - \delta_{il}\delta_{jk}\right) \tag{3.6}$$

for the tensile strained wells (i, k label the rows and columns in the 2×2 matrix).

The physical interpretation of these selection rules goes as follows. For highly compressively strained quantum wells, only TE polarized light interacts with the active medium and the polarization selection rules are trivial : only the TE components of the input waves contribute to a TE polarized FWM signal, and modulation of the spin-spin coherence is impossible. In tensile strained quantum wells, four-wave mixing by CDM, CH and SHB(1) can be interpreted as follows : the input waves generate two types of gratings, one induced by the TE components of the input waves (TE-induced gratings), and the other by their TM components (TM-induced gratings). The phase between these two gratings depends on the relative input polarizations, and the resulting FWM signal is strongest if the TE-induced gratings are in phase

with the TM-induced gratings. This occurs when the pump and the probe waves are co-polarized. On the other hand, if the input waves are orthogonally polarized, the two gratings are out of phase and tend to cancel each other. The cancellation is not complete however, and unlike in the case of isotropic media, even orthogonal pump and probe polarizations can generate a FWM signal in a tensile strained QW, except for TE and TM polarized pump and probe, in which case both gratings are zero for the above FWM mechanisms. In the second process of the mixing, the TE and TM components of the signal are generated by scattering of the corresponding polarization components of the pump. The four-wave mixing processes involving the spin-spin coherence modulation are the exception to the above rule, since for instance a TE polarized pump and a TM polarized probe can produce a modulation of the off-diagonal matrix element. Subsequently, the TE component of the pump is scattered into a TM polarized FWM signal. In Chapter 4 we will describe an experiment in which this contribution is measured.

3.4 Propagation effects

In a realistic comparison of experimental results with theoretical predictions, it is important to keep in mind that the FWM conversion efficiency is strongly affected by propagation effects. In order to include such effects in our model, we need to solve the standard coupled-mode equations of FWM in optical amplifiers for the pump (p), the probe (q) and the four-wave mixing signal (s)

$$\frac{dE_i^{(f)}}{dy} = T_i^{(f)}(y)E_i^{(f)}(y) \qquad f : p, q$$

$$\frac{dE_i^{(s)}}{dy} = T_i^{(s)}(y)\ E_i^{(s)}(y) + \frac{i}{2}\frac{\omega_s \mu_0 c}{n_i}\sum_{j,k,l}\chi_{ijkl}S(y)E_j^{(p)}(y)E_k^{(p)}(y)\left(E_l^{(q)}(y)\right)^*, \qquad (3.7)$$

where

$$T_i^{(f)}(y) = \frac{1}{2}\left[g_i^{(f)}S(y)(1 - i\alpha_i^{(f)}) - \gamma\right] + i\,\frac{\omega_f n_i}{c}, \qquad f : p, q, s. \qquad (3.8)$$

In these equations, y is along the direction of wave propagation, $g_i^{(f)}$ and $\alpha_i^{(f)}$ are the modal gain coefficient and linewidth enhancement factor for the $i^{(th)}$ component of the field at frequency ω_f, γ the internal loss coefficient and n_i the background refractive index. Finally, we defined the saturation factor $S(y) = \frac{1}{1+I(y)/I_{sat}}$ where $I(y)$ and I_{sat} are the total optical intensity and saturation intensity of the SOA.

Solution of these equation (and use of the FWM polarization selection rules) allows us to write the FWM signal field at the SOA output ($y = L$) in terms of the input fields as follows

$$E_i^{(s)}(L) = \left(E^{(p)}(0)\right)^2\left(E^{(q)}(0)\right)^*\left[\sum_{k=1}^{2}(p_i\ M_{iikk}\ p_k\ q_k^*) + \right.$$
$$\left. + M_{ilil}\Big|_{l\neq i}\ p_l p_i q_l^*\ + M_{illi}\Big|_{l\neq i}\ p_l^2 q_i^*\right], \qquad (3.9)$$

where we defined

$$M_{ijkl} = \chi_{ijkl}R_{ijkl},$$

$$R_{ijkl} = \frac{i}{2}\frac{\omega_s \mu_0 c}{n_i} \exp\left(\int_0^L dy T_i^{(s)}\right) \int_0^L dy S \exp\left[\int_0^y dy' \left(T_j^{(p)} + T_k^{(p)} + (T_l^{(q)})^* - T_i^{(s)}\right)\right] \tag{3.10}$$

and $\tilde{\tilde{\chi}}$ is the susceptibility tensor, as defined in Eq. 2.11. In typical multiquantum-well SOAs, the propagation factor R_{ijkl} is also a strong function of the fields polarization, due to both the anisotropy and the wavelength-dependence of the gain coefficient and of the refractive index. These considerations are important in order to make any quantitative predictions of the dependence of the FWM signal intensity and polarization on the polarizations of the input waves.

3.5 Experimental results

We are now ready to confront the results of our theoretical model with experimental results. To this end, we used a multi quantum-well semiconductor optical amplifier comprising three pairs of alternating compressive/tensile strained quantum wells. The pump and probe waves are provided by a tunable Erbium doped fiber ring laser (EDFRL) and a distributed feedback (DFB) semiconductor laser, and we used an Erbium doped fiber amplifier (EDFA) to boost the power before coupling the two signals into the SOA. The detuning was set to 1.5 nm, a value small enough the prevent the birefringence dispersion to affect the relative polarizations of the pump and the probe. Fig. 3.3 shows a typical set of data, in this case taken for a pump polarized at -45° relative to the growth axis (TM) and the probe polarization angle varying from -90° to +90°. Since the detuning is small, we expect the SHB contributions to be negligible, and the continuous line shows a fit of the data to the expression

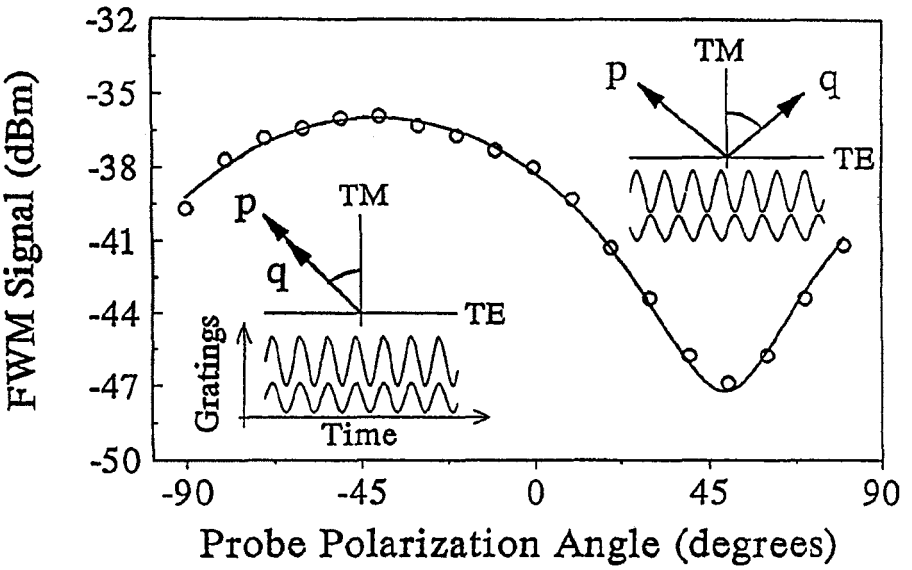

Figure 3.3: FWM signal power as a function of the linear polarization angle of the input signal relative to the TM direction, with linearly polarized pump at -45° and 1.5 nm detuning. The continuous line is a theoretical fit to Eq. 3.11 with fitting parameters $Miikk$. The inset shows the TE and the TM induced grating, and their relative phase. The polarization dependence of the mixing results from the interference between these two gratings.

$$E_i^{(s)}(L) = \left(E^{(p)}(0)\right)^2 \left(E^{(q)}(0)\right)^* \left[p_i \sum_{k=1}^{2} M_{iikk}\, p_k\, q_k^*\right] \tag{3.11}$$

where we used the coefficients M_{iikk} as parameters. The result agrees with our predictions, and in particular notice the non-zero conversion efficiency for orthogonal input polarization, as predicted for anisotropic (tensile strained) quantum well media.

To further demonstrate the validity of Eq. 3.11, and how it governs the polarization of the FWM signal, we used this result to propose a new scheme of pump suppression at the SOA output. Although the technique is probably quite unpractical, it nevertheless shows how the polarization properties of the FWM can be used and controlled. The goal of the experiment is to generate a FWM signal linearly polarized and orthogonal to the pump. Using a polarizer, it is then possible to suppress the pump wave at the SOA output without affecting the FWM signal. To achieve this, we first measured the birefringence of the pump, and computed the necessary input polarization to generate an output linearly polarized at -45° (this value was selected arbitrarily). Then, by fitting multiple sets of data like the one shown in Fig. 3.3, we measured all four non-zero components of the M_{iikk} tensor (amplitude and phase). Finally, given the tensor and the pump polarization, we computed the probe polarization state necessary to generate a FWM signal linearly polarized at +45°. The result is shown in Fig. 3.4, where the lowest trace is the ratio of the SOA output without and with the polarizer. The pump is attenuated by more than 30 dB and the FWM signal is practically unattenuated. This 'hit or miss' experiment requiring the exact measurement of ten parameters through fits of experimental data

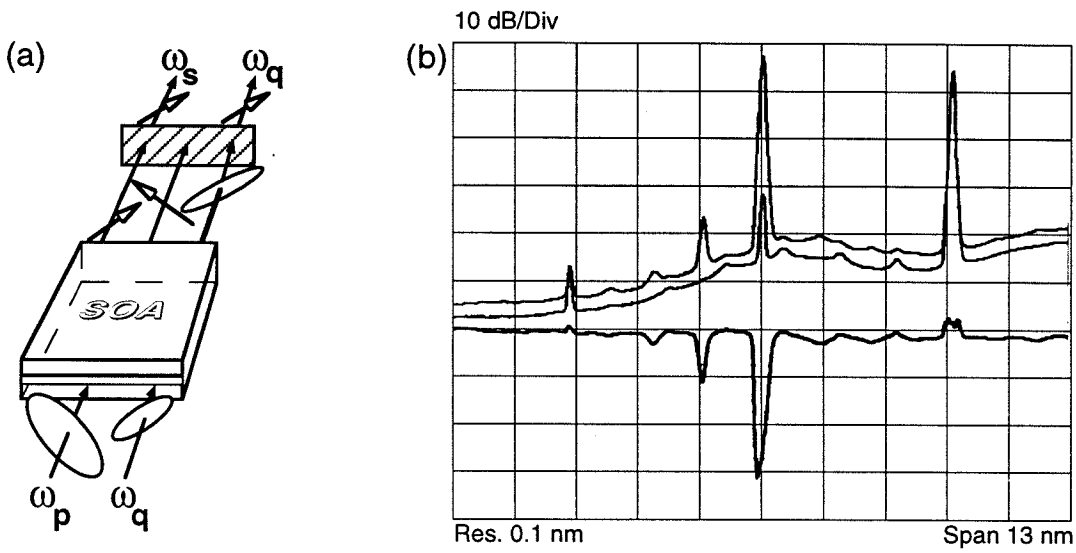

Figure 3.4: (a): Illustration of the pump suppression experiment: the input signal and pump have polarization unit vectors $0.78 \exp i66° \vec{\varepsilon}_1 + 0.63\vec{\varepsilon}_2$, and $0.71(\vec{\varepsilon}_1 + \exp i98° \vec{\varepsilon}_2)$; correspondingly, at the SOA output, the converted signal and pump are linearly polarized at +45° and -45°, respectively. (b): SOA output spectrum with the above input polarizations and with 4 nm detuning, before (upper trace) and after (middle trace) a linear polarizer at +45°. The pump (center peak) is suppressed by more than 30 dB by the polarizer, whereas the converted signal (left peak) is essentially unattenuated. The lower trace is the ratio of the upper two.

to an expression 3.11 we originally derived constitutes a culmination point of this thesis.

On a more practical note, we will end this chapter with a comment on the possibility of achieving polarization independent conversion with a single pump wave at a given polarization. In a typical system application of FWM for wavelength conversion, the polarization state of the probe is random and varies in time, since in general that signal travels through many miles of non-polarization maintaining fiber. The conversion efficiency therefore needs to be independent of the probe polarization. From 3.11, we conclude that the dependence of the FWM signal power on the probe polarization is $P^{(s)} \propto \mid Aq_1 \mid^2 + \mid Bq_2 \mid^2 + Re[Cq_1q_2^*]$ where A, B and C depend on the M coefficients and the pump polarization. Given the normalization condition $\mid q_1 \mid^2 + \mid q_2 \mid^2 = 1$, this means that the conversion is independent of the probe polarization for $\mid A \mid = \mid B \mid$ and $Re[C] = Im[C] = 0$. These equations only admit a solution for the two unknown parameters p_1 and p_2 for a restricted set of values for M_{iikk}. For this reason, there is no general solution for the pump polarization which would result in a polarization independent conversion. Using two pumps, on the other hand, gives additional degrees of freedom to the problem, and we will show in chapter 6 how it can be used to generate a FWM signal with a power independent on input probe polarization.

Bibliography

[1] R. Paiella, G. Hunziker, U. Koren, K. Vahala, *IEEE J.of Selected Topics in Quantum Electronics* **3**, p. 529, (1997).

[2] W. Chow, S. Koch, M. Sargent III, "Semiconductor-Laser Physics." Berlin, Germany : Springer-Verlag, 1994.

Chapter 4

Polarization resolved FWM spectroscopy

4.1 Introduction

In this chapter, we show how the FWM polarization selection rules derived in the previous chapter provide a new tool to investigate the carrier dynamics in semiconductor optical amplifiers. We focus our attention primarily onto phenomena affecting the carrier density as a whole, which occur on a relatively slow time scale of few hundred GigaHertz at most (corresponding to a time resolution on the order of a picosecond). This is the regime where the non-linearities are most dramatic, and relevant to system applications. We will however end with a brief excursion on an ultrafast spectral hole burning phenomena and describe an attempted measurement of the dephasing lifetime of the spin-spin coherence modulation.

We will begin this chapter with two experiments which are based on the fact

that for the carrier density modulation, the processes responsible for the generation of the dynamic gratings and those responsible for the scattering of the pump are decoupled, and as such do not necessarily occur at the same electronic transitions (in the stimulated carrier lifetime experiment, these can be the heavy-hole/light hole transitions respectively) or even the same physical region of the waveguide (for the interwell transport experiment they are the tensile/compressive strained wells). Then, we will describe an experiment aimed at measuring the FWM contribution associated to the spin-spin coherence modulation.

4.2 Stimulated carrier lifetime measurement

In this simple experiment we measure the stimulated carrier lifetime in semiconductor optical amplifiers using polarization-resolved four-wave mixing of a laser source with amplified spontaneous emission (ASE) noise. This method can be used for instance to quickly characterize the bandwidth performance of active layers for application in a cross-gain or cross-phase wavelength converter.

The stimulated carrier lifetime of an optical amplifier is a key physical quantity in determining the amplifier gain, saturation power, as well as the onset and strength of non-linear operation. Its small value in semiconductor optical amplifiers (SOAs), compared to Erbium doped fiber amplifiers (EDFAs), makes SOAs less attractive as linear amplifiers for 1.55μm wavelength systems. However, in non-linear elements, a short stimulated lifetime is advantageous. For example, in wavelength converters exploiting cross-gain or cross-phase modulation, the stimulated carrier lifetime, τ_s,

is the limiting factor to bit-rate transparency, and much effort is being devoted to increase the corresponding cutoff frequency in the conversion efficiency [1, 2, 3]. In this section, we present a novel technique for measuring $1/\tau_s$ using the fact that this frequency is also the first corner frequency in the detuning dependence of the four-wave mixing (FWM) conversion efficiency . The approach does not require a network analyzer, tunable rf-sources, or tunable laser sources. The carrier lifetime corner frequency can be determined in just two rf-spectrum analyzer sweeps, using nothing but a CW laser (pump) and a polarized noise source (probe).

In Chapters 2 and 3, we showed how FWM can be described as a two-step process as follows: first, beating of the input pump and probe waves gives rise to gain and index modulation at the detuning frequency $\Omega = \omega_p - \omega_q$; the pump is then partially scattered by this modulation into a new field harmonic at frequency $\omega_s = \omega_p + \Omega$. Here, we consider only detuning frequencies below 100 GHz, for which the gain and index modulation mainly results from modulation of the carrier density as a whole. In this case, modulation occurs either through beating of the TE components of the input waves or, separately, through beating of their TM components. Furthermore, the TE (TM) component of the pump is then scattered only into a TE (TM) polarized FWM signal. The device used in the experiement was an alternating strain multiquantum well amplifier, and the mixing processes in this case will only involve the tensile strained quantum wells.

A simple FWM configuration that is particularly well suited to studying the stimulated carrier lifetime as well as interwell transport consists of a TM polarized probe

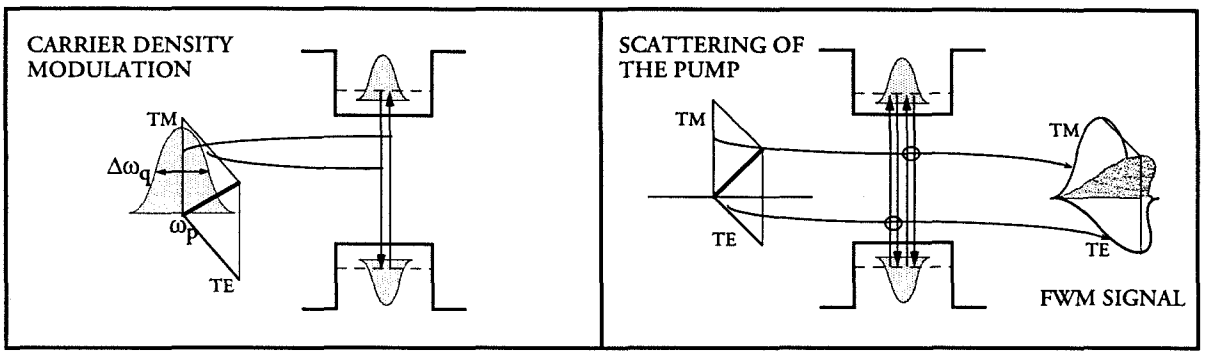

Figure 4.1: Schematics of the FWM process showing the pump and probe polarizations used in the stimulated carrier lifetime measurement. In the left panel, the generation of carrier density modulation by beating of the TM components of the input waves is shown. This occurs only in the tensile wells. In the right panel, we show the scattering of each pump component into the corresponding FWM component. This occurs in both the tensile and the compressively strained wells. The probe is not a single frequency source but rather a continuum of frequencies within a 100 GHz bandwidth. The modulation occurs at all the possible detuning frequencies, indicated by the gray shading, and the FWM signal is therefore also a continuum of frequencies.

and a linearly polarized pump with equal TE and TM components. In this experiment however, we do not use a single frequency probe laser beam, but instead use a broad-band noise source, amplified spontaneous emission from an EDFA, so that the frequency response can be characterized in one scan of the rf-spectrum analyzer (this source is indicated as the gray broad-band signal in Fig. 4.1). We will refer to this noise source as the "probe" despite the fact that it is not a single frequency laser. The polarization of this optical noise is set to be along TM by passing the EDFA emission though a polarization filter. As a result, the pump-"probe" beatnote in the SOA is zero along the TE axis, and optically modulated carriers are only generated by beating of TM waves. However, the TM-induced carrier modulation will lead to a modulation of the gain and refractive index for both the TE and TM components of the pump, thereby generating the TE and TM polarized FWM signals respectively. At the output of the device, we select the TE polarized waves, which, upon detection, will contain the beat note between the pump and the FWM-converted input noise. The frequency dependence of this signal is expected to reflect the first order pole at the stimulated carrier recombination lifetime [4].

In the experiment, we launched a pump laser beam linearly polarized at 45° with respect to the growth (TM) axis and a probe beam of TM-polarized ASE noise from an EDFA into the amplifier (see Fig. 4.2). The beating between the TM component of the pump (laser) and the "probe" (ASE noise) will generate a modulation of the carriers at all frequencies within the half-bandwidth of the ASE noise (0.8 nm in this case, corresponding to all frequencies from 0 to 100 GHz). This will lead to

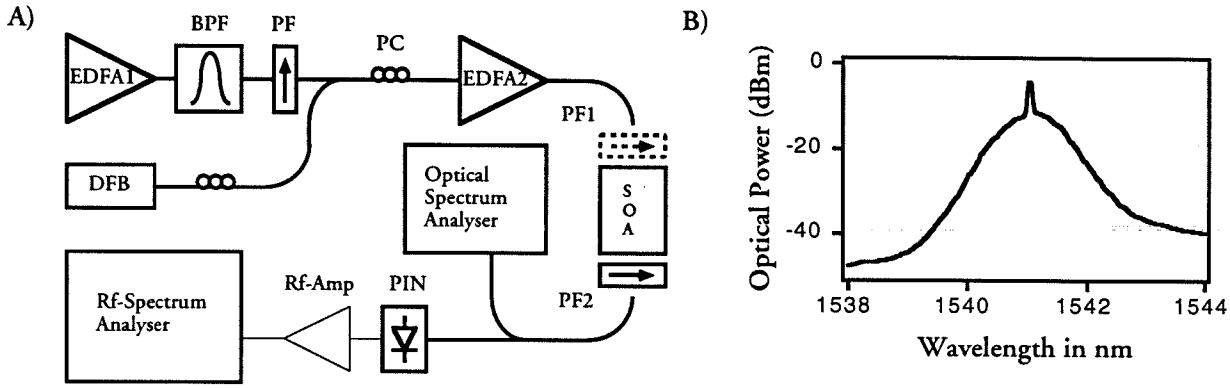

Figure 4.2: A) Experimental setup used to determine the stimulated carrier lifetime. The ASE from EDFA 1 is polarized and then filtered by a 1.6 nm FWHM bandpass filter (BPF). It is then combined with the polarization controlled (PC) output of a distributed feedback laser (DFB). The two sources are amplified in EDFA 2, and the polarization states are individually adjusted and measured with polarizer PF 1 before being coupled into the amplifier. PF 1 is subsequently removed and used at the output of the SOA (PF 2) to select either the TE or the TM emission for input to the photodetector (PIN). The rf-spectrum is amplified before being coupled into the spectrum analyzer. B) Optical spectrum after the SOA, measured without any polarizers, showing the broad input noise source and the DFB line.

the generation of a FWM signal in the same frequency band, along TE and TM. Optical filtering of the ASE noise was necessary in order to increase the gain of the second EDFA (and thus the conversion efficiency) for the narrow wavelength range of interest here. If we set the output polarization filter to TM, the rf-spectral power will be dominated by the amplified pump-"probe" beat noise, which is much stronger than the pump-FWM beat noise. On the other hand, if we set the output polarization filter to TE, then only the pump-FWM beat will be present, since the "probe" has no TE component. This signal component will contain the SOA carrier dynamics. In addition, of course, there will always be an almost white noise component coming from the beat between the pump and the stimulated emission of the SOA. Under highly saturated operating conditions this contribution is much weaker than the above two noise sources. The high saturation condition for this measurement limits the applicability of this technique, but is consistent with operation of cross-gain/cross-phase wavelength converters.

In the specific implementation used here, the total input power into the device was 12.3 dBm, and the optical pump signal (laser) to ASE power ratio was 6.6 dB (measured into 0.1 nm bandwidth). The SOA was 780μm long and had 3 pairs of compressive/tensile strained quantum wells as described in Ref. [7]. The proper input polarization states were selected using a polarizer at the input and by minimizing the power in the orthogonal direction. Since the TE generated rf-signal results from beating of the pump with both FWM sidebands, this is a measure of the amplitude response of the FWM at very low frequencies (i.e. contains no FWM phase infor-

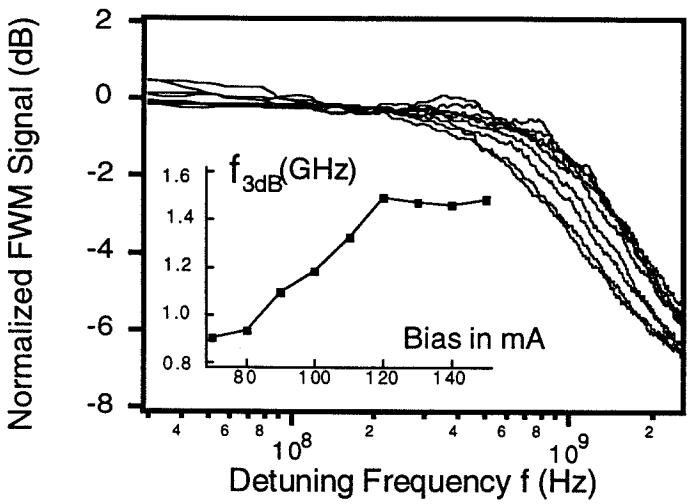

Figure 4.3: Frequency dependence of the TE-polarized FWM efficiency (normalized by the TM polarization emission) as a function of detuning for SOA bias currents ranging from 50 to 150 mA (left to right). The inset shows the 3 dB roll-off frequency as a function of bias current.

mation). Finally, to remove the frequency dependence of our detection electronics, the pump-FWM signal (TE) was normalized to the pump-"probe" noise (TM). The result is shown in Fig. 4.3, where we can clearly identify the 3 dB corner frequency of the FWM conversion efficiency.

The use of a mixed strain amplifier for this experiment is not a prerequisite, and the method is, in principle, applicable to any SOA with optical transitions involving the light hole band: tensile strained quantum wells or bulk amplifiers. Amplifiers consisting of alternating pairs of quantum wells, as is the case here, are slightly more complicated in that the dynamics involved in the generation of the TE polarized FWM signal are different for the two different types of wells. In the tensile wells, the

TE matrix element is non-zero, and the carrier modulation in these wells translates directly into a gain and index modulation for that mode. In the compressive wells, the TM-induced carrier modulation must first be transferred over from the adjacent wells by means of interwell transport. The results from the next section will show that the modulation transfer time constant is much faster than the spontaneous lifetime measured here, which means that the results at hand are not affected by the interwell dynamics.

We applied this experimental method to map out the dependence of the stimulated lifetime on the bias current of the SOA (under conditions of fixed input power). The curves in Fig. 4.3 correspond to an SOA current bias ranging from 50 to 150 mA in steps of 10 mA. The inset shows the corner-frequency changes with current bias. Since the input power into the device is high enough to fully saturate the amplifier for all the bias conditions, this curve reflects the change of the saturated gain with current.

In conclusion, we have proposed and demonstrated a novel technique to characterize the stimulated carrier recombination rate in semiconductor optical amplifiers containing tensile strained quantum wells. The method takes advantage of the polarization properties of FWM to measure the first pole occurring in the conversion efficiency versus detuning frequency.

4.3 Interwell carrier transport measurement

Interwell carrier transport in semiconductor multiquantum-well structures is a highly nonlinear process with significant implications to the use of these structures in electrical and optical devices. Of particular interest is the finite rate at which the carrier densities in neighboring wells reach equilibrium with one another and with the distribution of unconfined carriers in the barrier region. This process has received considerable attention in recent years [8, 9, 10, 11, 12, 13, 14, 15] since it has been associated with nonlinear gain compression, and hence the maximum modulation bandwidth of quantum-well lasers.

A technique very similar to that presented in the previous section can be used to infer the time constant relevant to interwell carrier equilibration. In this case, we will use the polarization properties to generate a carrier density modulation in the tensile strained quantum wells, and probe the response in an adjacent compressively strained well. The polarization configuration required to do this are shown in Fig. 4.4, and consists of a pump wave linearly polarized at 45° relative to the growth axis (TM), and a TM polarized probe wave (now a single frequency laser). Since compressive wells have negligible gain for TM polarized light, the carrier densities are modulated only in the tensile wells and each polarization component of the pump is subsequently scattered into the same component of the FWM signal. In addition, the modulated carrier distributions from each tensile well are coupled into the neighboring compressive wells, where only a TE polarized FWM signal can be generated. As a result, the ratio of TE to TM component of the overall FWM signal has the general form

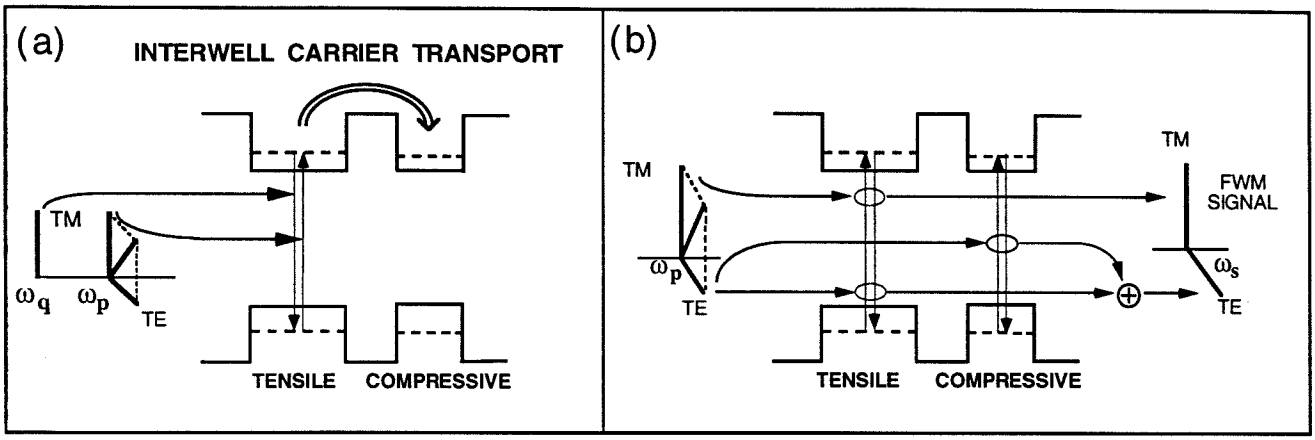

Figure 4.4: Schematics of the FWM processes taking place with the input polarizations used in the interwell transport experiment. As shown in the left panel, modulation of the carrier density is generated directly (through beating of the TM components of the input waves) only in the tensile wells, from which it can then be transferred to a neighboring compressive well. Each polarization component of the pump is then correspondingly scattered into the same component of the FWM signal as shown in the right panel.

$$\frac{P_{Signal}|_{TE}}{P_{Signal}|_{TM}} \sim \left| \frac{\chi^T_{TE,TM} + \chi^{C\leftarrow T}_{TE,TM}}{\chi^T_{TM,TM}} \right|^2 \rightarrow \Omega \gg \Omega_t \rightarrow \left| \frac{\chi^T_{TE,TM}}{\chi^T_{TM,TM}} \right|^2 \qquad (4.1)$$

where the superscripts T and C refer to the tensile and the compressive wells respectively [16]. The polarization selection rules have been used in the above expression to simplify the notation of the FWM tensor, and the second subscript of χ denontes the polarization direction along which the pump and the probe generate the modulation, while the first subscript denotes the polarization direction of the pump and the FWM components involved in the scattering (e.g. $\chi^T_{TE,TM}$ stands for χ^T_{1122}). $\chi^{C\leftarrow T}_{TE,TM}$

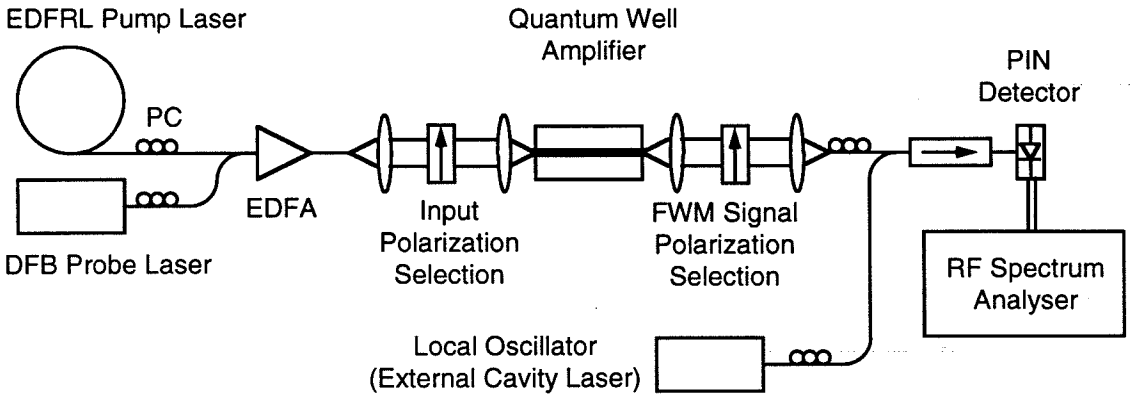

Figure 4.5: Experimental setup used to measure the interwell transport lifetime. PC stands for polarization controller.

describes the FWM process in which the modulation is generated in a tensile well by the TM components of the input waves, and transferred to a compressive well where the TE component of the pump is scattered into the FWM signal. In the limit of detuning frequencies well above the cutoff frequency for the interwell transport ($\Omega \gg \Omega_t$), the TE to TM ratio of the FWM signal is affected by contributions from the tensile wells only, while at lower frequencies, and additional contribution mediated by interwell transport should become apparent. A schematic representation of the polarization components of the input waves involved in the modulation and scattering processes in each type of well is given in Fig. 4.4.

This prediction was verified using a high-sensitivity optical heterodyne detection setup shown in Fig. 4.5. Optical heterodyne detection was necessary for two reasons: first, it allowed for accurate frequency resolution at very low detunings (< 20 GHz), not available with standard optical spectrum analyzers, and second, it provided a

very good signal-to-noise ratio because the detection bandwidth was only 10 MHz (as opposed to 12 GHz on the spectrum analyzer). We used a tunable Erbium doped fiber ring laser as the pump and a temperature controlled DFB laser as the probe. Both the pump and the probe were polarization controlled and amplified before being coupled into the SOA. The FWM polarization was selected at the output of the SOA with a polarizer, and combined with a co-polarized optical local oscillator (LO), an external cavity tunable semiconductor laser. The beat note between the FWM signal and the local oscillator was detected with a high-speed PIN photodetector, amplified and recorded in a microwave frequency spectrum analyzer. The frequency of the probe and the local oscillator were adjusted for each data point so that the beatnote between the FWM signal and the LO was at a fixed frequency which eliminates the frequency response of the detection electronics in the data. The residual noise on the TE to TM ratio data stems primarily from intensity noise of the Erbium doped fiber ring laser. Fig. 4.6(a) shows the measured optical powers in the TE and TM components of the FWM signal as a function of detuning frequency; their ratio P_1^s/P_2^s is plotted in Fig. 4.6(b). The contribution associated with coupling of the carrier density modulation from the tensile to the compressive wells is clearly seen at low detuning frequencies, and becomes negligible at $\Omega \approx 40$ GHz.

In order to extract quantitative information from the data, we consider a simple model for the interwell carrier dynamics. The transfer of carriers between adjacent wells mainly results from phonon-assisted quantum capture/escape processes between the quantum well states and the overlying continuum of 3D states of the

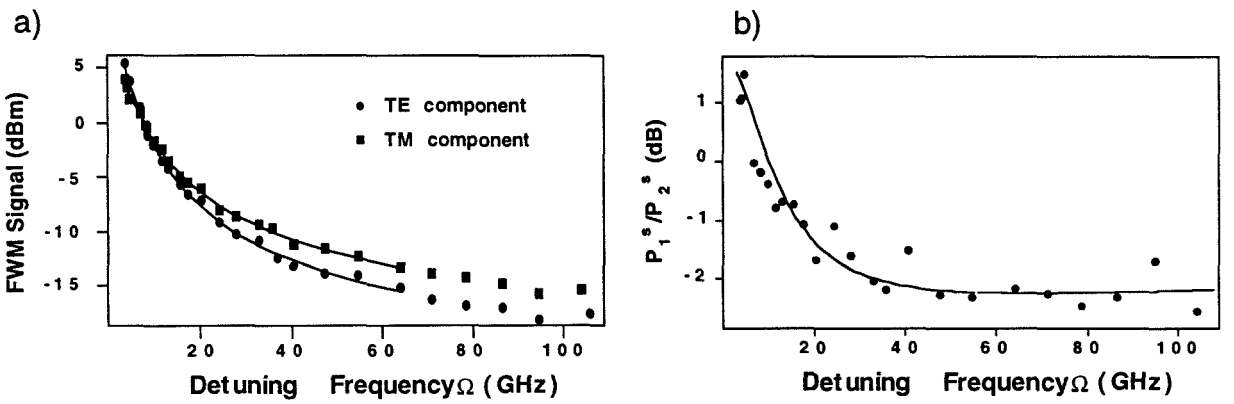

Figure 4.6: (a) Optical powers in the TE (circles) and TM (squares) components of the FWM signal. (b) TE over TM signal ratio versus detuning frequency. The continuous lines are fits to the model theory discussed in the text. The fit is only shown to detuning frequencies up to 60 GHz because beyond that value carrier heating, not included in the model, becomes important. However, since its contribution is approximately the same for both the TE and TM components, the fit remains good for their ratio in the right figure. An approximate interwell transport lifetime of 16 ps is inferred from the data.

SOA waveguide layer [10, 11]. We assume that the 2D states of each well are coupled to wavepackets of 3D states localized near the same well, whose dynamics is dominated by classical diffusion (drift is of minor importance in a forward-biased structure [10, 11]). Interwell transport by tunneling is neglected because the width of the barriers is too large for this process to be effective. Finally, the dynamics of holes (which are known to have a shorter capture lifetime [11]) are assumed to adiabatically follow that of the electrons and is not considered explicitly.

These assumptions lead to the following set of rate equations :

$$
\begin{aligned}
-i\Omega N_{2D}^{T} &= -\left(\frac{1}{\tau_s}+\frac{1}{\tau_{esc}^{T}}\right)N_{2D}^{T}+\frac{N_{3D}^{T}}{\tau_{cap}^{T}}-\frac{\epsilon_0 cn}{2}\frac{g_2^{T}}{\hbar\omega_p}E^{p}\,(E^{q})^{*}\,0 \\
-i\Omega N_{2D}^{C} &= -\left(\frac{1}{\tau_s}+\frac{1}{\tau_{esc}^{C}}\right)N_{2D}^{C}+\frac{N_{3D}^{C}}{\tau_{cap}^{C}}.
\end{aligned}
\tag{4.2}
$$

Here N_{2D} is the harmonic component at the detuning frequency Ω of the density of electrons confined inside the quantum well under consideration and (N_{3D}) is the corresponding density of unconfined carriers above the well. τ_s, τ_{esc} and τ_{cap} are the recombination, escape and capture lifetimes respectively. Again, the superscripts T and C distinguish between quantities of tensile and compressive wells and in what follows we assume that the time constants do not depend on the type of well. The last term on the right-hand side of the top equation accounts for modulation of the carrier density by beating of the input waves in each tensile well (g_2 is the gain coefficient for TM polarized waves and n is the background refractive index). No such term is present in the second equation for the FWM polarization configuration considered here. Finally, the density of unconfined electrons N_{3D} above the quantum well satisfy

the diffusion equation with boundary values N_{3D}^{C} above the compressive quantum well, and similarly for the tensile well

$$-i\Omega N_b = -\frac{N_b}{\tau_s} + D\frac{\mathrm{d}^2 N_b}{\mathrm{d}z^2}, \tag{4.3}$$

subject to the boundary conditions $N_b(z_i^T \pm L_w^T/2) = N_{3D}^T$ and $D\frac{\mathrm{d}N_b}{\mathrm{d}z}(z_i^T \pm L_w^T/2) = \pm\frac{L_w^T}{2}\left(\frac{N_{3D}^T}{\tau_{cap}^T} - \frac{N_{2D}^T}{\tau_{esc}^T}\right)$ near the center z_i^T of the i^{th} tensile well, of width L_w^T (and similarly for each compressive well).[1]

The connection between the simple model of interwell dynamics just presented and the FWM experimental results of Fig. 4.6 is provided by Eq. 4.1 plus the relations $\chi_{TE,TM}^T \propto \chi_{TM,TM}^T \propto N_{2D}^T$ and $\chi_{TE,TM}^{C\leftarrow T} \propto N_{2D}^C$, where the proportionality constants are essentially independent of Ω, and can be evaluated following Ref. [4]. The continuous lines in Fig. 4.6 are the theoretical fits. Aside from unimportant multiplicative prefactors, the only physical parameters important in determining these curves are the capture and escape lifetimes, which are taken here to be $\tau_{cap} = 1.5$ ps, and $\tau_{esc} = 8$ ps respectively. On the other hand, the fits are relatively insensitive to the diffusion constant D (D= 5 cm^2 s^{-1}) as long as the diffusion length $L_D = \left|\sqrt{\frac{D\tau_s}{1-i\Omega\tau_s}}\right|$ is much larger than the barrier width L_b of 100 Å in the SOA under study. This is certainly the case for $\Omega < 100$ GHz. The agreement with the experimental data is excellent, except for the points at detuning frequencies in excess of about 50 GHz, where carrier heating (not included in our model) is known to cause an increase in the FWM

[1] Implicit in these boundary conditions are the two main simplifications of the model, namely (I) a periodic chain of pairs of oppositely strained wells is assumed, and (II) the finite width of the well is not considered in treating the diffusion process.

conversion efficiency [14]. Since this increase is approximately the same for both the TE and TM components, the fit remains good for their ratio in Fig. 4.6(b).

In light of its validity in reproducing the experimental data, the above model can also be applied to a numerical estimate of the interwell transport rate. A detailed expression for this quantity can be obtained by using the solution to the boundary-value problem of Eq. 4.3 to eliminate the 3D carrier densities from Eq. 4.2. This procedure introduces in the rate equation for N_{2D}^{C} a term proportional to N_{2D}^{T} (and vice versa), whose proportionality constant $1/\tau_t$ is the effective rate for the overall transport of modulated carrier distributions from a tensile well to a neighboring compressive well. Neglecting diffusion ($L_D >> L_b$) and the differences between the two types of wells, we find the simplified expression

$$\frac{1}{\tau_t} = \frac{1}{2\tau_{esc}} \frac{1}{1 - i\Omega\tau_{cap} L_b / L_w}. \tag{4.4}$$

At low detuning frequencies, where diffusion may be regarded as instantaneous, interwell transport is mainly limited by escape since capture is always faster [11]. Therefore $\tau_t = 2\tau_{esc} \approx 16$ psec. The factor of two appears because, if both types of wells have the same capture lifetime, each escaped carrier from a well can be transferred to an adjacent well or recaptured in the same well with equal probability.

In conclusion, the FWM experiment described here combined with a simple model allowed us to study the interwell transport lifetime for modulated carrier distributions in an alternating-strain SOA. We found that this lifetime is mainly determined by quantum escape from each well and we estimated the overall interwell transport rate

to be $\tau_t \approx 16$ ps.

4.4 TE-TM mixing

Polarization resolved FWM can also in principle be used to measure the dephasing time constant, τ_2, describing the lifetime of the optically induced coherence between degenerate spin states in a given band (see discussion in Chapter 3). Setting the polarization of one of the input waves exactly along the TE direction and that of the other wave along the TM direction should in principle generate a FWM signal resulting from the modulated phase coherence between spin-degenerate states of the conduction band. The study of this signal would give an insight into the dynamics of the spin-spin phase coherence, and in particular, it may be a way of measuring the lifetime associated with the decay of such coherence. This contribution to the FWM nonlinearity is expected to be faster than the usual spectral hole burning, and the large frequency detunings involved in resolving such ultra-fast phenomena will require careful elimination of propagation effects.

An attempt was made to measure this contribution with the setup shown in Fig. 4.7. We have used narrow linewidth sources (a high-power DFB laser, an external cavity laser and an Erbium doped fiber ring laser) so that the resolution bandwidth on the RF-spectrum analyzer could be set to below 10 MHz (not limited by the instantaneous linewidth of the lasers, but rather by the frequency stability of the external cavity laser over the sweep time of the rf-spectrum analyzer). Furthermore, we chopped the probe beam and fed the analog signal output of the spectrum analyzer to

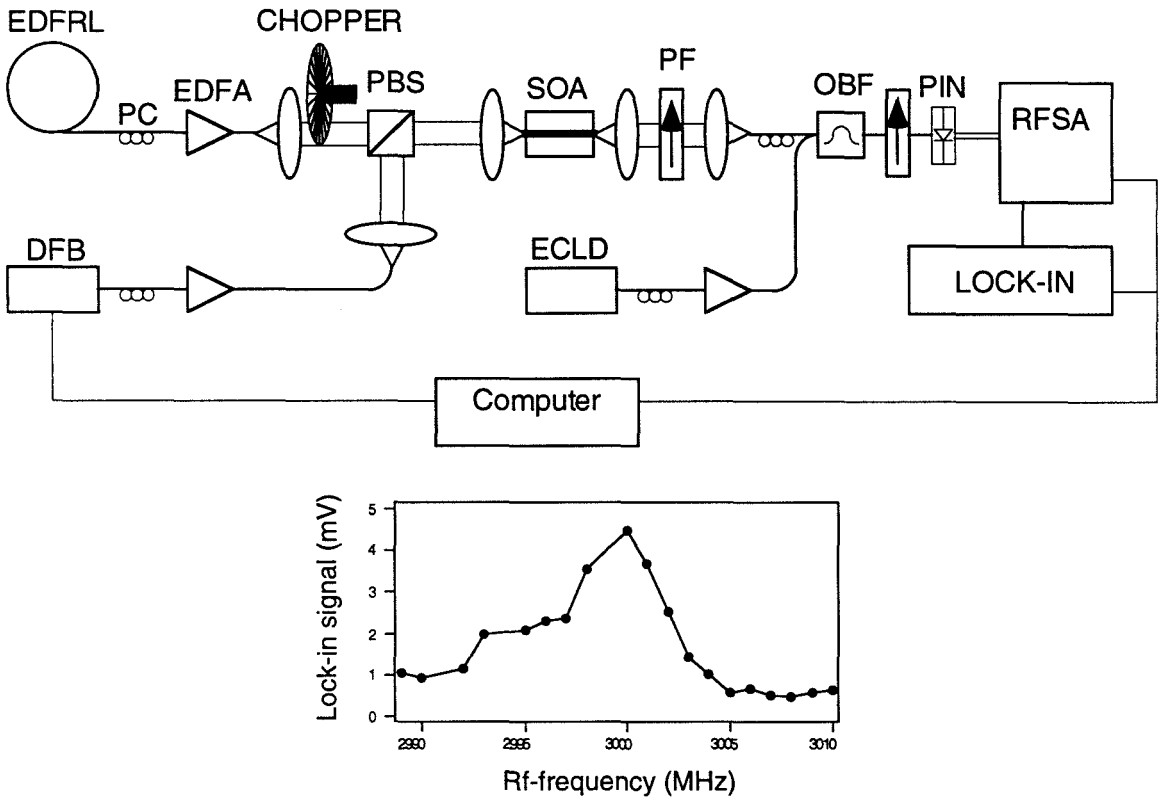

Figure 4.7: Experimental setup to measure the FWM signal induced through spin-spin coherence modulation. The computer control was used to scan the rf-frequencies while measuring the signal on the lock-in amplifier. It was also used to adjust the temperature of the DFB laser so that the beatnote between the FWM signal and the local oscillator was fixed at 3 GHz. The resulting trace is shown in the lower part of the figure, clearly showing the FWM signal beat with the local oscillator. The shoulder appearing to the left of the peak stems from occasional mode hops of one of the lasers during the integration time of the lock-in amplifier. The noise floor on the signal stems from modulated ASE noise from the SOA beating with the local oscillator (the carrier density in the SOA is modulated at the chopper frequency due to weak saturation of the amplifier by the probe beam). The acronyms appearing in the figure are explained in the Glossary.

a lock-in detector. This allowed us to further lower the noise floor on the FWM signal, since it reduces the shot noise contribution of the local oscillator (by reduction of the effective detection bandwidth) as well as the beat noise of the local oscillator with ASE from the SOA. The measurement required careful elimination of parasitic FWM signals generated in the fibers by the Kerr non-linearity (before the SOA). The pump and probe waves were therefore combined in air using a polarizing beamsplitter, just before being coupled into the device. Furthermore, it was necessary to use very high values for the FWM detuning frequency, since the very sensitive detection setup will detect the weak FWM signals generated by the residual component of the pump and probe along the orthogonal polarization direction. These parasitic mixing signals are identified by measuring the detuning frequency dependence, which reveals the usual roll-off sequence due to CDP CH and SHB, whereas the FWM due to the coherence modulation is expected to be flat (or strongly oscillating due to phase mismatch) over a frequency range extending well into the TeraHertz regime.

After taking all these precautions, we have measured what we believe is the FWM contribution due to the coherence modulation between spin degenerate states. The signal was very weak and strongly oscillating as a function of detuning frequency because of the phase mismatch. To estimate the amount of phase mismatch, we measured the refractive indices for the TE and the TM mode of the SOA (measuring the Fabry Perot ripple of the ASE along the TE and the TM direction). The difference was found to be quite large, $\Delta n = 0.03$, resulting in an estimated 30 dB of attenuation of the FWM signal. The weakness of the signal and its strong phase mismatch made

it impossible to map a sufficient detuning frequency range with this device.

Bibliography

[1] T. Durhuus, B. Mikkelsen, and C. Joergensen, *Journal of Lightwave technology*, **14**, p. 942, 1996.

[2] H. Yasaka, Hishii, Takahata-K, K. Oe, Y. Yoshikuni, H. Tsuchiya, *Electronics Letters* , **30**, p. 133, 1994.

[3] D. Marcenac, A. Kelly, D Nesset, D. Davis, *Electronics Letters* , **31**, p. 1442, 1995.

[4] G. P. Agrawal, *J. Opt. Soc. Am. B*, **5**, p. 147, 1988.

[5] J. Zhou, N. Park, J. W. Dawson, K. J. Vahala, M. A. Newkirk, and B. I. Miller, *IEEE Photon. Technol. Lett.*, **6**, p. 50, 1994.

[6] J. Zhou, N. Park, J. W. Dawson, K. J. Vahala, M. A. Newkirk, and B. I. Miller, *Appl. Phys. Lett.*, **63**, p. 1179, 1993.

[7] M. A. Newkirk, B. I. Miller, U. Koren, M. G. Young, M. Chen, R. M. Jopson, and C. A. Burrus, *IEEE Photon. Tech. Lett.*, **4**, p. 406, 1993.

[8] W. Rideout, W. F. Sharfin, E. S. Koteles, M. O. Vassell, and B. Elman, *IEEE Photon. Tech. Lett.*, **3**, p. 784, 1991.

[9] R. Nagarajan, T. Fukushima, S. W. Corzine, and J. E. Bowers, *Appl. Phys. Lett.* **59**, p. 1835, 1991.

[10] S. Weiss, J. M. Wiesenfeld, D. S. Chemla, G. Raybon, G. Sucha, M. Wegener, G. Eisenstein, C. A. Burrus, A. G. Dentai, U. Koren,B. I. Miller, H. Temkin, R. A. Logan, and T. Tanbun-Ek, *Appl. Phys. Lett.*, **60**, p. 9 1992.

[11] S. C. Kan, D. Vassilovski, T. C. Wu, and K. Y. Lau, *Appl. Phys. Lett.* **61**, p. 752, 1992.

[12] D. Vassilovski, T. C. Wu, S. C. Kan, K. Y. Lau, and C. E. Zah, *Appl. Phys. Lett.* **63**, p. 2307, 1993.

[13] N. Tessler, and G. Eisenstein, *IEEE J. Quantum Electron.*, **29**, p. 2230, 1993.

[14] J. Zhou, N. Park, K. J. Vahala, M. A. Newkirk, and B. I. Miller, *Appl. Phys. Lett.* **65**, p. 1897, 1993.

[15] G. Lenz, E. P. Ippen, J. M. Wiesenfeld, M. A. Newkirk, and U. Koren, *Appl. Phys. Lett.* **68**, p. 2933, 1996.

[16] R. Paiella, G. Hunziker, U. Koren, K. Vahala *IEEE J.of Selected Topics in Quantum Electronics* **3**, p. 529, 1997.

Chapter 5

Wavelength resolved FWM spectroscopy

5.1 Introduction

Sections 4.2 and 4.3 have shown how specific choices of the polarizations of the pump and probe fields can be used to selectively generate and probe the carrier density modulation in quantum wells. In particular, the interwell transport experiment showed how a rather simple experiment can yield a wealth of information about complicated processes such as quantum capture, escape and diffusion. The main conclusions of that experiment were that the interwell transport was predominantly limited by escape dynamics, and that the overall interwell equilibration time constant was 16 picoseconds. To extract the capture and escape time constants, a rate equation model was used to fit the data. Although this model was in very good agreement with the experimental data, it was not possible to isolate the individual contributions to

the interwell transport with a single measurement. In the first section of this chapter, I will describe how *wavelength* resolved spectroscopy can be used to isolate the dynamics of the capture process only. Since quantum capture is not the dominant contribution in the interwell transport, this experiment complements the results from the polarization resolved FWM measurement. Section 5.3 will be devoted to a different wavelength resolved FWM experiment where below-gap pump waves were used to isolate the contribution to FWM due to free carrier absorption.

5.2 FWM mediated by carrier capture

Quantum capture is the process by which charge carriers are transferred from the delocalized 3-D states above the quantum wells to the confined 2D states inside the wells. This process occurs through energy relaxation, mainly by emission of optical phonons, from states in the separate confinement layer (with a bandgap of 0.97 eV in this device) to the lasing transition (occurring at 0.8 eV). The rate at which these charge carriers relax to the lowest quantum well state is important in explaining the dynamic and spectral features of devices based on such structures. Furthermore, the phonons emitted in this process generate a significant amount of heat, which affects the performance of high-power quantum well lasers.

Common experimental methods to determine the time constants associated with the capture and escape dynamics include impedance measurements [1], ultrafast non linear spectroscopy [2], pump-probe measurements [3], or, as shown in the previous chapter, polarization resolved FWM. While they all involve the capture time constant

to some extent, these methods are often not very direct because a simplified model is required to extract the relevant number. In the work of Ref. [4], the idea of direct generation of a small signal modulation of the carriers in the 3D barrier states has been proposed.

The experiment presented in this section is an extension of that work, where instead of generating the modulation of the carriers in the barriers with a directly modulated laser beam, the modulation is generated by optical photomixing of two detuned pump lasers. This, combined with optical heterodyne detection extends the frequency range from 20 GHz (limited by the modulation and detection electronics in [4]) to about 240 GHz. This is well beyond the typical values for the intrinsic capture rate, so it can in principle be measured directly with no need for involved theoretical fits. On the other hand, since the pump and probe wavelengths are so far apart (1.31 μm and 1.55 μm respectively), propagation effects have to be taken into account when interpreting the results.

The principle of the experiment is shown in Fig. 5.1, as well as the layout used to perform the measurement. The two pumps (DFB lasers in the 1.31 μm wavelength band) are combined in a fiber bi-directional coupler, and their polarization is set along TE at the input of the amplifier. The photon energy of these lasers is within kT of the onset of continuous optical transitions between the states in the separate confinement layer. Absorption of these detuned lasers creates the carrier modulation in those states. By changing the temperatures of the DFB pump lasers, we can precisely control their detuning, and hence the rate at which the carriers are modulated.

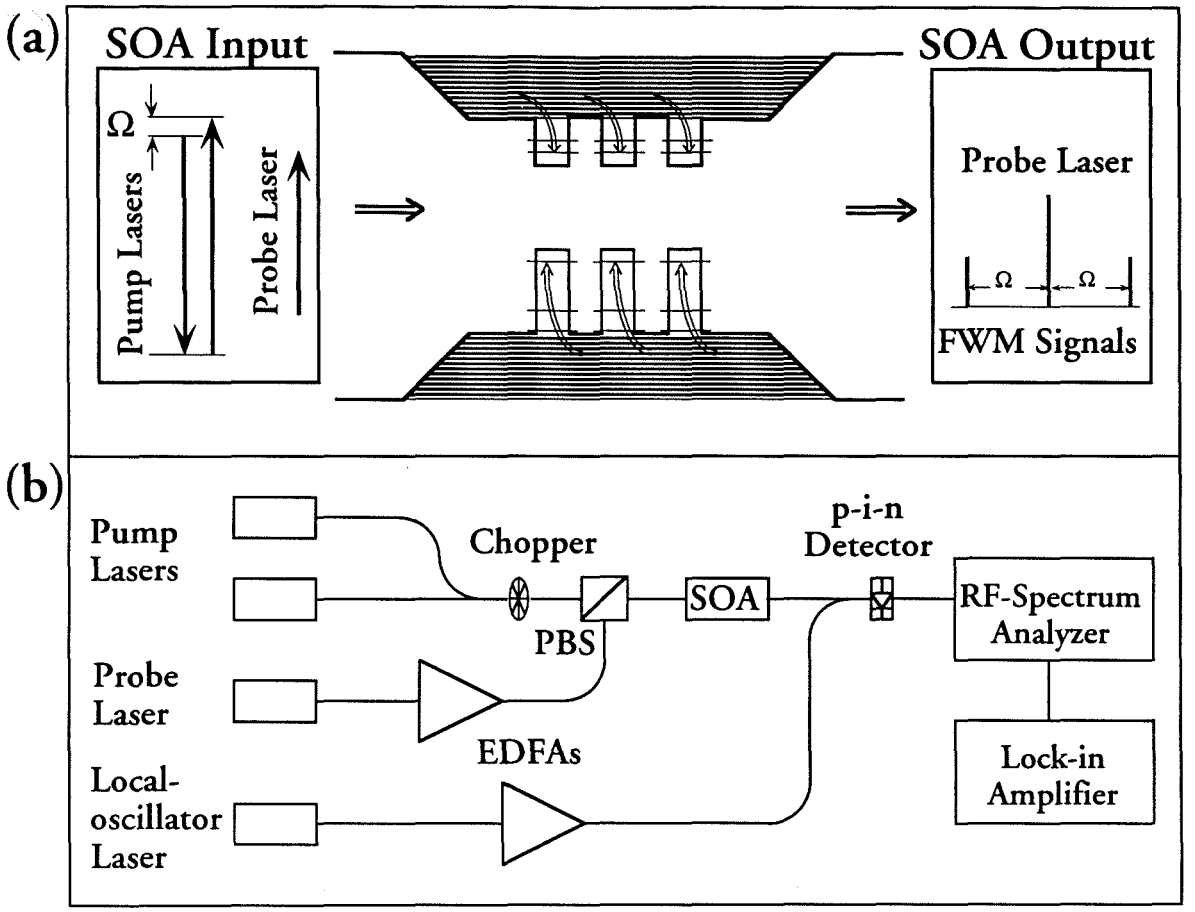

Figure 5.1: (a) Pictorial description of the experiment and (b) schematics of the experimental layout (b). The total pump power at 1.3 μm was 2 mW and the probe power was 17 mW at the SOA input. The SOA was 780μm long and biased at 100mA. The DFB laser frequencies were adjusted by temperature control. To remove the frequency dependence of the RF electronics, the local oscillator was at a fixed detuning relative to the FWM signal. Lock-in detection was also used for improved sensitivity.

The probe wave (in the 1.55 μm wavelength band) is linearly polarized along the TM direction and combined with the pumps in a polarizing beam splitter. As the probe wave travels through the amplifier, it experiences gain from optical transitions between the lowest states of the quantum wells. If some of the carrier modulation induced by the absorption of the pump waves in the separate confinement states is transferred to the lowest quantum well states, this gain is modulated. The probe wave is then be scattered by this modulated gain into the FWM signals.

To avoid the complications which arise from measuring a compound capture rate for tensile and compressive wells of different size, we use a TM polarized probe wave which interacts only with the tensile wells. The polarization of the pump waves is not as important since the transitions of the continuum of states in the separate confinement layer are not expected to exhibit any anisotropy. [1] The strength of the gain (and index) gratings at the probe wavelength due to the photomixing is small. Consequently, the FWM sidebands generated on the probe wave are weak, and despite the heavy saturation by the probe wave, they are below the ASE noise level of the SOA (measured with the 0.1 nm resolution bandwidth of our spectrum analyzer). For this reason, an optical heterodyne measurement similar to the one presented Section 4.4. is used. Furthermore, to cover the large dynamic range required to span the full

[1] This suggests an interesting extension of this experiment, combining polarization and wavelength resolved FWM spectroscopy in compressive-strained quantum wells. In that case, the continuum of states can be modulated through both polarizations components of the pumps while the confined states can only interact with the TE components of the pumps. A comparison between the FWM signal generated in each case can then reveal the distinction between inter-subband energy relaxation and carrier capture of unconfined carriers.

detuning range, and to improve the signal to noise ratio of the FWM, we chop one of the pump beams and use a lock-in detector to measure the beatnote between the local oscillator and the FWM signal. The SOA device is the same as the one used in the interwell experiment, and it is also biased at 100 mA. The power level of the beams before the SOA is approximately 2 mW for pump power (both lasers) and 17 mW for the probe. The optical power of the local oscillator is 4 mW at the photodetector.

The measured strength of the FWM sideband as a function of pump detuning frequency is shown in Fig. 5.2. As indicated by the straight lines in the figure, the data shows an initial roll-off with a 20dB/decade slope, up to about 85 GHz, followed by a steeper decay at higher detuning frequencies (the second line has a 40 dB/decade slope). The initial slope of the decay comes about from the stimulated carrier recombination of the carriers. The actual value of the corner frequency for this first pole is not important here and it is expected to be similar to that measured in the experiment described in Section 4.2. This feature simply reflects the limited rate at which the gain can be modulated, and is not related to the capture process per se. For this reason, we normalized its contribution out of the data. The result is shown in the inset of the figure, and the pole at 88 GHz now clearly appears, but other features at higher frequency are also evident.

The most straight forward interpretation of this data is done with a simple rate equation model, analogously to the one we used to fit the data from the interwell experiment :

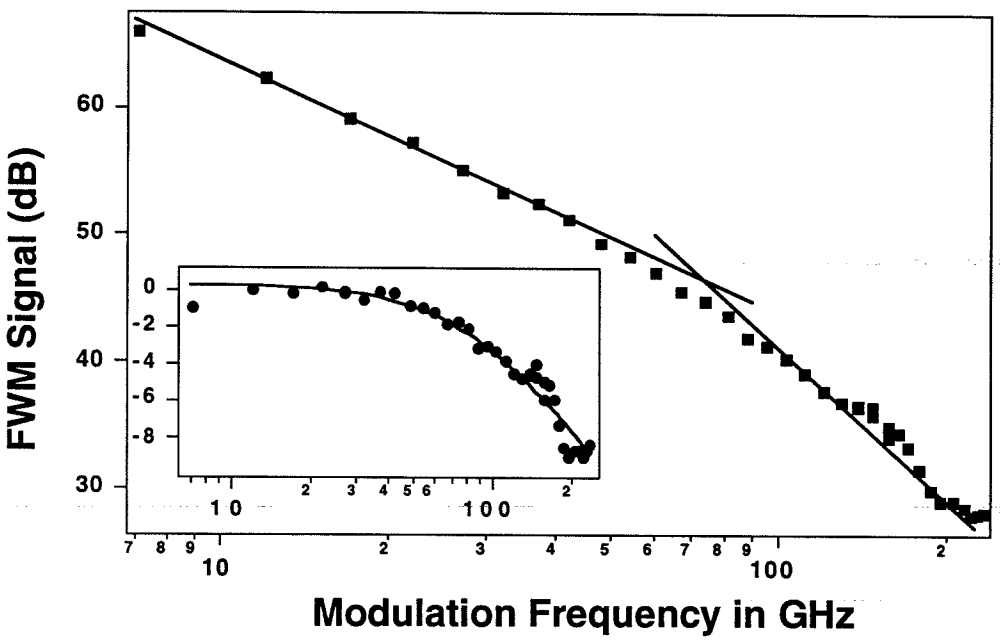

Figure 5.2: Measured optical intensity of the FWM signal versus modulation frequency. As emphasized by the continuous lines, the slope of the data changes from -20 to -40 dB/decade with increasing detuning frequency. The inset displays the same data with the initial 20 dB/decade roll-off subtracted. The continuous curve is a fitted single-pole frequency response at 88 GHz $= 1/(2\pi \times 1.8\text{psec})$.

$$-i\Omega N_{2D}^{(\Omega)} = -\left(\frac{1}{\tau_s}+\frac{1}{\tau_{esc}}\right)N_{2D}^{(\Omega)}+\frac{N_{3D}^{(\Omega)}}{\tau_{cap}},$$

$$-i\Omega N_{3D}^{(\Omega)} = -\left(\frac{1}{\tau_s}+\frac{1}{\tau_{cap}}\right)N_{3D}^{(\Omega)}+\frac{N_{2D}^{(\Omega)}}{\tau_{esc}}+g_{3D}^{(\Omega)}. \tag{5.1}$$

Here $N_{2D}^{(\Omega)}$ denote the small-signal density of carriers confined inside each (tensile) well. $N_{3D}^{(\Omega)}$ is the density of unbound carriers localized near the same quantum well and directly modulated by the beating of the pump waves, at a rate $g_{3D}^{(\Omega)}$. τ_{cap} and τ_{esc} are the intrinsic capture and escape lifetimes, and τ_s si the stimulated carrier lifetime. Notice that we are not including in this model any effect related to transport in real space, such as diffusion or drift, which is appropriate for excitation near the barriers band-edges. Furthermore, we are assuming that the phonon modes involved in the capture/escape processes are not significantly perturbed from their equilibrium occupancy, so that their dynamics need not be considered. Finally, we do not explicitly consider the capture of both conduction-band electrons and holes, since the frequency response measured in this experiment should be dominated by the slower carrier type (presumably the electrons [5]).

The field amplitude of the FWM signal as a function of Ω is proportional to the amplitude of the carrier density modulation that generates it, $N_{2D}^{(\Omega)}$. Solving the coupled set of equations 5.2, one finds

$$N_{2D}^{(\Omega)} = \frac{1/\tau_{cap}}{(-i\Omega+1/\tau_s)(-i\Omega+1/\tau_{cap}+1/\tau_{esc}+1/\tau_s)}g_{3D}^{(\Omega)}. \tag{5.2}$$

On the basis of this simple model we expect the FWM conversion efficiency to exhibit one pole at $1/\tau_s$ and another at $(1/\tau_{cap}+1/\tau_{esc}+1/\tau_s)\approx 1/\tau_{cap}$ since in general the

capture lifetime is shorter than both the stimulated recombination and the escape lifetimes (see 4.2 and 4.3). As a result, τ_{cap} can be directly read off the experimental data provided that the frequency dependence is entirely ascribed to the carrier-density modulation response described by Eq. 5.2. If we assume that this is indeed the case for the data of Fig. 5.2 , we immediately obtain an electronic capture lifetime of 1.8 psec. This estimate is consistent with the measurement of the interwell transport rate in the same SOA presented in section 4.3, where a value of 1.5 psec for τ_{cap} (and 8 psec for τ_{esc}) was inferred.

Although the above model seems to provide a good explanation for the experimental data, and is in agreement with the results from the interwell measurement, it cannot explain the two small features observed at 140 GHz and at a 200 GHz, which bear some resemblance to the two first maximas of a phase matching curve. Given the large wavelength separation between the pump and the probe lasers, the wavenumber mismatch Δk can be significant for this FWM process, and can actually produce similar features in the conversion efficiency at these frequencies. We have been able to fit the above results successfully with a damped phase-matching curve. However, the damping coefficient necessary to reproduce both features as sharply as they appear in the data corresponds to a very small absorption coefficient for the pump lasers (a factor of 10 smaller than the value measured on the device). An alternative explanation of these features could also be that they are the result of a resonance in the interaction between the captured electrons an the phonon modes involved in the process. The physical picture would then be similar to the relaxation

oscillations observed in a laser where, at a given frequency, electrons and photons populations are resonantly coupled and 'slosh' back and forth.

In view of this ambiguity regarding the nature of these high-frequency features, we cannot make a definite claim for the capture time constant measured above. Instead, the value of 1.8 ps should be regarded as an upper limit to the actual value for the capture time constant pending the resolution of the phase matching issue. In order to resolve this question, the experiment should be repeated in a configuration where the interaction length over which the FWM signal is generated is shorter. This is possible by either increasing the photon energy of the pump waves or reducing the bandgap of the separate confinement layers (or that of the barriers in between quantum wells). All of these changes would increase the absorption coefficient of the pump lasers thereby reducing the interaction length. Unfortunately none of these approaches were accessible to us with our current setup.

5.3 Below-gap FWM

In the general theory of FWM, we have mentioned that the carrier heating contribution can be caused by two distinct mechanisms: stimulated recombination and free carrier absorption. The contribution from free carrier absorption is expected to be a weaker contribution to the non-linear gain [6], but experimental evidence of their relative strengths has not been done with FWM to date. The issue has been extensively studied with pump-probe techniques [7, 8, 9], where either one or both waves were tuned across the bandgap. The results consistently showed a transient index

recovery associated with the carrier temperature relaxing to the lattice temperature. This effect has a time constant on the order of 1 ps and is ascribed to the carrier heating by free carrier absorption, but the strength of this mechanism relative to the stimulated emission contribution or spectral hole burning was not quantified.

As for the case of pump-probe experiments, wavelength resolved FWM spectroscopy can in principle be used to selectively probe the carrier density modulation due to free carrier absorption only. In the experiment presented here, we used two 1.55μm pump lasers, and measured the FWM signal generated in a semiconductor optical amplifier with a band edge at 1.31μm (for details about the structure of this amplifier, see [10]). All the waves were therefore 170 meV below the bandgap, and the FWM conversion measured does not involve direct band-to-band transitions. In fact, the two only possible contribution to the FWM signal are from carrier heating by free carrier absorption or four-photon processes similar to spectral hole burning. If the carrier heating contribution from free carrier absorption is dominant, then we expect the physical picture to be that the absorption of the pump and the emission of a probe photon create a temperature modulation (which in this case modulates only the refractive index of the active medium) and the pump wave is subsequently scattered by this index modulation into a FWM sideband. This process is limited by the carrier temperature relaxation trough the carrier-phonon interaction, and from the experimental results of Fig. 2.2 we expect it to be much slower than spectral hole burning processes. The time constants measured by pump-probe experiments suggest that the conversion efficiency for the latter should decrease as the detuning

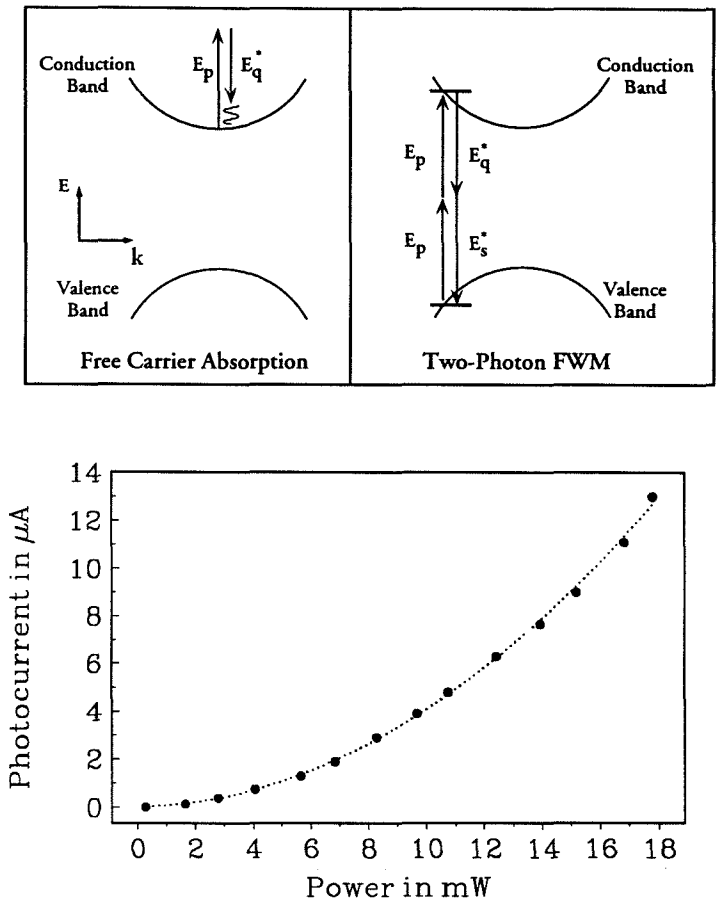

Figure 5.3: Top: Below-gap FWM processes from carrier heating and resonant two photon transitions. The left schematic shows the generation of the modulation by free carrier absorption. The resulting refractive index modulation is then responsible for the scattering of the pump (this process is not shown). The right diagram shows the two-photon FWM process, in which two pump photons are absorbed and a probe and a signal photon are re-emitted. The latter process is expected to be accompanied by a two-photon current, as seen in the lower figure. Bottom: Current induced by two-photon absorption of light below the bandgap. The photocurrent depends quadratically on the total input power, as indicated by the fit (dashed line).

frequency exceeds a few hundred GigaHertz, as is the case for the carrier heating due to stimulated recombination. On the other hand, the spectral hole burning contribution is expected to be a much faster process and should have a flat response up to very high detuning frequencies (the damping rate is this case is the dipole lifetime τ_1). It is not clear what the exact transitions involved in the generation of this signal are, but a strong candidate is the one shown in the right inset of Fig. 5.3, involving two-photon transitions occurring away from the Brillourin zone center (with a resonance at the second intermediate state, where the bandgap matches the energy of a two-photon transition). We expect this to be the case because we measured a significant two-photon absorption current induced by the input waves, also shown in Fig. 5.3. Other four-photon processes are possible however, involving for instance intervalence band transitions or off-resonance FWM at the zone center. Further experiments are required to confirm which is the dominant contribution in this configuration.

We used a setup similar to the one used in the interwell experiment with an additional fiber ring laser instead of a DFB laser to measure the below-gap FWM signal versus detuning frequency. The pump and the probe waves were polarized along the TM direction, for which the free carrier absorption contribution to the index is expected to be stronger [11]. The resulting FWM signal versus detuning frequency is shown in Fig. 5.4, and we can see that the signal remains constant to detuning frequencies as high as 1.5 THz. This rules out the possibility of a signal generated by carrier heating through the absorption of free carriers. Based on the observations described above, we conclude that the dominant process responsible for

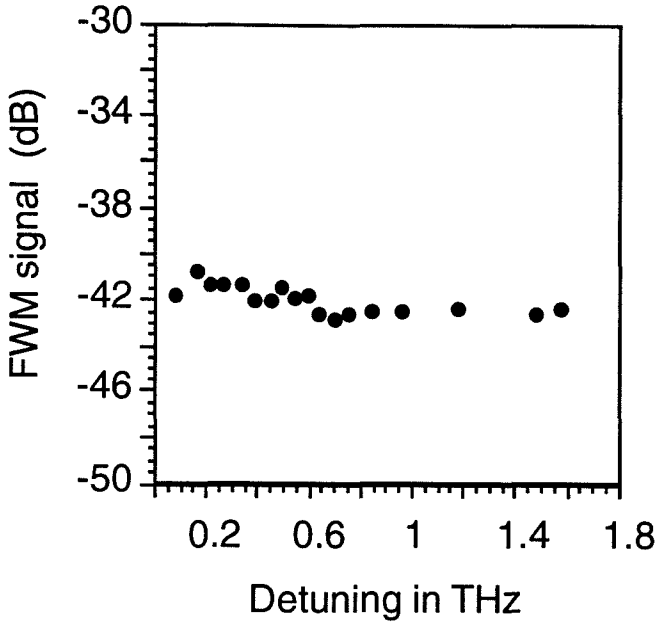

Figure 5.4: Below-gap FWM signal versus pump-probe detuning.

this FWM signal is the 2-photon process shown in the right inset of Fig. 5.3.

The fact that we did not observe a time constant pertinent to the heating through free carrier absorption does not mean that this process is non-existant. There are several reasons that could explain why it was found to be weaker than the spectral hole burning contribution. First, it can be due to the fact that the device used for this experiment has a low free carrier absorption coefficient, resulting from the particular optical/electrical confinement in the vertical direction (the waveguide was designed for very effective carrier injection with a decoupled optical confinement [10]). Second, it can be that the heating by free carrier absorption has a small index contribution, which would result in a weak scattering of the pump into the FWM signal in this experiment. Following the analysis of Ref. [12], the strength of the index grating

due to the carrier heating is determined by the gain-index coupling factors for the temperature: $\alpha_T = \partial_T Re[\chi]/\partial_T Im[\chi]$. For small values of α_T, the contribution of the carrier heating will result predominantly in a gain grating whereas for large values of α_T, the gratings are predominantly in the refractive index. Calculations of these factors have suggested that their value was small [12], which would translate into weak index gratings, and a small FWM signal.

Bibliography

[1] S. Weisser, I. Esquivias, P. Tasker, J. Ralston, B. Romero, J., *IEEE Photon. Technol. Lett.*, **7**, p. 1421, (1994).

[2] J. Shah, *Ultrafast Spectroscopy of Semiconductors and Semiconductor Nanostructures*, Berlin, Germany: Springer-Verlag, 1996.

[3] S. Weiss, J. M. Wiesenfeld, D. S. Chemla, G. Raybon, G. Sucha, M. Wegener, G. Eisenstein, C. A. Burrus, A. G. Dentai, U. Koren, B. I. Miller, H. Temkin, R. A. Logan, and T. Tanbun-Ek, *Appl. Phys. Lett.* **60**, p. 9, (1992).

[4] D. Vassilovski, T. C. Wu, S. Kan, K. Y. Lau, and C. E. Zah, *IEEE Photon. Technol. Lett.*, **7**, p. 706, (1995).

[5] S. C. Kan, D. Vassilovski, T. C. Wu, and K. Y. Lau, *Appl. Phys. Lett.* **61**, 752, (1992).

[6] M. Willatzen, A. Uskov, J. Mork, H. Olesen, B. Tromborg, A. Jauho, *IEEE Photon. Technol. Lett.*, **3**, p. 606, (1991).

[7] K. Hall, G. Lenz, E. Ippen, U. Koren, G. Raybon, *Appl. Phys. Lett.*, **61**, p. 2512 (1992).

[8] C. Sun, H. Choi, C. Wang, J. Fujimoto, *Appl. Phys. Lett.*, **62**, p. 747 (1993).

[9] C. Hultgren, D. Dougherty, E. Ippen, *Appl. Phys. Lett*, **61**, p. 2767 (1992).

[10] S. Hausser, H. Maier, R. Germann, C. Harder, *IEEE J. of Quantum Electronics*, **29**, p. 1596 (1993).

[11] S. Murata, A Tomita, A. Suzuki, *IEEE Photon. Technol. Lett.* **5**, p. 16 (1993).

[12] A. Uskov, J. Mϕrk, and J. Mark, *IEEE Photon. Technol. Lett.* **30**, p. 1769, (1994).

Chapter 6

Single-pass FWM wavelength converters

This chapter is the beginning of the second part of this thesis, devoted to system applications of the four-wave mixing is semiconductor optical amplifiers.

6.1 Introduction

There are three approaches to upgrade the capacity of an all-optical network. The first is to increase the optical bandwidth in the link (currently limited by the fiber amplifier gain spectrum), so that it can accomodate more WDM channels. The second is to increase the spectral efficiency of the WDM channels, by reducing the separation between the different channels and/or increasing their bit rates. The third is to utilize the bandwidth of existing networks more effectively. This last option, when performed on the optical layer, is where wavelength converters are likely to become

of importance. In current networks, the system requirements on such converters are quite easy to accommodate, and can be implemented in a simple manner using a back-to-back receiver/transmitter in conjunction with multiplexers and space switches. However, as the system requirements evolve, it is likely that the optimal conversion scheme will become all-optical. In fact, field trials with all-optical cross-gain/phase modulators have been conducted recently using commercially available wavelength converters (Alcatel).

Four-wave mixing is a viable alternative to the cross-gain and cross-phase modulation techniques, and has some unique features such as bit rate transparency, modulation format transparency, largely unrestricted wavelength mapping, simultaneous multichannel conversion and the inherent optical phase conjugation (a review of system level demonstrations can be found in [1]). Although some of these features are not required in current systems, there is no particular reason to believe that this should remain true in the future. Therefore, it is important to address some of the additional challenges this technique has to overcome to be used in a system environment. In particular, this chapter will address the issue of the limited conversion span due to the FWM efficiency roll-off at high detunings as well as of the polarization dependence of the converter.

6.2 Wide span conversion

The limit on the span of a FWM wavelength converter is set by the power and signal-to-noise ratio of the converted signal. As the detuning between the pump and the

input signal is increased, the conversion efficiency drops (See Fig. 2.2), and eventually the amplified spontaneous emission (ASE) noise generated by the optical amplifier induces errors upon detection of the digital information contained in the converted signal. One method to overcome this limitation is to operate the semiconductor optical amplifier in a saturated regime. This has the benefit of lowering the ASE noise floor (strong stimulated emission reduces the population inversion and hence the gain and the spontaneous emission rate) and simultaneously providing a good conversion efficiency because of the high pump power used to saturated the amplifier. This is done using a high-power EDFA. Since this high-power EDFA tends to generate a significant amount of ASE noise, we use an ASE noise filter to carve out the noise in the spectral region where the FWM signal will be generated [2]. The resulting wavelength converter is somewhat more complicated, as shown in the shaded area of Fig. 6.1, but we will show in this chapter that the resulting performance is very adequate for system applications.Increasing the input power to the SOA does not improve the performance of the converter indefinitely, because the saturation of the gain also translates into a saturation of the four-wave mixing non-linearity. It has been observed [3, 4] that for single-pass SOAs there exists an "optimum" value of the pump power that maximizes the FWM conversion efficiency.

A second way to improve the performance of FWM wavelength converters is simply to increase the length of the mixing device. This has been predicted and verified experimentally in a number of publications [4], but at time of our experiment, no system level demonstrations had been performed to confirm this. Using long amplifiers

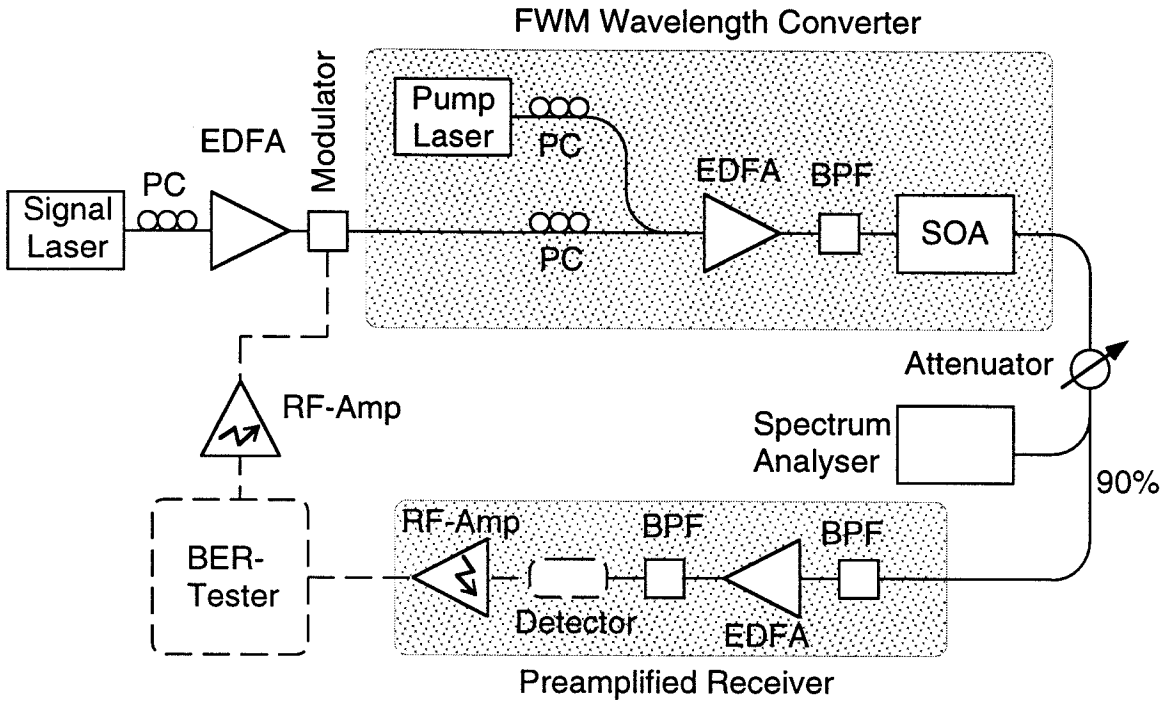

Figure 6.1: Schematic of the experimental setup to measure the bit-error rates for the wavelength conversion. PC stands for polarization controller, EDFA for Erbium doped fiber amplifier, BPF for bandpass filter (all 1 nm bandwidth, except the one just before the SOA), SOA for semiconductor optical amplifier, BER for bit error rate. Dashed lines carry electrical (RF) signals.

(typically a few millimeters long) in principle requires very good anti-reflection coatings in order to prevent lasing action in the cavity, although in most cases the high input power saturates the gain sufficiently so that it remains below the round-trip losses of the device. In the reminder of this section, we will present the results from a system level experiment, where we have experimentally verified the performance improvements associated with long SOA devices.

The device used in this experiment is a fiber pigtailed bulk SOA device with a ridge waveguide structure and anti-reflexion coated angled facets [5]. It is 1.5 mm long, has a polarization independent gain, a peak of the fiber-to-fiber signal gain at a wavelength of 1665nm, and equal to 24 dB (limited by ASE induced gain saturation). Under heavy bias (670 mA) and optical saturation conditions (40 mW of total optical power into the device) used in the FWM experiment, the gain peak shifts to 1575nm, which means that all conversion experiments were actually done well below the peak gain wavelength (or at energies above the peak gain). For the wavelength down-conversions, this improves the converter performance because the pump and the probe are still very effective in depleting the carrier inversion (they are close to the peak gain). At the same time, the converted signal is located in a low gain region, where the amplifier generates less ASE noise. In terms of the conversion noise performance, the reduced gain for the converted signal is largely offset by this lower noise floor (the conversion efficiency is primarily given by the amount of gain and power available in for the pump and probe waves). On the other hand, for wavelength up-conversions (and with the wavelength sources available to

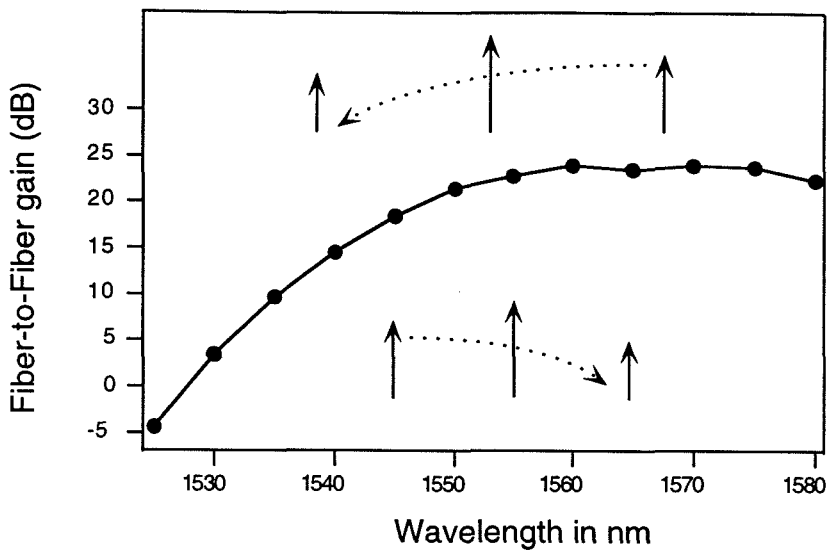

Figure 6.2: Fiber-to-fiber gain spectrum of the SOA. The arrows show the location of the signals for the wavelength conversion.

us) the position of the gain peak at high wavelength is a disadvantage, because the pump is not as effective in saturating the gain, and the converted signal is in a high noise region of the amplifier. The spectrum of the small signal gain of the amplifier is shown in Fig. 6.2, and the positions of the waves for up- and down-conversions are indicated in the figure. This emphasizes another important point in the design of a high-performance FWM wavelength converter : for a given range of conversions to be performed, the gain spectrum should be located accordingly. The noise and saturation are not necessarily the only concerns in this regards, and the recent results by Kelly et. al. in [7] indicate that the position of the pump wavelength relative to the gain peak can be used to improve the non-linear susceptibility as well.

The experimental setup to test the performance of the FWM converter in a system

environment is shown in Fig. 6.1. The setup uses a Hewlett Packard bit-error-rate analyzer consisting of a clock source, a pattern generator, an error performance analyzer and a microwave transition analyzer (HP 70800 Series). This generates a pseudo-random bit stream (PRBS) of non-return-to-zero (NRZ) data at 10 Gigabits per second. This signal (1 Volt peak-to peak modulation) is amplified in a high power microwave amplifier (7 Volts peak-to-peak modulation) and used to drive one of the phase arms of a Lithium Niobate Mach-Zehnder modulator. The Voltage required to shift the phase of the modulator arm by π is 12 Volts, thus the extinction ratio is not optimal and is strongly dependent upon the operating point. Good extinction ratios are achieved with a significant power penalty, which called for an additional EDFA before the modulator. Putting the EDFA before the modulator instead of after has the advantage of having a smaller amount of optical power in the logical zeros (no added ASE noise), but requires constant adjustment of the bias point of the modulator, which tends to drift when a large optical input power is used. The BER versus received power traces are very sensitive to the extinction ration of the original signal, and are recorded while constantly monitoring the operating point of the modulator with an extra 5% tap and a power monitor right after the modulator. The extinction ratio between the logical ones and zeroes achieved this way is typically 6 to 8 dB. The modulator performance is polarization dependent, and a polarization controller is necessary to optimize the extinction ratio. The pump and the probe then go through individual polarization controllers to align their polarizations at the input of the SOA. They are combined in an 80:20 coupler (the 20% port is for the probe and

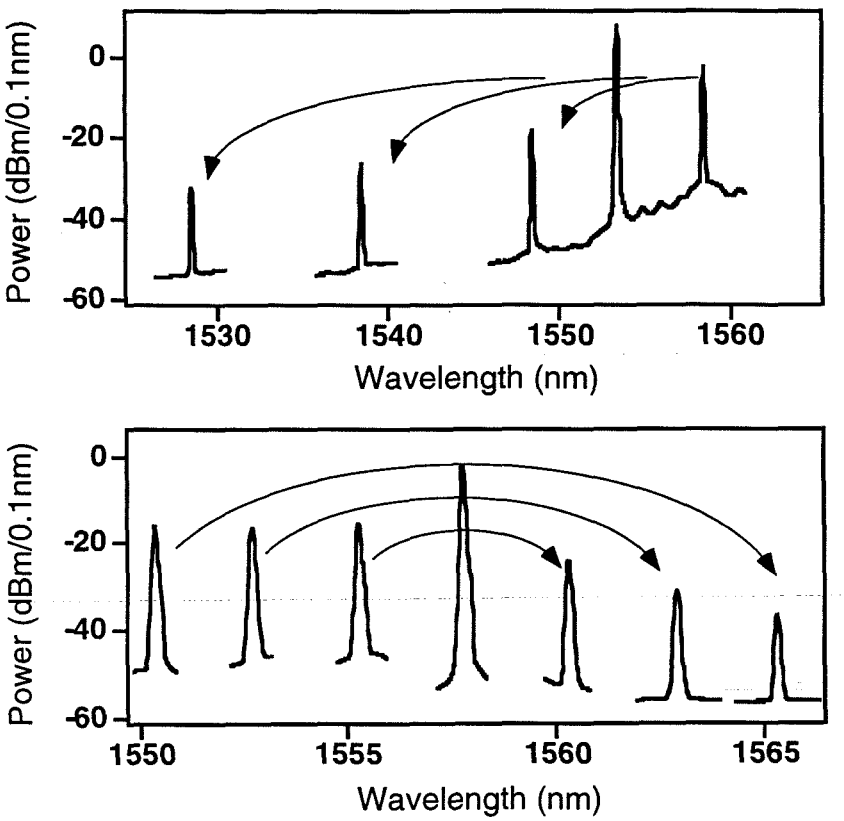

Figure 6.3: Spectra measured at the output of the SOA (0.1 nm resolution bandwidth). The top figure shows the down-converted signals for the 30, 20 and 10 nm shifts (from left to right). For the smallest shift, we also show the pump and the input signal. The pump wavelength was tuned to lower wavelengths at constant power to achieve the larger shifts. The bottom figure shows the up-converted signals for the 5, 10 and 15 nm shifts (from right to left). In this case, we changed the input signal wavelength and the pump remained the same for all three shifts.

the 80% for the pump). This coupling ratio was chosen so that the pump to probe ratio at the output of the converter, including the gain dispersion in the high-power EDFA and the SOA, was 10 dB, a value which was found to minimize errors due to cross-gain modulation of the pump while maintaining good conversion performance. The waves were then fed to the high-power EDFA. The optical power at this point was kept above -3 dBm to fully saturate the EDFA and get as much power as possible into the SOA. We spliced the output of the EDFA to the ASE Prefilter (a 9 or 15 nm optical passband filter centered over the pump and the probe) and the light is then coupled into the SOA. The amplifier bias is set at 670 mA and the device is temperature controlled by a thermoelectric cooler. The spectra shown in Fig. 6.3 are measured directly after the SOA. To eliminate the pump and the probe waves, we use a 1 nm optical bandpass filter centered on the FWM signal after the converter. Since the pump power is usually 30 to 50 dB stronger than the FWM signal, this filter does not completely suppress the pump wave; in fact for the small detunings the pump wave is still stronger than the FWM signal at the input of the preamplified receiver. The receiver consists of a two-stage EDFA, with a short low-noise initial amplifier section followed by a longer power amplification stage. The performance and the details of the construction of this amplifier are described in detail in [6]. The optical amplifier is followed by another 1 nm bandpass filter, to eliminate the residual amount of pump and ASE power. The optical to electrical conversion was done with a HP 11982 A lightwave converter followed by a Veritech electrical preamplifier after which 10% of the signal is fed to the microwave transition analyzer and 90% to the

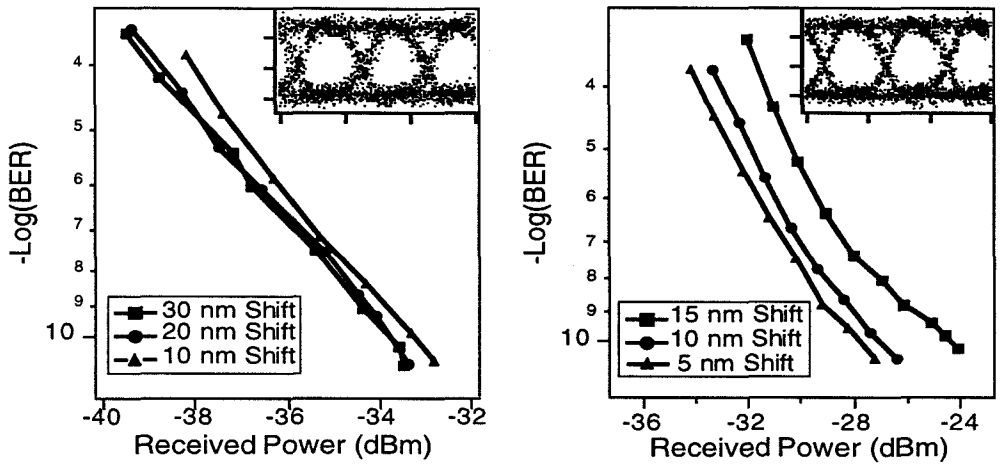

Figure 6.4: BER vs. received signal power for the shifts in Fig. 6.3. The received signal power was measured at the 10% tap after the attenuator with 0.2 nm resolution bandwidth. The eye diagram in the inset corresponds to the largest shift in each case, with no attenuation.

bit error rate tester. The microwave transition analyzer is used to analyze the digital waveforms, and proved very useful in system 'debugging' by looking at the distortion induced on PRBS and user specified 8 bit sequences. The results of the bit error rate testing are shown in Fig. 7.2. In order to measure the penalty induced by the four-wave mixing wavelength conversion, we also measured the bit error rates for the original signal. To obtain a comparison, the probe laser was tuned to the wavelength corresponding to the converted signal, and was input directly into the preamplified receiver. It is necessary to move the probe laser because the optical preamplifier gain and noise figure are strongly wavelength dependent. The comparison between the error rates of the largest wavelength shifted signal and the original at that wave-

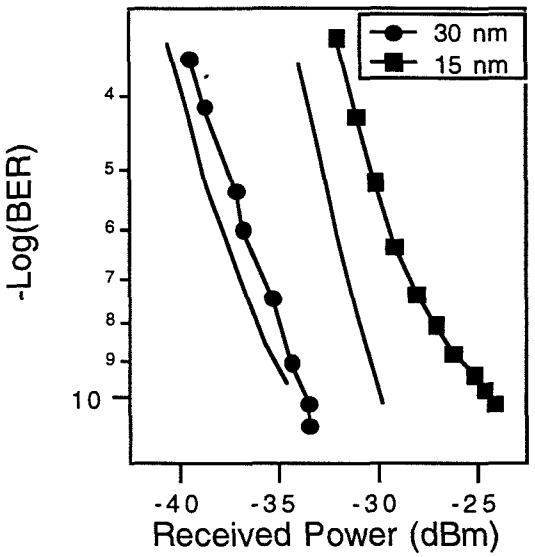

Figure 6.5: Comparison between the error rates of the original signal (shifted to the new wavelength) and the FWM converted signal (the largest shifts are shown).

length is shown in Fig. 6.5. As can be seen from the figure, the penalty introduced is about 1 dB for the down-converted signals and about 5 dB for the up-converted signal, which results primarily from the noise added to the signal in the conversion process. The receiver sensitivity (defined as the amount of power necessary to reach an error rate of 10^{-9}) is -35 dBm for the largest down-conversion. This translates to an average of 244 photons per bit ($\bar{n} = \bar{P}_s/h\nu_s B$ where $\bar{P}_s$ is the received power and B is the bitrate of the signal), only a factor of 6 higher than the theoretical minimum for an ideal optically preamplified receiver (which assumes a fully inverted EDFA, unity quantum efficiency of the photodetector, optimal bandwidth of the bandpass filter, and no insertion losses). Accounting for the insertion losses of the bandpass filter (3dB), this brings the results for this system quite close to the ideal case. It

was worth the sleepless nights, despite the fact that our record wavelength conversion remained a record for only a few months [7].

6.3 Polarization independent conversion

We have thus seem that FWM is very effective in translating the wavelengths of signals carrying digital information at high bitrates. In order for this technique to be of practical use however the process needs to be polarization independent, since after propagating through many miles of fiber, the state of polarization of a signal is neither known nor constant in time. The simplest solution to this problem is to find a polarization state for the pump for which the conversion efficiency does not depend on the polarization of the input wave. This scheme has been proposed, but has some serious limitations because it requires a specific device parameters for any given wavelength shift. We have seen in chapter 3 that, in general, there is no single state of polarization for which the conversion efficiency is polarization independent. To circumvent this problem, different schemes have been proposed. Probably the most elegant solution is to use a DFB laser in a Sagnac interferometer configuration with a polarizing beamsplitter [8]. The forward propagating laser light converts one state of polarization, and the backward propagating light converts the other sate of polarization (rotated by a half-wave plate in one of the arms of the interferometer). Other proposed schemes involve the use of two orthogonally polarized pump lasers [10] (in isotropic media) or a single pump laser with two SOAs [9].

Strained quantum well amplifiers have anisotropic active regions, and the FWM

efficiency depends on the absolute and the relative polarizations of the pump and the probe. In general, the conversion efficiency from two orthogonal pumps will still depend on the probe polarization, and to achieve independence, the exact polarizations have to be calculated using conversion efficiency matrices given in Chapter 3. For the carrier density modulation and carrier heating FWM contributions considered in this section, the single-pump converted signal can be expressed as a function of the pump and the probe via a 2x2 matrix. In the dual-pump configuration, the converted signal of interest can be described in terms of two such matrices, one corresponding to the conversion efficiency at the detuning between the signal and the first pump, and other for the detuning with the second pump. Thus, in general, to compute the polarization state of the two pumps for which the conversion efficiency is exactly independent of the probe polarization, eight conversion parameters must be known for each wavelength configuration.

We will now present an approach using alternating-strain quantum well SOAs [11], for which there is a simple pump configuration yielding nearly-polarization independent wavelength conversion. No material parameters need to be determined, and the method can be applied for almost any wavelength shift, anywhere within the gain spectrum of the amplifier. The feasibility of this scheme is demonstrated in a wavelength conversion system, at 2.5 Gb/s.

Let's begin by briefly recalling the polarization selection rules derived in Chapter 3. We found that two "types" of dynamic gratings are formed, one through beating of the TE components of the input waves, the other through beating of their TM

components. The TE (TM) component of the converted signals is generated by scattering of the TE (TM) components of the pumps off *both* types of gratings. The polarization dependence of the FWM efficiency results from the interference between these two contributions. The FWM process of interest in the dual pump configuration is one in which the two gratings are formed with different pump waves, and cannot interfere with each other. The amplitude of the wavelength converted signal at the output of the amplifier is given by

$$E_i^s(L) = \sum_{k=1}^{2} E_i^A M_{ik}^{AB} E_k^B (E_k^q)^* + E_i^B M_{ik}^{BA} E_k^A (E_k^q)^* \tag{6.1}$$

where $\vec{E}^A$, $\vec{E}^B$ and $\vec{E}^q$ are the complex field amplitudes of the pumps and the signal at the input of the SOA, and the subscripts $i, j = 1, 2$ refer to their components along TE, TM direction. M_{ik}^{AB} is the short-hand notation for a 4^{th} rank tensor M_{ijkl} described in Chapter 3 and subject to the polarization selection rules. The superscript AB means that the pump A is scattered into the converted signal and the gratings are generated with pump B. These tensor elements are the product of the FWM susceptibility tensor times a factor to account for the propagation of the waves through the waveguide.

Given M^{AB} and M^{BA}, one can use Eq. 6.1 to compute the polarization states for the two pumps for which the conversion is independent of the probe polarization. The simpler approach considered here consists of reducing the contributions to each signal component to one (since the polarization dependence stems from the interference between the terms contributing to each component of the signal). This

is done by setting one pump along TE and the other along TM. Nearly polarization-independent wavelength conversion is then obtained because of two properties of the M matrices. One is that in the limit where the detuning between the pumps is much smaller than that between the pumps and the probe $M^{AB} \sim M^{BA}$. In that limit, the detuning between the input signal and the two pumps is almost the same, thus the gratings are generated with the almost the same efficiency. The second property is that the alternating-strain devices used in our experiment have nearly equal off-diagonal components $M_{12} \sim M_{21}$ (a result of carefully engineered bandgap structures with low gain anisotropy [11]). The schematics of the polarizations and the resulting modulations are shown in Fig. 6.6. Practically, the choice of the detuning between the two pumps is important. Very small detunings require narrow bandpass filters to separate the polarization independent FWM signal from the adjacent single pump FWM signals which are strongly polarization dependent [1]. On the other hand wider detunings, on the order of the detuning with the probe, will no longer yield a polarization independent signal.

The experimental setup used to verify this polarization independent conversion scheme was similar to the one shown in Fig. 6.1. An external cavity laser and an Er-doped fiber ring laser were used as pumps. Their spacing was 0.2 nm. After pre-amplification, they were combined with the signal from a directly modulated DFB laser (Ortel Digital laser module). The three lasers were amplified to a total power of about +15 dBm and coupled into the SOA. The polarization states were adjusted by

[1] Ultimately, of course, the minimal detuning will be set by the data bandwidth, since below that the beatnote between the pumps will interfere with the data in the converted signal.

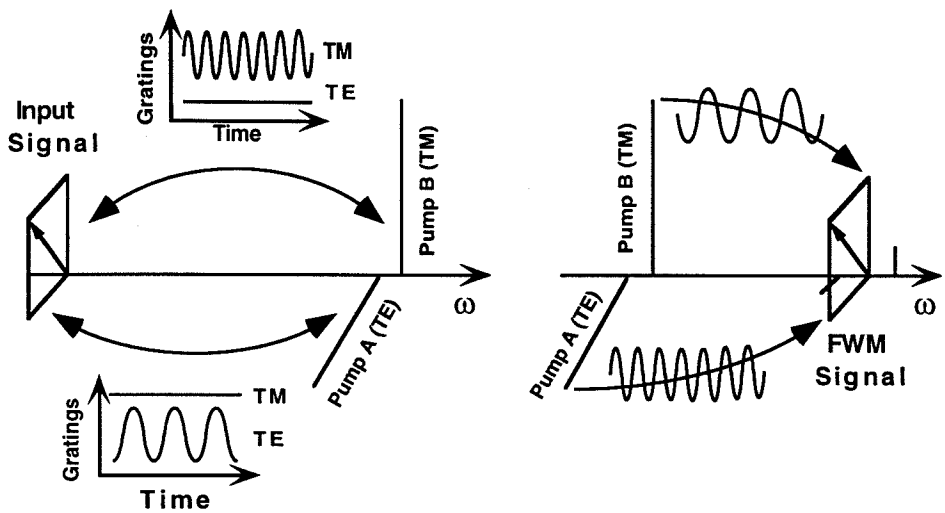

Figure 6.6: Polarization states of the waves for the polarization independent conversion. In the left diagram, the grating formation is shown; the beating of pump A and the TE component of the input signal generate a 'slower' grating. Since pump A has no TM component, there is no probe polarization dependent interference effect in the generation of these gratings. Similarly, the TM component of the probe and pump B generate 'faster' grating with no interference effects from TE waves. Then, in the right diagram, pump A scatters off the 'faster' gratings into the TE component of the signal, and pump B scatters off the 'slower' gratings into the TM component of the signal. Also shown are the single pump, polarization *dependent* FWM signals on either side of the polarization independent signal. These come from the scattering of pump A off the 'faster' gratings (left signal) and from the scattering of pump A off the 'slower' gratings.

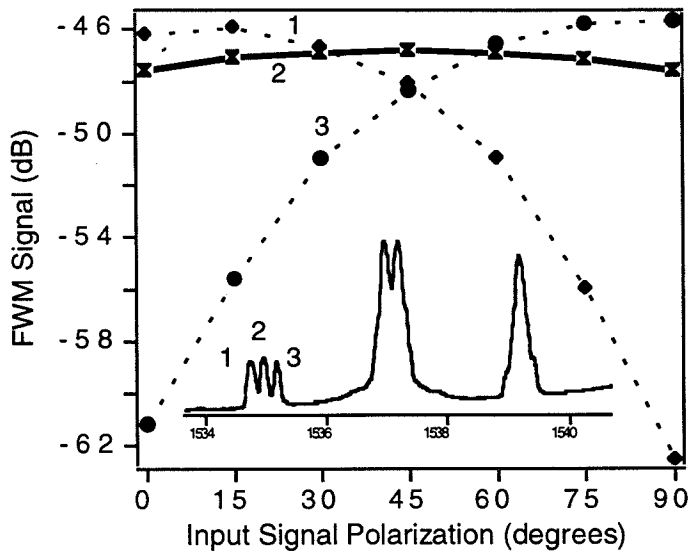

Figure 6.7: FWM signals for various linear input signal polarizations: the solid line is the dual-pump signal while the two dashed lines are the adjacent single pump FWM products. The inset shows the spectrum at the output of the SOA with the signal polarization at 45 degrees. 2 dB on the vertical scale correspond to 20 dB on the inset. Angles are measured relative to the quantum well growth axis.

inserting a polarizer at the input of the amplifier and then monitoring the power on a spectrum analyzer placed after the SOA. To detect the modulated signal, we used two bandpass filters to single out the polarization independent signal, one before and one after the optical preamplifier. The inset to Fig. 6.7 shows the spectrum at the output of the SOA for a wavelength shift of 6 nm with the probe linearly polarized at 45° relative to the growth axis. The data plotted in Fig. 6.3 give the polarization dependence of the three distinct products (i.e. 1, 2, 3) that result from FWM. The variation of the central FWM peak (labeled 2 in the figure) is less than 1.5

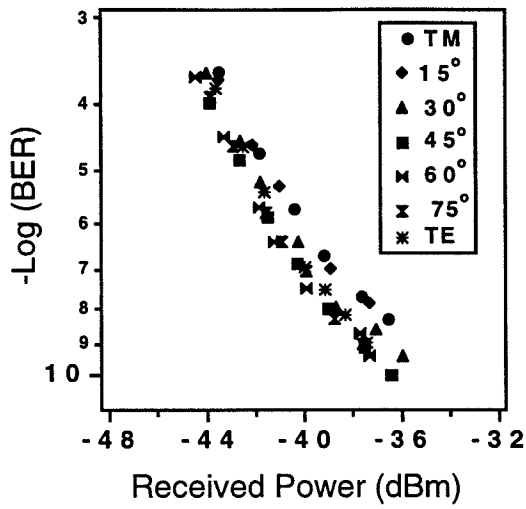

Figure 6.8: BER vs. received power for 6 nm wavelength shift at 2.5 Gb/s, for a $2^7 - 1$ pseudo-random data stream. The received power was measured on the OSA with a 0.5 nm detection bandwidth.

dB for all possible linear polarizations of the input signal. This remains the case for random elliptical polarizations of the input signal as well. The residual polarization dependence is consistent with the relative values of M_{12} and M_{21} measured the same device in Chapter 3. Fig. 6.8 shows the BER vs. received power for the same set of input signal polarizations. The best results are obtained for a signal at 45 degrees, but the penalty to the worst case (TE here) is less than 1.7 dB. The exact location of the bandpass filters is important; if they are not exactly on the center peak (peak 2), some of the polarization dependent single pump FWM will be detected. We found that this can be used to compensate for the slight asymmetry in the M tensor, and by optimum filter placement the penalty could be further reduced to 1.3 dB. We

Pump A	Pump B	Max/Min FWM signal
+45	-45	2.8 dB
+60	-30	3.5 dB
σ_+	σ_-	2.9 dB
TE	TM	1.5 dB

Table 6.1: Polarization sensitivity of the converted signal for various sets of orthogonal pump polarizations.

repeated the experiment at different detunings, and even for the lowest signal shift (4nm), there was no measurable increase of the polarization dependence with 0.2 nm pump detuning.

To compare our results with the case of isotropic conversion media (i.e. bulk active layers), we also checked the absolute polarization dependence of the mixing for various sets of orthogonal pump polarizations. The results are shown in table 1. We noticed that for the alternating-strain device tested, changes in the absolute polarization of the two pumps does not affect the polarization dependence of the efficiency too much. This is a result of the weak anisotropy of these devices, and is not to be expected for, say, a highly-tensile strained quantum well amplifier.

In conclusion, we have given a general expression for the polarization dependence of the FWM efficiency in the dual-pump configuration. In view of the complications involved in the generation of a strictly polarization independent FWM signal, we propose a simplified configuration which yields a nearly polarization independent

conversion efficiency. We have experimentally confirmed the viability of this scheme, by measuring a BER penalty of less than 1.7 dB at transmission rates of 2.5 Gb/s.

Bibliography

[1] D. Geraghty, R. Lee, M. Verdiell, M. Ziari, A. Mathur, K. Vahala, *IEEE J. of Selected Topics in Quantum Electronics*, **5**, No 5, pp. 1146, 1997

[2] J. Zhou, K. Vahala, *CLEO Proceedings*, Paper CThT1, Baltimore, 1995

[3] M. A. Summerfield, and R. S. Tucker, *IEEE Photon. Technol. Lett.*, **8**, p. 1316, 1996.

[4] A. D'Ottavi, F. Girardin, L. Graziani, F. Martelli, S. Scotti, R. Dall'Ara, J. Eckner, G. Guekos, *IEEE J. of Selected Topics in Quantum Electronics*, **3**, No. 2, pp. 522, 1997

[5] C. Holtmann, P. Besse, T. Brenner, H. Melchior, *IEEE Photon. Technol. Lett.*, **8**, pp. 343, 1996

[6] R.B. Lee, Ph. D. Thesis, Caltech, 1997

[7] A. Kelly, D. Marcenac, D. Nesset, *Electronics Letters*, **33**, No. 25, pp. 2123, 1997

[8] S. Watanabe, H. Kuwasstuka, S. Takeda, H. Ishikawa, *Electronics Letters*, **33**, pp. 316, 1997

[9] J. Lacey, S. Madden, M. Summerfield, *IEEE Photon. Technol. Lett.*, **9**, pp. 1355, 1997

[10] R.M. Jopson and R.E. Tench, *Electronics Letters*, **33**, pp. 2216, 1993

[11] M. A. Newkirk, B. I. Miller, U. Koren, M. G. Young, M. Chen, R. M. Jopson, and C. A. Burrus, *IEEE Photon. Technol. Lett.*, **5**, pp. 406, 1993

[12] R. Paiella, G. Hunziker, U. Koren, K. Vahala, *IEEE J.of Selected Topics in Quantum Electronics* **3**, 529, 1997

Chapter 7

Lasing FWM wavelength converters

7.1 Introduction

In the previous chapter, we demonstrated how long and strongly saturated SOAs can be very effective wide span wavelength converters. An alternative design strategy is to place the active medium into an optical cavity. In this chapter, we describe and demonstrate two different FWM configurations that take advantage of the optical feedback in a semiconductor laser. In the first case, the laser is biased above threshold and the lasing beam is used as the FWM pump wave, so that a large pump power is obtained with significantly reduced device complexity (i.e. with no need for an external pump source and for an EDFA at the SOA input). Furthermore, the lasing action is beneficial to the wavelength conversion process because of the resulting clamping of the optical gain (and hence of the FWM nonlinearity). In a second

configuration, we use an external pump wave (strong enough to quench any solitary laser oscillation) and tune the frequency of the converted signal to the laser frequency; consequently, the device is injection locked by the FWM signal itself, leading to a large resonance enhancement of both conversion efficiency and optical signal-to-noise ratio (OSNR).

Both approaches would be difficult to implement with a Fabry-Perot cavity, because of the complications arising from the laser being injection locked by the external input wave(s). In order to avoid such complications, it is convenient to use a resonator with a narrowband wavelength-selective reflector, such as a Bragg mirror, with the external input wave(s) sufficiently detuned from its reflection band so that for such wave(s) the device simply acts as a SOA. In this paper, we present experimental results obtained from a semiconductor laser with a fiber Bragg grating (FBG) pigtailed to one facet, and a high-reflection coating on the other facet. This structure has the advantage that there is no spatial overlap between the nonlinear medium and the Bragg mirror, which may introduce a significant phase mismatch in the FWM interaction. It should be mentioned however that self-pumped FWM has also been recently demontrated with good results in long, quarter-wave shifted distributed feedback (DFB) lasers [1]. In both cases, the center wavelength of the Bragg mirror reflection bandwidth is not tunable, so that the pump wavelength (in the self-pumped configuration) and the destination wavelength of the converted signal (in the injection-locked configuration) are fixed. However, an electrically-tunable, on-chip external distributed Bragg reflector (DBR) could be used to overcome this

problem (DBR lasers are also promising for additional reasons, as will be discussed in the following)

This Chapter is organized as follows. We begin, in the next Section, with a description of the FBG coupled laser used in this work, and of the general features of the FWM interaction in this device. In Section 7.3 we discuss wavelength conversion by self-pumped FWM, and present the measured bit-error-rate (BER) performance of this converter at 2.5 Gbit/sec. An important feature of this configuration is the fact that, due to gain clamping, both the conversion efficiency and the OSNR of the converted signal exhibit a strong, nearly quadratic, dependence on the pump power; this property is experimentally verified in Section 7.3, where we also discuss its implications to the design of self-pumped FWM converters. Finally, Section 7.4 is devoted to a wavelength converter based on injection-locked FWM; in particular, we present a detailed characterization of its static response, together with preliminary dynamic results at 1 Gbit/sec. With the present device, this approach cannot be extended to signals with a higher bit rate due to the narrow linewidth of the injection-locking resonances; however, we discuss theoretically how the maximum bit rate can be improved by proper design of the laser cavity.

7.2 FWM in a fiber Bragg grating coupled semiconductor laser

A schematic picture of the device used in these experiments is given in Fig. 7.1. The FBG, having a narrow reflexion bandwidth centered at about 1554 nm, is butt-coupled

to the front facet (which is anti-reflexion coated); on the other facet, a high-reflexion coating provides almost unit reflectivity. The lasing action occurs in a temperature controlled, 500-μm-long, compressively strained multiquantum-well active region. We point out that the present device characteristics were optimized for single-mode laser oscillation. Also shown in the figures is an optical circulator, used for efficient coupling of light in and out of the laser (although in the self-pumped FWM experiment a bidirectional coupler was used instead). The generation and propagation of the FWM signal in this device can be described in the same way as for the case of single-pass SOAs, except that here one has to consider waves traveling in both direction along the waveguide axis (and the boundary conditions are different). In the following, we will briefly outline the theoretical description of FWM in a FBG coupled laser, irrespective of the specific configuration considered (i.e. of whether the pump wave is generated inside the laser or is externally injected). This description will then be used in the following Sections to discuss how the wavelength conversion performance of this device can be improved by proper design of the laser structure.

In the presence of a pump wave of frequency ω_p and an input signal of (carrier) frequency $\omega_q = \omega_p - \Omega$, two sidebands are generated through the FWM nonlinear interaction, at frequencies $\omega_s = \omega_p + \Omega$ and $\omega_{s'} = \omega_q - \Omega$. If we assume that the pump wave is significantly stronger than the input signal (as is typically the case in practical wavelength conversion experiments), the latter FWM sideband can be ignored, and the total electric field in the laser waveguide (averaged over the transverse dimensions) can be written as

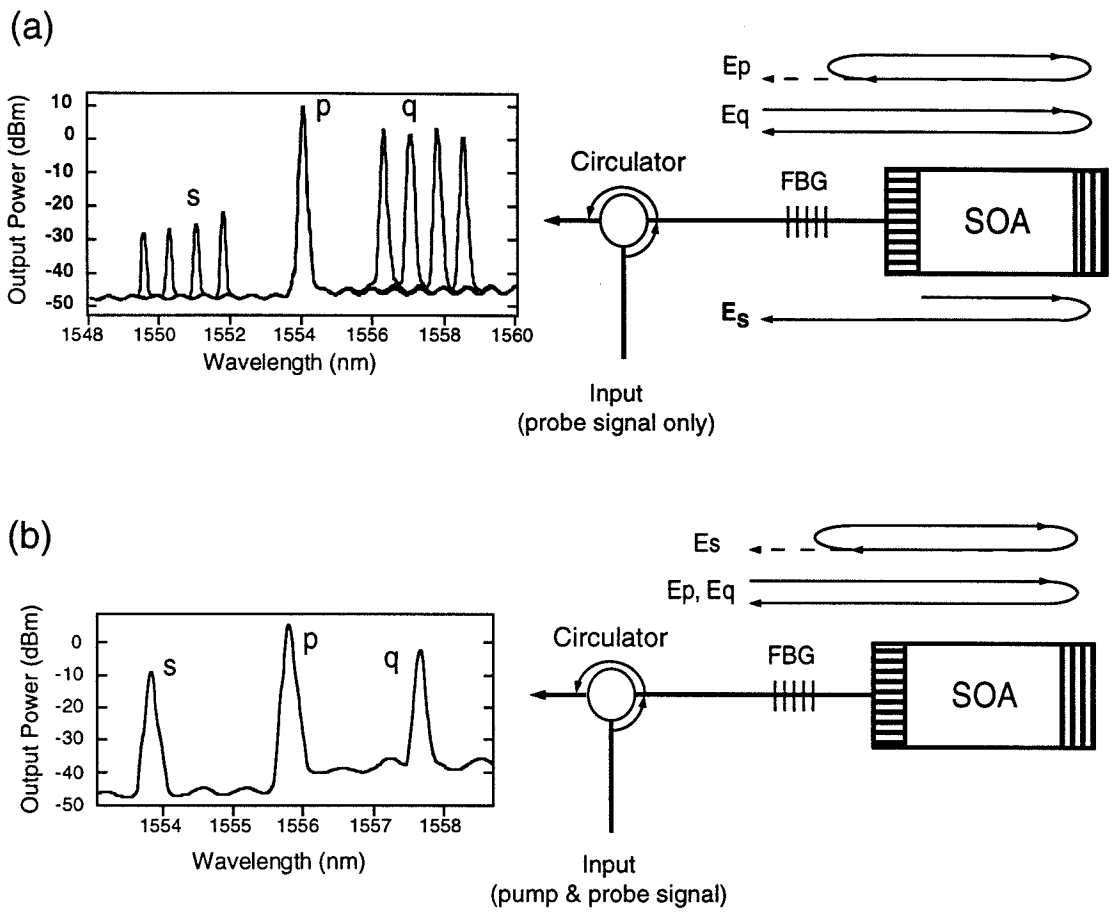

Figure 7.1: (a) Schematic representation of the wavelength conversion device based on self-pumped FWM in a FBG coupled semiconductor laser. The left panel shows four superimposed optical spectra measured at the output of the converter, for wavelength downshifts of 4.5, 6, 7.5 and 9 nm (0.1 nm resolution bandwidth). (b) Schematic representation of the wavelength conversion device based on injection-locked FWM in a FBG coupled semiconductor laser. The left panel shows the optical spectrum measured at the output of the converter under resonance conditions, for a wavelength downshift of 4 nm (0.1 nm resolution bandwidth, less than 4 dBm total in-fiber input power).

$$\mathcal{E}(z,t) = \sum_{f=p,q,s} \left(E_f^+(z) e^{ik_f z} + E_f^-(z) e^{-ik_f z} \right) e^{-i\omega_f t} + c.c. \tag{7.1}$$

where $k_f = \omega_f \bar{n}/c$ and $\bar{n}$ is the modal index of refraction.

The different field amplitudes $E_f^{\pm}$ defined above satisfy the following coupled-mode wave equations [2, 5]

$$\pm \frac{dE_{p,q}^{\pm}(z)}{dz} = \left\{ \Gamma \left(\frac{1}{2}\, g(P_{tot}(z)) - i\, \delta k(P_{tot}(z)) \right) - \frac{1}{2}\gamma \right\} E_{p,q}^{\pm}(z), \tag{7.2}$$

$$\begin{aligned} \pm \frac{dE_s^{\pm}(z)}{dz} = & \left\{ \Gamma \left(\frac{1}{2}\, g(P_{tot}(z)) - i\, \delta k(P_{tot}(z)) \right) - \frac{1}{2}\gamma \right\} E_s^{\pm}(z) + \\ & + \Gamma \kappa(P_{tot}(z);\Omega) \left(E_p^{\pm}(z) \right)^2 \left(E_q^{\pm}(z) \right)^* \end{aligned} \tag{7.3}$$

where Γ is the confinement factor, g is the material gain coefficient, $-\delta k$ is the carrier-induced phase shift per unit length, γ is the waveguide scattering loss coefficient, κ is the FWM coupling coefficient, and P_{tot} is the total optical power along the axis of the active region. Notice that we are neglecting in Eq. (7.3) any contribution to the FWM signal arising from mixing of counterpropagating field components, because these contributions are strongly phase-mismatched. The contributions from copropagating waves are taken to be perfectly phase matched, and we neglect the wavelength dependence of g and δk. These assumptions are perfectly justified over a wide range of wavelength shifts of interest (say $|\Delta\lambda| \equiv |\lambda_q - \lambda_s| \sim 2 - 30$ nm).

Equations (7.2) and (7.3) are solved in conjunction with a set of boundary conditions having the general form (for $f : p, q, s$)

$$E_f^+(0) = C\sqrt{R_{BG}(\omega_f)}e^{i\omega_f l_{BG}(\omega_f)/c}E_f^-(0) \; + \; \sqrt{C}E_f^{in},$$

$$E_f^-(L) = \sqrt{R_{HC}}E_f^+(L) \tag{7.4}$$

where $z = 0$ and $z = L$ denote the anti- and the high-reflection coated facets of the laser respectively, C is the fraction of optical power that is coupled from the fiber into the laser (and viceversa), R_{BG} and R_{HC} are the power reflectivities of the FBG mirror and of the high-reflection coating respectively (the former being a narrowband function of frequency peaked at around 1554 nm), l_{BG} is the optical path length from the anti-reflection coated facet into the FBG and back to the same facet, and E_f^{in} is the external field at ω_f launched into the FBG.

The solution of the boundary-value problem above requires knowledge of the dependence of the coefficients appearing in Eqs. (7.2) and (7.3) on the total power $P_{tot}(z)$. As for the gain coefficient g, it is convenient to write it as

$$g(P_{tot}) = \frac{g_{th}}{\Gamma} + A\ \Delta N(P_{tot}) \tag{7.5}$$

where

$$g_{th} = \gamma + \frac{1}{L}\log(\frac{1}{C\sqrt{R_{BG}R_{HC}}}) \tag{7.6}$$

is the modal gain coefficient at threshold (equal to the distributed loss coefficient), A is the differential gain, and R_{BG} is evaluated at the lasing frequency at threshold. Furthermore, ΔN is the local deviation of the steady-state carrier density from its threshold value, given by (from solution of the carrier density rate equation in steady-state)

$$\Delta N(P_{tot}) = \frac{(I - I_{th}) / (qV_a) - g_{th} P_{tot} / (\Gamma \hbar \omega S_m)}{1/\tau_{sp} + A P_{tot} / (\hbar \omega S_m)} \tag{7.7}$$

where I is the laser bias current, V_a is the volume of the active region, S_m is the modal cross-sectional area, and τ_{sp} is the spontaneous and nonradiative recombination lifetime. A similar functional dependence on P_{tot} can be assumed for δk (which cancels out in the results of the following Sections).

Finally, the nonlinear coupling constant κ depends on the optical power through the gain coefficient, its derivatives with respect to carrier density and temperature, and the corresponding linewidth enhancement factors. An expression for $\kappa(P_{tot}; \Omega)$ can be derived from a full microscopic theory of FWM in semiconductor gain media [4], and it has been modeled with varying degrees of approximation [2, 5]. A simple model that is often used and that is a valid approximation over a wide range of conditions is based on the expression

$$\kappa(P_{tot}; \Omega) = \kappa_0(\Omega) g(P_{tot}) \tag{7.8}$$

where the function $\kappa_0(\Omega)$ describes the decrease in the strength of the FWM nonlinearity with increasing detuning frequency.

To conclude this discussion, we point out that, since the pump wave is commonly much stronger than the input and the converted signals, it is a valid assumption to take

$$P_{tot}(z) \approx \left|E_p^+(z)\right|^2 + \left|E_p^-(z)\right|^2. \tag{7.9}$$

Then, $P_{tot}(z)$ can be obtained from a simple numerical integration of the boundary-value problem for the pump wave alone. An important simplification that follows from this assumption is that the carrier density is saturated by the (cw) pump wave alone. And as a result, even in the presence of an intensity-modulated input signal, the coefficients g, δk, and κ of Eqs. (7.2)-(7.3) remain approximately constant in time. The results obtained from this analysis, which is inherently steady-state, can then be taken to be approximately valid even in the presence of such a modulated signal (i.e., under the practical conditions of a wavelength conversion experiment).

7.3 Wavelength conversion by folded-path, self-pumped FWM

7.3.1 Wavelength conversion performance

In this Section, we will discuss wavelength conversion by self-pumped FWM in a FBG coupled diode laser. As illustrated schematically in Fig. 7.1, in this configuration the laser is biased above threshold, and the FWM pump wave is provided by the lasing beam, so that this wavelength converter does not require a high-power external pump source. On the other hand, the input signal and, consequently, the converted signal have frequencies well outside of the reflection band of the FBG, so that for these waves the device simply acts as a gain-clamped SOA. Notice that the reflection off the back mirror (folded-path SOA) effectively doubles the FWM interaction length, leading to improved conversion efficiency (however, as will be discussed below, the OSNR of the FWM signal is not correspondingly enhanced). Also shown Fig. 7.1 (left panel) are four superimposed optical spectra measured at the output of the device,

corresponding to wavelength (down) shifts of 4.5, 6, 7.5, and 9 nm.

The experimental setup used to study the wavelength conversion performance of this device, and the results of the measurement, are described in details in Ref. [15]. The input signal was provided by a tunable external-cavity semiconductor laser, externally modulated at 2.5 Gbit/sec with a $2^7 - 1$ pseudorandom bit stream (no significant pattern length dependence was observed). Before being coupled into the converter (through a bidirectional coupler in this case), the input signal was amplified in an EDFA, filtered in a 1-nm bandpass filter to reduce the ASE noise from the EDFA, and then passed through a variable attenuator (used to measure the input-signal power dynamic range of the converter). The converted signal collected from the device output (through the other input arm of the bidirectional coupler) was similarly attenuated by a variable amount and then fed to a preamplified receiver. BER measurements were then performed with the same setup as we described in the previous chapter.

In Fig. 7.2 we show the measured BER versus received power for the wavelength shifts of Fig. 7.1(a) (the eye-diagram in the inset corresponds to the 4.5 nm shift). No significant degradation is observed except at the largest measured shift (9 nm), where the decrease in the OSNR of the converted signal with increasing $\Delta\lambda$ begins to play a role. Furthermore, we found that error rates lower than 10^{-9} could be obtained over a wide input-signal power range, approximately -10 to +2 dBm (coupled into the FBG) for the 4.5 nm shift. Incidentally, we notice that the degradation in BER performance at large input-signal powers is due not to a reduction in the optical gain

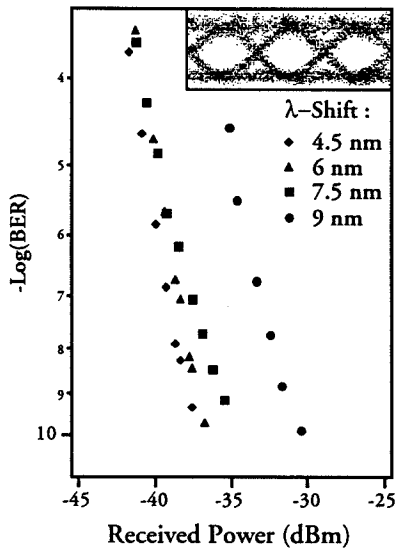

Figure 7.2: BER performance at 2.5 Gbit/sec of the wavelength conversion device based on self-pumped FWM. The inset shows the error-free eye diagramm for the 4.5 nm conversion.

as in the case of standard SOAs (since the gain here is clamped by the lasing action), but rather by a reduction in pump power.

These results clearly indicate that the FWM configuration described in Fig. 7.1(a) is an attractive approach to wavelength conversion. Good conversion performance is obtained at 2.5 Gbit/sec, with significantly reduced device complexity (relative to the case of FWM wavelength converters based on single-pass SOAs) and low input-signal power requirements. While conversion with much larger wavelength shifts and bit rates has been recently demonstrated using specially optimized single-pass SOAs [9, 10], it should be again emphasized that the present device was not designed specifically for this application. It is therefore worthwhile to investigate theoretically its margins of improvement as a wavelength converter. To this purpose, we solved the coupled-mode equations of FWM in a FBG coupled laser, Eqs. (7.2)-(7.3) above,

for $P_s^{out} = C|E_s^-(0)|^2$, subject to the boundary conditions depicted schematically in Fig. 7.1(a) (i.e. the boundary conditions of Eq. (7.4) with $E_p^{in} = E_s^{in} = 0$, and $R_{BG}(\omega_q) = R_{BG}(\omega_s) = 0$). The FWM conversion efficency (the ratio of the in-fiber converted signal output power to the input-signal power coupled into the FBG) was found to be given by

$$\eta \equiv \frac{P_s^{out}}{P_q^{in}} = \left(\frac{P_p^{out}}{1 - R_{BG}(\omega_p)}\right)^2 \left| \int_0^L dz\ \Gamma\kappa(P_{tot}(z);\Omega) \left[\frac{G(z)}{\sqrt{R_{HC}}G(L)} + \frac{\sqrt{R_{HC}}G(L)}{G(z)}\right]\right|^2. \tag{7.10}$$

In this expression, the two terms in the square brackets refer to the FWM signals generated by the forward and by the backward traveling waves respectively. Furthermore, we defined the overall gain over a length z of the laser active region,

$$G(z) = \exp \int_0^z \mathrm{dz}' \left[\Gamma \mathrm{g}(\mathrm{P_{tot}(z')}) - \gamma\right] \tag{7.11}$$

with the lasing threshold condition requiring that

$$G(L) = \frac{1}{C\sqrt{R_{BG}(\omega_p)R_{HC}}} \tag{7.12}$$

Incidentally, notice that, due to the large asymmetry of the FBG coupled laser resonator, $P_{tot}(z)$ significantly varies along the cavity axis, so that even under threshold conditions one cannot take $\Gamma g(P_{tot}(z)) = g_{th}$ for all z in the active region.

As demonstrated in Chapter 6, dramatic improvements in the performance of FWM wavelength converters based on single-pass SOAs can be achieved by increasing the FWM interaction length. It is therefore interesting to consider how this approach

would work in the case of the present device, especially in light of the fact that here the physical length of the semiconductor active region is used twice in the generation of the FWM signal (as well as of the ASE noise power in its spectral vicinity). In Figs. 7.3(a) and 7.3(b), respectively, we plot the FWM conversion efficiency and the OSNR of the converted signal for a FBG coupled laser as a function of the length of the active region (OSNR here is defined as the ratio P_s^{out}/P_{ASE}^{out}, where P_s^{out} is given in Eq. (7.10), and the ASE noise power in the detector bandwidth P_{ASE}^{out} was computed as described in the last section of this chapter). The approximation of Eq. (7.8) was used for the nonlinear coupling coefficient κ, with the value of $|\kappa_0(\Omega)|$ set to reproduce the measured conversion efficiency for the 6 nm wavelength shift; all other structural and operational parameters were either known or reasonably guessed. For comparison, the same quantities are also plotted (dashed lines) for the case of FWM in a single-pass but otherwise identical SOA. The filled and empty dots are experimental data from this work [15] and from Ref. [6] respectively, for $\Delta\lambda = 6$ nm (the agreement is good). From Fig. 7.3(a) it is apparent that the FWM conversion efficiency significantly benefits from the folded-path SOA geometry. Indeed, in terms of conversion efficiency, the self-pumped converter described here roughly performs as a FWM converter based on a single-pass SOA twice as long. However, in the folded-path SOA, the physical length of the active region is used twice also in the generation and amplification of the ASE noise power, which is the main limiting factor to the converter BER performance. As shown in Fig. 7.3(b), in the case at hand this increase in P_{ASE}^{out} more than offsets the corresponding improvement in conversion efficiency. In

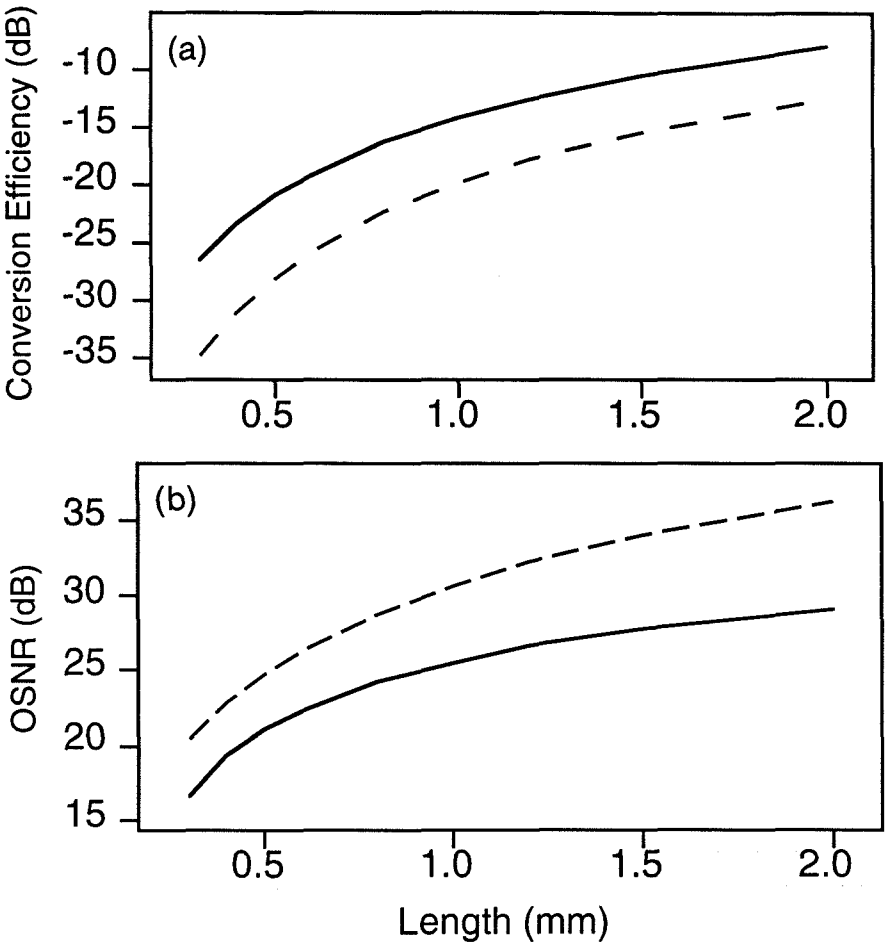

Figure 7.3: Theoretical conversion efficiency (upper panel) and OSNR (lower panel) of the self-pumped FBG coupled laser (continuous lines), and of an otherwise identical, externally pumped, single-pass SOA (dashed lines), versus length of the active medium (6 nm down-shift). The filled and empty dots are experimental data from this work and from Ref. [6], respectively.

conclusion then, these plots seem to suggest that increasing the length of the FBG coupled laser would certainly improve its wavelength conversion performance, but it would not by itself be able to put it on par with the present state-of-the-art in FWM converters [9, 10]. Instead, more dramatic improvements can be obtained by designing the laser structure for higher power operation, to take advantage of the strong (nearly quadratic) pump power dependence of the conversion efficiency and OSNR of this device, as described below.

7.3.2 Gain clamping and pump power dependence

A peculiar feature of the FWM nonlinearity of SOAs is that it depends on the optical gain coefficient, and as a result it saturates with the total optical power present in the amplifier active region. Indeed, it has been observed [7, 8] that for single-pass SOAs there exists an "optimum" value of the pump power that maximizes the FWM conversion efficiency. At significantly lower values of $P_{tot} \approx P_p$, both the conversion efficiency and the OSNR of the FWM signal increase quadratically with it. As the pump power is increased beyond the "optimum" value, the conversion efficiency actually decreases while the OSNR further increases, but at a slower (sublinear) rate. Practical wavelength converters based on FWM in single-pass SOAs operate in this high-power regime, so that the benefits associated with a large pump power are nearly fully exploited in these devices.

In the self-pumped configuration, on the other hand, the optical gain is clamped at its threshold value by the lasing action, as indicated by Eq. (7.12). As a result, both the conversion efficiency and the OSNR of the FWM signal are expected to increase

monotonically with pump power. This expectation is verified by the data shown in Figs. 7.4a and 7.4b, where we plot η and OSNR respectively versus P_p^{out} for several wavelength downshifts. The experimental setup used is the same as described above (with a cw input signal); P_p^{out} was varied by changing the bias current of the FBG coupled laser (the resulting temperature changes were compensated by constantly adjusting the device temperature controller during the measurement). From these plots, we find that as P_p^{out} is varied over a range of more than 10 dB, both η and OSNR vary as $(P_p^{out})^{\beta}$, with the exponent β ranging between 1.6 and 1.8 for the different wavelength shifts (no systematic dependence of β on $\Delta\lambda$ is observed).

In order to discuss these results, it is convenient to refer to Eq. (7.10) for the conversion efficiency η and to Eq. (7.22) of the last section for the output ASE noise power P_{ASE}^{out} ($OSNR \equiv \eta P_q^{in}/P_{ASE}^{out}$). First of all, using these equations it is easy to show that both η and OSNR will vary quadratically with P_p^{out} if $P_{tot}(z)$ is uniform along the laser axis. The reason is that in this case the gain coefficient g itself (not just the overall gain $G(L)$) is clamped (i.e., $\Gamma g(P_{tot}(z)) = g_{th}$ for all values of z), and therefore so are the FWM coupling coefficient κ and the whole integrals appearing in Eqs. (7.10) and (7.22). In an asymmetric resonator such as the FBG coupled laser, however, the lasing power strongly varies along the axis (decreasing towards the higher reflectivity mirror): depending on the details of $g(P_{tot}(z))$ and $\kappa(P_{tot}(z))$, this may lead to a weak power dependence of the integrals in these equations, and therefore explain the observed deviation from a purely quadratic dependence. In particular, a value for the exponent β slighty smaller than two (as in the data of Fig. 7.4) would

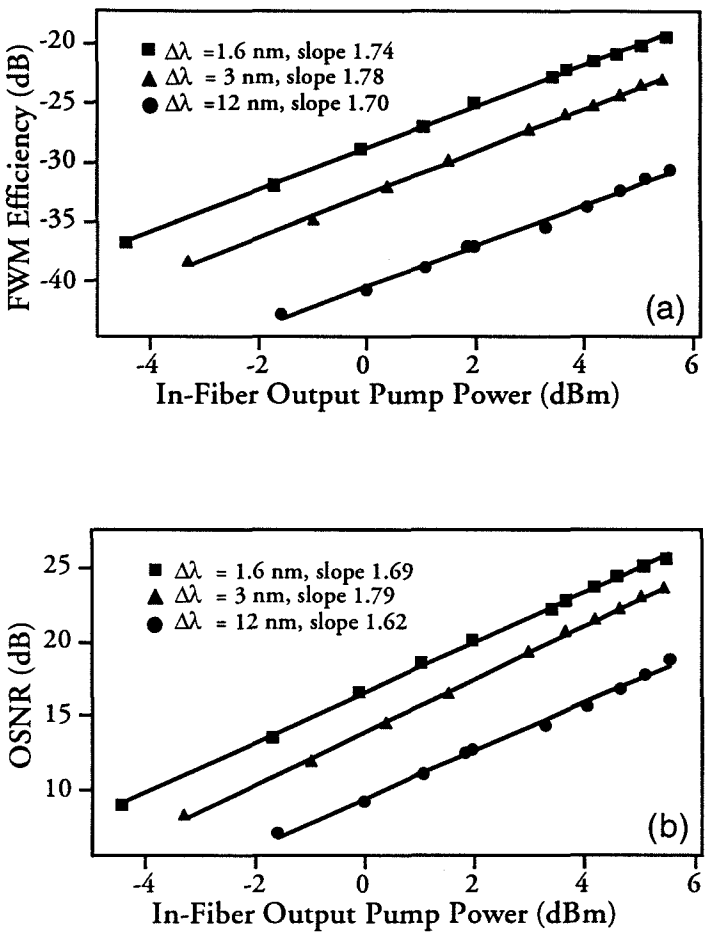

Figure 7.4: Conversion efficiency (upper panel) and OSNR (lower panel) of the self-pumped FBG coupled laser versus output pump power (measured at the output port of the circulator of Fig.1 (a)), for several wavelength downshifts $\Delta\lambda$. The continuous lines are best-fit straight lines through the data, with slopes listed in the legend.

seem to require a stronger saturation of the FWM coupling coefficient than assumed in Eq. (7.8) (i.e., a larger decrease in κ than g with increasing P_{tot}). Alternatively, the measured value of β could be attributed to causes not directly related to the FWM process in the laser active region such as a power dependence of the fiber-laser coupling coefficient C).

In any case, the important thing in the present context is the strong dependence of η and OSNR on the pump power: notice from Fig. 7.4 that neither quantity appears to saturate as P_p^{out} approaches the upper end of its considered range of values. It is therefore apparent that a large improvement in the wavelength conversion performance of this device can be obtained with a laser structure specifically designed for high-power operation. In fact, the data of Fig. 7.4 suggest that increasing the pump power may be a more effective optimization strategy for the case of self-pumped FWM than it is for FWM in single-pass SOAs. In this sense, semiconductor lasers with an on-chip DBR seem more promising in view of the extremely large output powers that can be obtained with these devices. Large wavelength shifts at 10 Gbit/sec are therefore realistic even in the self-pumped configuration, which, in conjunction with its inherent simplicity, would make it quite attractive for system applications.

7.4 Wavelength conversion by injection locked FWM

7.4.1 Wavelength conversion performance

The second wavelength conversion configuration considered in this work is illustrated schematically in Fig. 7.1(b). In this case, both the input signal and the pump wave

are externally launched into the laser active region, with frequencies well outside of the FBG reflection band. On the other hand, the FWM signal frequency $\omega_s = 2\omega_p - \omega_q$ is chosen to nearly coincide with a longitudinal mode of the laser cavity. The laser is biased below the threshold required for oscillation in the presence of the pump wave alone. When the input signal is also turned on, the resulting FWM signal acts as a strong seed for oscillation of the nearby cavity mode. The FBG coupled laser is consequently locked to oscillate at the FWM signal wavelength, and it automatically generates a replica of the input signal at this wavelength. The net result is a sharp resonance enhancement of the FWM conversion efficiency and OSNR. This mechanism is entirely equivalent to the technique of injection locking, which, in the context of semiconductor lasers, has been considered [18, 19, 20] as a means to improve their stability and noise properties, and, more recently, for signal-processing applications [21, 22]. However, it is interesting to note that in this case the "master" laser beam is not externally injected, but rather generated inside the active medium by the FWM nonlinear interaction.

The panel at the left of Fig. 7.1(b) shows a typical output spectrum of this wavelength converter under resonance conditions, for a wavelength downshift of 4 nm. The experimental setup is the same as described above, except that two external-cavity lasers are now used to provide the two input waves (with their outputs combined in a bidirectional coupler before being fed into the same EDFA), and a broadband filter is now used for ASE prefiltering at the output of the EDFA. We see from this figure that the FWM signal is strongly enhanced by the optical feedback: for instance, if we

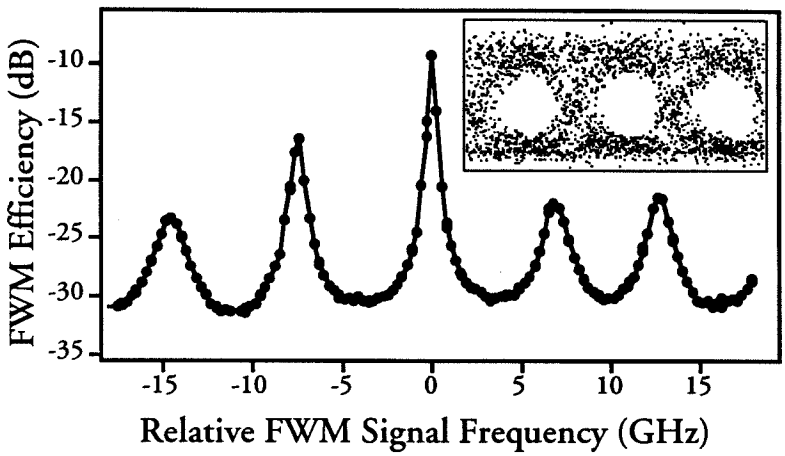

Figure 7.5: Conversion efficiency for injection-locked FWM in the FBG coupled laser versus frequency of the converted signal measured relative to the frequency of the solitary laser output (4-nm downshift, approximately 5 dBm total in-fiber input power), and (inset) eye diagram at 1 Gbit/sec.

refer to the smallest shift displayed in the left panel of Fig. 7.1(b) (a 4.5 nm downshift in the self-pumped configuration), and we keep into account the larger pump power used there, this enhancement can be quantified to be more than two orders of magnitude. In fact, given that the fiber-to-fiber gain experienced by the input signal in the injection-locked converter is approximately equal to $1/R_{BG} \approx 6$ dB, we find that the FWM conversion efficiency in Fig. 7.1(b) is close to unity. In Fig. 7.5, we plot the measured FWM conversion efficiency as a function of the frequency of the converted signal (relative to the frequency of the solitary laser output): several resonances, associated with various modes of the FBG coupled laser cavity, are clearly resolved. The spectral width of these resonances is quite small, less than 2 GHz

for all the peaks in the figure. This poses a serious limitation to the applicability of the present device to wavelength conversion of high-speed signals, because of the spectral distortion that occurs when the bit rate is comparable to, or larger than, the resonance width. In a preliminary study, we obtained conversion with best-case BER of 10^{-9} at 1 Gbit/sec, with eye-diagram shown in the inset of Fig. 7.5 (the corresponding BER versus received-power curves exhibit a strong flooring). Also, we found, consistent with the measured width of the injection-locking resonances, that the conversion performance rapidly degraded at higher bit rates.

Based on these results, it is apparent that the width of the resonances must be significantly improved in order to increase the maximum bit rate at which this wavelength converter can operate. In the following we will discuss how to specifically design the laser structure to this purpose, again using the theoretical framework developed in Section 7.2. From solution of Eqs. (7.2) and (7.3) with the boundary conditions depicted schematically in Fig. 7.1(b), the FWM conversion efficiency can be written as

$$\eta = f(\omega_s) \times \eta|_{R_{BG}\to 0} \tag{7.13}$$

where we defined

$$f(\omega_s) = \frac{1 - R_{BG}(\omega_s)}{\left|1 - C\sqrt{R_{HC}R_{BG}(\omega_s)}G(L)e^{i\Delta\Phi(\omega_s)}\right|^2} \tag{7.14}$$

The quantity $\eta|_{R_{BG}\to 0}$ is the conversion efficiency of the same device used in the

injection-locked FWM configuration, with the same power distribution $P_{tot}(z)$, but without the FBG (i.e., operated as an externally pumped, folded-path SOA). Analytically, it is given by the same expression for the FWM efficiency in the self-pumped configuration, Eq. (7.10) (with $R_{BG}(\omega_p) = 0$ in this case); numerically, however, these two quantities may be quite different, because of the different power distributions, and hence overall gain, in the two configurations.

The function $f(\omega_s)$ defined in Eq. (7.14) provides a measure of the performance enhancement associated with the optical feedback. In this equation, $G(z)$ is the overall gain of Eq. (7.11); notice that due to the large emission into "lasing mode" (by the FWM interaction) $G(L)$ can significantly differ from its threshold value, and Eq. (7.12) should be replaced by

$$G(L) = \frac{e^{\Gamma A \Delta\bar{N} L}}{C\sqrt{R_{BG}(\omega_s)R_{HC}}}$$
$$\Delta\bar{N} \equiv \int_0^L \frac{dz}{L}\, \Delta N(P_{tot}(z)). \tag{7.15}$$

with $\Delta\bar{N} < 0$ in this configuration. Furthermore, the quantity $\Delta\Phi$ introduced in Eq. (7.14) is the round-trip phase shift in the laser cavity, given by

$$\Delta\Phi(\omega_s) = \frac{l_{BG}(\omega_s) + 2\bar{n}L}{c}\omega_s - 2\int_0^L dz\ \Gamma\delta k(P_{tot}(z)) =$$
$$= 2m\pi + \frac{l_{BG}(\omega_s) + 2\bar{n}L}{c}(\omega_s - \omega_m) \tag{7.16}$$

where m is an integer, and ω_m is the frequency of the mth longitudinal mode of the solitary laser in the presence of the power distribution $P_{tot}(z)$ (the second equality in Eq. (7.16) assumes that ω_s is sufficiently close to ω_m that $l_{BG}(\omega_s) \approx l_{BG}(\omega_m)$). It

is interesting to note that, in the case of standard laser operation, Eq. (7.14) gives the ratio of the output power of the laser to the spontaneous emission power emitted into the lasing mode; near threshold this factor is very large, which explains, in the present case, the strong enhancement in the FWM signal power.

Using Eqs. (7.15) and (7.16) in (7.14), the enhancement function $f(\omega_s)$ can be rewritten as follows

$$f(\omega_s) = \frac{1 - R_{BG}(\omega_m)}{\left(1 - e^{\Gamma A \Delta \bar{N} L}\right)^2 + 4e^{\Gamma A \Delta \bar{N} L} \sin^2(\pi \frac{\omega_s - \omega_m}{\Delta \omega_m})} \tag{7.17}$$

where again we took $\omega_s \approx \omega_m$, and we defined the cold-cavity free spectral range near ω_m

$$\Delta\omega_m \equiv \frac{c}{l_{BG}(\omega_m) + 2\bar{n}L}. \tag{7.18}$$

Equation (7.17) has the general form of a Fabry-Perot transmission function, with the mth peak centered at the mode frequency ω_m and having FWHM $\delta\omega_L^m$ and maximum value E_{max}^m given by

$$\begin{aligned} \delta\omega_L^m &\approx \frac{\Delta\omega_m}{\pi} \frac{1 - e^{\Gamma A \Delta \bar{N}_m L}}{e^{\Gamma A \Delta \bar{N}_m L/2}}, \\ E_{max}^m &\approx \frac{1 - R_{BG}(\omega_m)}{\left(1 - e^{\Gamma A \Delta \bar{N}_m L}\right)^2}. \end{aligned} \tag{7.19}$$

(notice that ΔN depends on ω_m through $R_{BG}(\omega)$, see Eqs. (7.7) and (7.6), hence the subscript m). As mentioned before, the spectral width $\delta\omega_L^m$ sets the maximum bit rate at which the wavelength converter described here can operate. The laser

structure to be used in this converter should therefore be designed so as to maximize this quantity.

From inspection of Eq. (7.19), we find that the largest improvements in the performance of this converter can be obtained by maximizing the free spectral range $\Delta\omega_m$, since the width of the locking resonances increases linearly with it, while the conversion efficiency is not affected (at least insofar as the length L of the mixing medium is not reduced). In practice, this can be accomplished by shortening the optical path length in the Bragg mirror, which, in the present device, accounts for the larger part of the measured 7 GHz free spectral range. The bandwidth $\delta\omega_L^m$ also increases with increasing $\Gamma A\Delta\bar{N}_m L$; the FWM signal enhancement E_{max}^m, however, correspondingly undergoes a larger decrease. No indefinite improvement in the performance of the converter can therefore be achieved by maximizing $\Gamma A\Delta\bar{N}L$. Instead, this quantity should be optimized to achieve the largest bandwidth for which the conversion efficiency remains larger than a given threshold (e.g. large enough to support error-free wavelength conversion in a given link); for instance this can be simply accomplished by properly selecting the input pump power ($|\Delta N|$ increases with the optical power as confirmed by Eq. (7.7)). This is illustrated in Fig. 7.6, where the circles and the continuous lines are, respectively, experimental and theoretical values of $\delta\omega_L^m$ and E_{max}^m/E_{min}^m (the peak-to-valley ratio of the resonance) versus the input power P_p^{in} (the parameter values used in this simulation are the same as those used for Fig. 7.3; furthermore, for simplicity, here we replaced $P_{tot}(z)$ in Eq. (7.7) with its average along the laser axis).

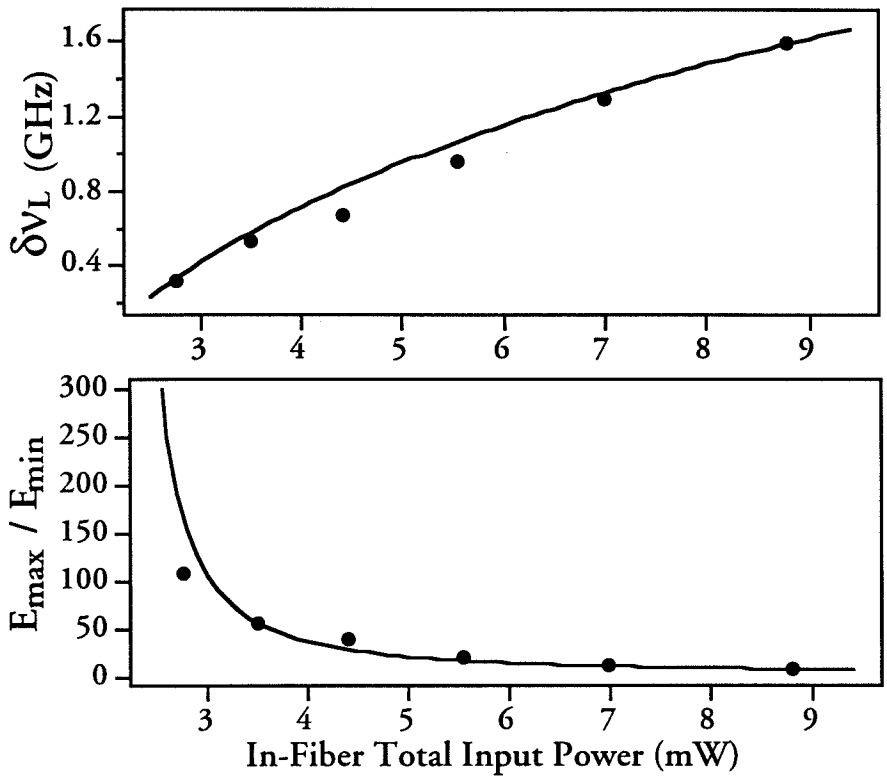

Figure 7.6: Spectral width (upper panel) and peak-to-valley ratio (lower panel) of the FWM injection-locking resonance centered at the frequency of the solitary laser output, versus total in-fiber input power (4 nm downshift). The continuous lines are theoretical fits to the model discussed in the text.

In conclusion then significant improvements over the experimental results presented here can be expected, mainly by maximizing the free spectral range. In the FBG coupled laser, this can be accomplished by writing the grating as close to the lensed fiber tip as possible, and by reducing its length. Furthermore, an on-chip DBR could be used instead, which should allow for an increase of $\Delta\omega_m$ by more than a factor of ten, and therefore make this device suitable for operation at 10 Gbit/sec. In particular a tunable DBR would be quite desirable for the additional flexibilty resulting from the tunability of the resonance wavelength.

7.5 ASE noise Power

In this Section, we will discuss the expression for the ASE noise power used in Section 7.3. The quantity P_{ASE}^{out} was defined there as the ASE power at the output of the self-pumped converter, in the frequency range $\Delta\nu_{det}$ (the resolution bandwidth of the spectrum analyzer used in our measurements) around the FWM signal frequency. It is given by

$$P_{ASE}^{out} = h\nu_s \Delta\nu_{det} C n^{-}(0) \tag{7.20}$$

where $n^{\pm}(z)\Delta\nu_{det}$ is the number of ASE photons traveling along the $\pm z$-direction in the laser active region, with frequency lying within the interval $\Delta\nu_{det}$ about ν_s.

In order to express P_{ASE}^{out} in terms of directly measurable parameters, we need to solve the boundary-value problem

$$\pm \frac{dn^{\pm}(z)}{dz} = \Big\{\Gamma g(P_{tot}(z)) - \gamma\Big\} n^{\pm}(z) + \Gamma\beta(P_{tot}(z))$$

$$n^{+}(0) = 0, \qquad n^{-}(L) = R_{HC} n^{+}(L) \tag{7.21}$$

where β is the spontaneous emission rate per unit length of the laser active region. The solution of Eqs. (20)-(21) can be written as

$$P_{ASE}^{out} = \frac{h\nu_s \Delta\nu_{res}\Gamma}{\sqrt{R_{BG}}} \left\{ \int_0^L dz\ \beta(P_{tot}(z)) \left[\frac{\sqrt{R_{HC}}G(L)}{G(z)} + \frac{G(z)}{\sqrt{R_{HC}}G(L)} \right] \right\} \tag{7.22}$$

where the two terms in square brackets refer to the ASE noise power emitted in the forward and backward directions respectively.

Finally, we need to characterize the dependence of β on the total optical power within the laser. First of all, recall that the following expressions are good approximations for semiconductor lasers (see, for instance, Section 3-3 of Ref. [23])

$$g(P_{tot}(z)) = g_M \Big[f_e(P_{tot}(z)) + f_h(P_{tot}(z)) - 1 \Big]$$

$$\beta(P_{tot}(z)) = g_M f_e(P_{tot}(z)) f_h(P_{tot}(z)) \tag{7.23}$$

where f_e and f_h are the occupation probabilities for the conduction-band electrons and the valence-band holes, respectively, evaluated at the transition frequency of interest, and g_M is a constant depending on a number of material parameters. Given the relation between the two Fermi functions, one can solve for β as a function of g. This is particularly simple for the case of compressively-strained quantum-well lasers, such as the device used in our experiments, because in this case the two Fermi functions are approximately equal, which leads to

$$\beta(P_{tot}(z)) = \frac{g_M}{4}\left[1 + \frac{g(P_{tot}(z))}{g_M}\right]^2. \tag{7.24}$$

Using Eq. (7.24) in (7.22), the ASE output power can be evaluated in a manner entirely analogous to the FWM efficiency calculation discussed in Section 7.3. This then gives the OSNR of the FWM signal, $OSNR \equiv \eta P_q^{in}/P_{ASE}^{out}$. It should be noted that we are assuming here that the optical filter used at the input of the converter is effective enough that the ASE power from the EDFA used to boost up the input signal can be neglected.

Bibliography

[1] H. Kuwatsuka, H. Shoji, M. Matsuda, and H. Ishikawa, *IEEE J. Quantum Electron.*, **33**, p. 2002, 1997.

[2] G. P. Agrawal, *J. Opt. Soc. Am. B*, **5**, P. 147, 1988.

[3] J. Zhou, N. Park, J. W. Dawson, K. J. Vahala, M. A. Newkirk, and B. I. Miller, *Appl.Phys. Lett.*, **63**, p. 1179, 1993.

[4] A. Uskov, J. Mϕrk, and J. Mark, *IEEE J. Quantum Electron.*, **30**, p. 1769, 1994.

[5] A. Mecozzi, S. Scotti, A. D'Ottavi, E. Iannone, and P. Spano, *IEEE J. Quantum Electron.*, **31**, p. 689–699, 1995.

[6] D. F. Geraghty, R. B. Lee, M. Verdiell, M. Ziari, A. Mathur, and K. J. Vahala, *IEEE J. Select. Topics Quantum Electron.*, **3**, p. 1146, 1997.

[7] M. A. Summerfield, and R. S. Tucker, *IEEE Photon. Technol. Lett.*, **8**, p. 1316, 1996.

[8] A. D'Ottavi, F. Girardin, L. Graziani, F. Martelli, P. Spano, A. Mecozzi, S. Scotti, R. Dall'Ara, J. Eckner, and G. Guekos, *IEEE J. Select. Topics Quantum Electron.*, **3**, p. 522, 1997.

[9] G. Hunziker, R. Paiella, A. D'Ottavi, P. Spano, R. Dall'Ara, G. Guekos, and K. J. Vahala, *Optical Fiber Communication Conference*, San Jose, California, 1998, paper WB7.

[10] A. E. Kelly, D. D. Marcenac, and D. Nesset, *Electron. Lett.*, **33**, p. 2123, 1997.

[11] D. D. Marcenac, D. Nesset, A. E. Kelly, M. Brierly, A. D. Ellis, D. G. Moodie, and C. W. Ford, *Electron. Lett.*,**33**, p. 879, 1997.

[12] S. Diez, C. Schmidt, R. Ludwig, H. G. Weber, K. Obermann, S. Kindt, I. Koltchanov, and K. Petermann, *IEEE J. Select. Topics Quantum Electron.*, **3**, pp. 1131, 1997.

[13] D. Nesset, M. Tatham, and D. Cotter, *Electron. Lett.*, **31**, p. 896, 1995.

[14] K. J. Vahala, R. Paiella, and G. Hunziker, *IEEE J. Select. Topics Quantum Electron.*, **3**, p. 698, 1997.

[15] G. Hunziker, R. Paiella, M. Ziari, A. Mathur, and K. J. Vahala, *IEEE Photon. Technol. Lett.*, **9**, p. 1352, 1997.

[16] R. Paiella, G. Hunziker, M. Ziari, A. Mathur, and K. J. Vahala, *Optical Fiber Communication Conference*, San Jose, California, 1998, paper WB8.

[17] R. Paiella, G. Hunziker, M. Ziari, A. Mathur, and K. J. Vahala, to be published in the *IEEE Photon. Technol. Lett.*.

[18] R. Lang, *IEEE J. Quantum Electron.*, **18**, p. 976, 1982.

[19] F. Mogensen, H. Olesen, and G. Jacobsen, *IEEE J. Quantum Electron.*, **21**, p. 784, 1985.

[20] N. Schunk and K. Petermann, *IEEE J. Quantum Electron.*, **22**, p. 642, 1986.

[21] K. Weich, E. Patzak, and J. Hörer, *Electron. Lett.*, **30**, p. 493, 1994.

[22] L. Li and K. Petermann, *IEEE J. Quantum Electron.*, **30**, p. 43, 1994.

[23] W. W. Chow, S. W. Koch, and M. Sargent, III, *Semiconductor-Laser Physics.* Berlin, Germany: Springer-Verlag, 1994.

Chapter 8

Logic gates

8.1 Introduction

Wavelength conversion is becoming a useful and important tool in a WDM network [1], but it is only the first step in creating a "smart" optical communication layer. Cross-phase modulators for instance have been recently shown to be very effective all-optical 2R and 3R signal regenerators [2]. All-optical packet header recognition and routing has also been demonstrated [3]. Logic gates are the focus of an intense research effort and a number of paradigms have been proposed; a spectacular demonstration has recently been done at 100 Gb/s by researchers from MIT [4]. The idea behind most of these efforts is to move some of the low-level and high speed information processing and routing to the optical layer. Time-division multiplexed systems are of course the candidates of choice to implement these ideas because the very high bit rates make electronics a difficult and costly alternative.

Byte-wide transmission on multiple wavelengths has been investigated as a single

physical channel optical bus [5]. To perform optical logic operations on such a bus has the great potential of combining parallel processing with very high speed gates. In this Chapter, I will show how four-wave mixing can be used in this context as an ultrafast conditional test for byte-wide WDM logic gates. A logic AND gate based on the polarization properties of the four-wave mixing has been proposed and demonstrated previously [6], but it processed two information channels encoded on the *same* wavelength. The scheme proposed here has the advantage that it can be easily extended to *any* logic function of two inputs, encoded on different WDM channels.

8.2 Operation of the logic gates

In our paradigm, the wavelength designates the bit position within the overall binary word in a multi-wavlength fiber optic bus, and the polarization of the signal at a given wavelength is used to specify the logic state of each bit. For instance, the binary word 1001 1100 would be encoded on an 8-wavelength bus (in a single fiber) as follows : λ_1^{TM}; λ_2^{TE}; λ_3^{TE}; λ_4^{TM}; λ_5^{TM}; λ_6^{TM}; λ_7^{TE}; λ_8^{TE}. In general, on-the-fly logic operations on such a binary word are performed using a combination of waveplates and four-wave mixing elements. The most straightforward operation is the logical NOT, which simply consists of a half-wave plate or a polarization mode converter. In more sophisticated gates, four-wave mixing is used to test for polarization coincidence of signals at different wavelengths, and provides new signals which can be used to confirm the coincidence. Direct mixing of polarization modulated signals will not maintain the coding format, since 'no signal' is not a logic state, and therefore the

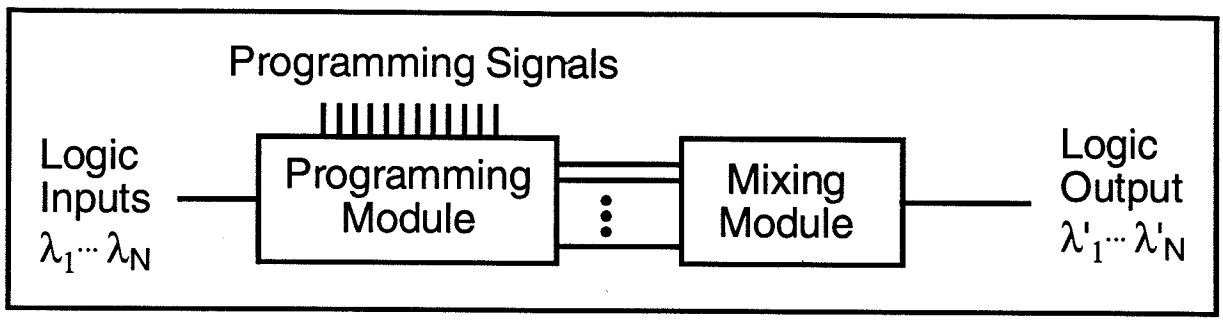

Figure 8.1: Generic gate architecture consisting of a programming module and a mixing module. The programming module consists of a series of linear optical devices, including wavelength demultiplexers, waveplates and polarizers (and possibly linear optical amplifiers). The figure also shows the dynamic gate reconfiguration possibility, through programming signals. The mixing module performs the conditional test function, and consists of SOAs as well as EDFAs at this point.

inputs to the mixers must be programmed to generate a polarization encoded logic outcome. This can be done with cascaded couplers and polarization elements. Since the timescale for the FWM signal generation is negligibly small, these gates impose practically no intrinsic limitation on the bit rate of the incoming signals.

The generic logic gates consist of a programming module followed by a mixing module, as shown in Fig. 8.1. In the programming module, the wavelength and polarization of the input waves are separated and prepared in such a way that the mixing processes occurring in the second module generate new signals polarized according to the truth table of the desired logic function. The programming module performs very simple tasks on the input waves, typically it consists of wavelength demultiplexers

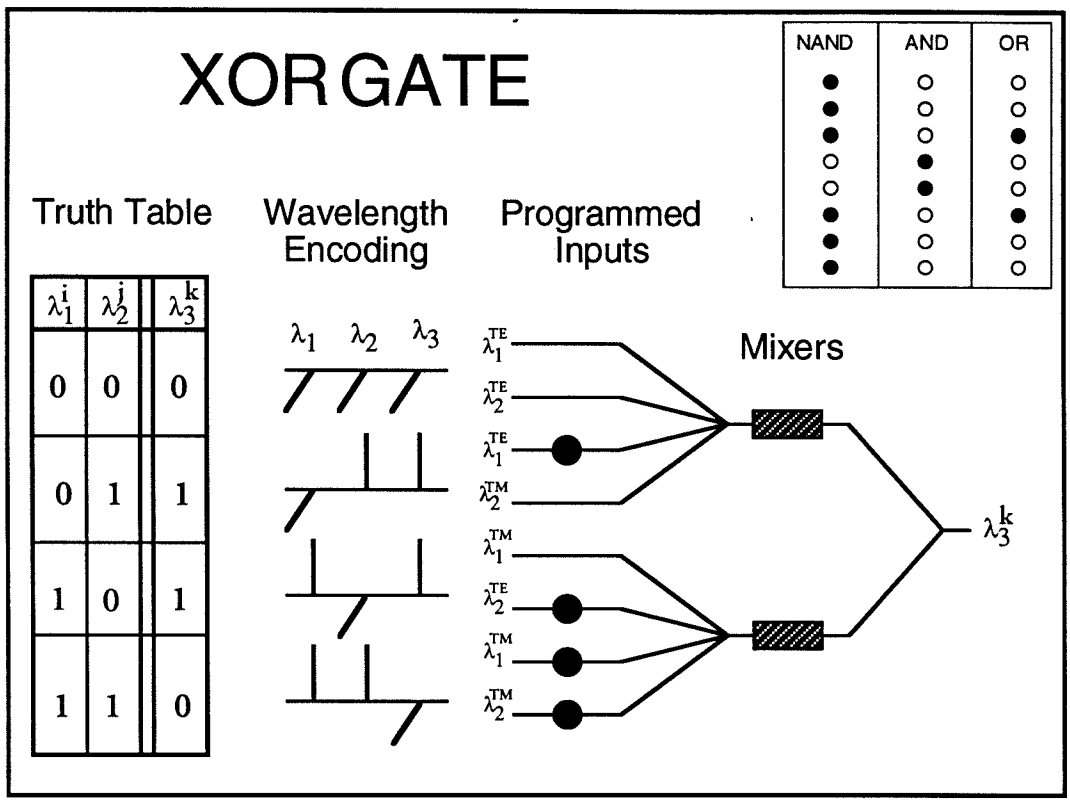

Figure 8.2: Schematic of a two-input XOR gate. The inset shows where the waveplates needed for other logical functions.

and polarization control elements. In future versions of these gates, it is therefore possible to envision a dynamically reconfigurable programming module, where the task performed by the gate can be reassigned, by controlling the module with either optical or electrical signals.

To see how a simple gate works, let's examine the case of a two-input XOR gate, schematically shown in Fig. 8.2. In the programming module, we first decompose the two input waves according to wavelength and polarization into the four possible input

states: $\lambda_1^{TE}\lambda_2^{TE}$, $\lambda_1^{TE}\lambda_2^{TM}$, $\lambda_1^{TM}\lambda_2^{TE}$, $\lambda_1^{TM}\lambda_2^{TM}$. The polarization states for these pairs must then be rotated so that the four-wave mixing product gives the corresponding outcomes for the XOR function, namely λ_3^{TE}, λ_3^{TM}, λ_3^{TM}, λ_3^{TE} respectively. The positions for the polarization rotators (half-wave plates at 45 degrees) are shown as black dots in the figure. These new polarization states are then combined and fed to the mixing elements. The four input cases are separated into two subgroups, and a separate mixing element is necessary for each of the subgroups. The pairing of the different input states to a given mixer can be somewhat different depending on the function to be implemented. Two mixers are however sufficient to implement all the two-input logical functions.

8.3 Experimental demonstrations

In order to demonstrate the feasibility of these logic gates, we have experimentally tested the operation of the different components of an XOR gate. We have separately tested the 3 key elements of this gate, namely the signal source (a 2.5 Gb/s polarization modulator), the programming module (a custom designed silica on silicon integrated photonic chip) and the mixing module (two polarization-insensitive SOAs).

8.3.1 The signal generator

To generate the polarization encoded signal, we used a $LiNbO_3$ Mach-Zehnder modulator with polarization maintaining (PM) fibers pigtailed to both outputs of the

interferometer. The light is coupled into the slow axis of the fiber so that the electric field vector joins the stress members next to the core. Both outputs were spliced to the input arms of a fiber polarization combiner. One of these splices was rotated by 90in the orthogonal polarization states of the same fiber after the polarization combiner. For the bits to be synchronized, it is very important that the optical path length between the Mach-Zehnder modulator and the polarization combiner is exactly the same for the data and the data-bar outputs.

The layout of the signal generator and the test setup are schematically shown in Fig. 8.3. To verify the performance of the modulator, we used a polarizer to select either the data or the data-bar states for detection. The bit-error rates were measured as usually, using the optically preamplified receiver described in the previous chapters.

There are two critical settings for this experiment. The first is the operating point of the Mach-Zehnder, and the other is the angle of the polarizer selecting the data or the data-bar states. The operating point of the Mach Zehnder needs to be set precisely at the 50/50 point so that the data and data-bar states are properly separated into the two outputs. This is done by measuring the total power at the output of the modulator, without polarizer. The polarizing splitter has 10% higher losses for the fast polarization mode, and thus the total output power of the modulator changes slightly as a function of applied voltage to the Mach-Zehnder. This is used to identify the transmission curve of the modulator, and knowing that, it is possible to align the polarizer to the fiber axis. With this alignement, the bit error rates become very stable even when the fibers are moved. There are many possible settings for the

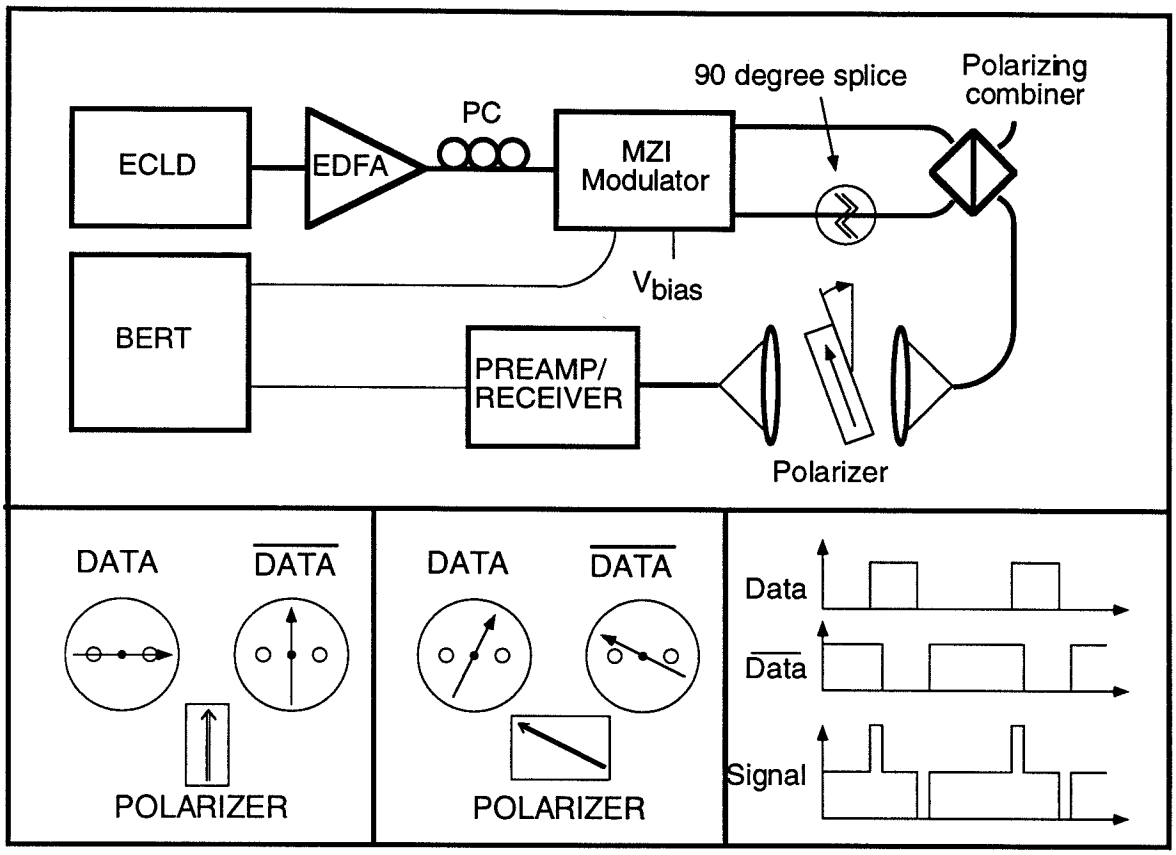

Figure 8.3: Layout of the signal generator and of the setup used to verify its operation. The left inset in the lower part of the figure shows schematically the polarization states for a properly aligned system, the middle inset shows an example of unstable polarization states, and the right inset shows the effect of bad signal timing in conjunction with misaligned polarizer (this is used to measure the difference in path length of the data and data-bar signals).

Mach-Zehnder operating point and the polarizer angle, but only one is stable and corresponds to the data and data-bar light propagating exactly along the eigenmodes of polarization of the fiber. Non-stable settings are usefull to measure the timing offset between the two output ports of the modulator. This is illustrated in the lower right inset of Fig. 8.3, where non-syncronized data and data-bar streams are shown as well as the resulting signal interference spikes (or dips) in the overlap region (this measurement is done with a misaligned polarizer collecting both components of the data).

Using this alignment scheme, we measured the sensitivity at the 10^{-9} error to be -35 dBm. This is high compared to the ideal case of -48dBm [7], and is attributed to the timing offset between the data and data-bar states (measured to be 100 ps or a fourth of a bit length) and the position offset of the polarizer relative to the fiber eigenaxis of polarization. Using an in-fiber-polarizer and fine-tuning the optical path lengths should significantly improve the sensitivity.

8.3.2 The programming module

The function shown in Fig. 8.2 has been implemented in a fully integrated planar photonic waveguide circuit shown in Fig. 8.4. The input is first split into two equal arms with a bi-directional coupler. Each side has a temperature-tunable Mach-Zehnder interferometer to split the WDM wavelength channels (the free spectral range is 250GHz), followed by the appropriate polarization elements (not visible in the mask) and two recombiners. In order to test the operation of this chip for its wavelength and polarization response, we used the signal generator from Fig. 8.3 with the laser turned

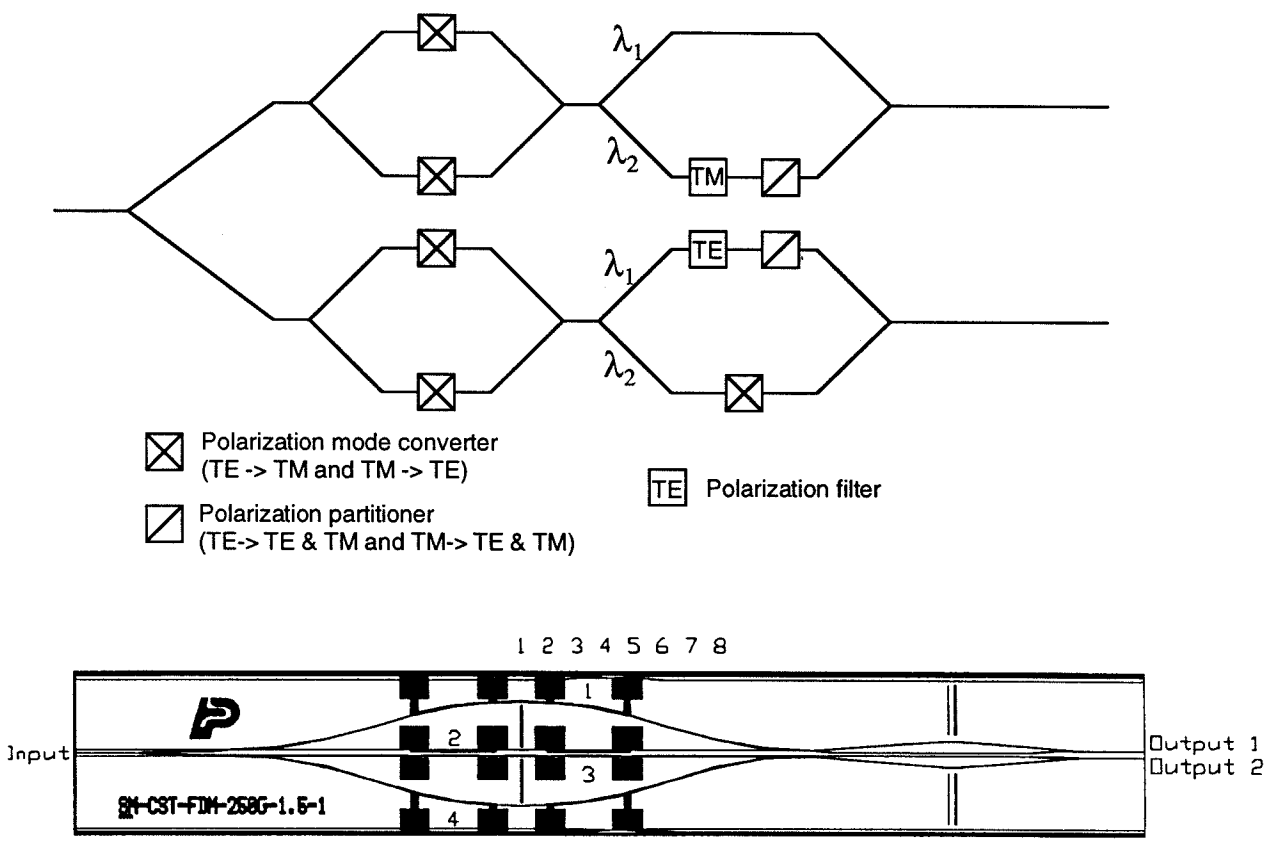

Figure 8.4: Top: Schematic of the programming implementation of the XOR gate. The input is fist equally divided in a biriectionnal coupler, followed by the wavelength demultiplexers (Mach-Zehnder interferometers with polarization mode converters to achieve polarization independent demlutiplexing). Then, each wavelength arm has polarization filters and rotators according to the programming table of Fig. 8.2. Bottom: Mask layout of the photonic integrated waveguide chip. The black square are the connections to electrical heating pads used to adjust the wavelength position of the demultiplexers. The vertical lines indicate the positions of the grooves into which the polarization elements are inserted.

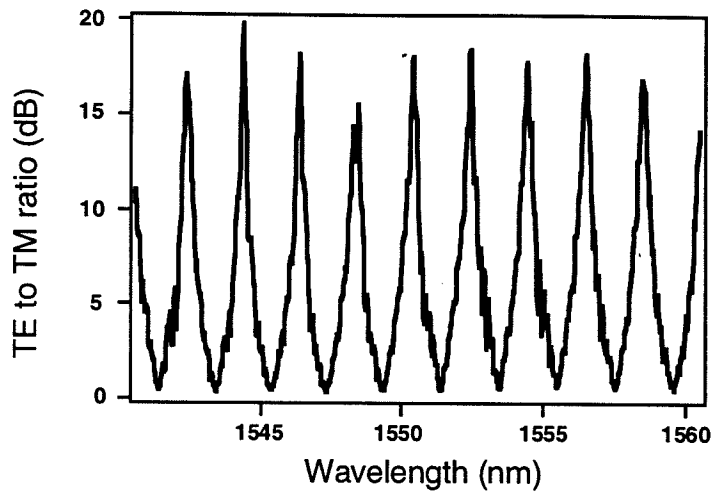

Figure 8.5: Relative amounts of light transmitted through the programming chip for TE and TM polarized input light. The peak to valley ratio is the measure of the polarization suppression, and the transmission at a valley is a measure of the power balance for the two programming paths.

off. The broadband ASE noise from the EDFA covered the entire wavelength range in one scan. The voltage of the Mach-Zehnder was used to select the polarization state of the noise. The spectrum at the output of port 1 is shown in Fig. 8.5, confirming the operation of the chip and a good polarization suppression of the polarizers (15-20dB).

8.3.3 The mixing module

In a preliminary experiment, we have also tested the mixing operation of the XOR gate by implementing it in the simple way shown in Fig. 8.6. Notice that we did not use polarization maintaining wave guides in this experiment; as a result, we could not obtain the required polarization components at the input to each SOA by simply inputting to the gate TM (λ_1^{TM} and λ_2^{TM}) and TE (λ_1^{TE} and λ_2^{TE}) waves followed by

polarization rotators. Instead, we used the polarization controllers shown in figure 8.7 (each of which is labeled by the polarization state that it is set to produce at the SOA input). Furthermore, due to limited availability of components, only one of the input signals (X_1, of wavelength λ_1) was modulated with digital information. This signal was provided by an externally modulated distributed feedback laser. The modulator was a dual-output Mach-Zehnder interferometer, whose two output ports provide the modulating signal and its complement. It was driven by a Hewlett-Packard bit error rate tester with a preset bit pattern (at 2.5 Gb/sec). On the other hand, the other input signal (X_2, of wavelength λ_2) was constant and set first to a logical one and then to a logical zero. In the former case, the XOR truth table requires that the output signal Y be the complement of X_1; in the latter case that $Y = X_1$. The results of this experiment are shown in figure Fig. 8.6.

The upper trace is the preset bit pattern (10011100) encoded on the input signal X_1, measured with a Hewlett-Packard microwave transition analyzer. The middle trace corresponds to the case $X_2 = 1$ and shows the four-wave mixing signal generated in SOA 1, which in this case is the TM component of the overall output wave of the XOR gate. As such, this trace gives the output signal Y (given that TM is interpreted as a logical one). Consistent with the truth table, we indeed find it to be the complement of X_1. Similarly, the lower trace gives Y for $X_2 = 0$ (i.e. the four-wave mixing signal from SOA 2 in this case), which can be seen to be equal to X_1, again as required by the truth table. The SOAs used in the experiment have only a small-signal gain of approximately 10 dB, which results in a low four-wave mixing

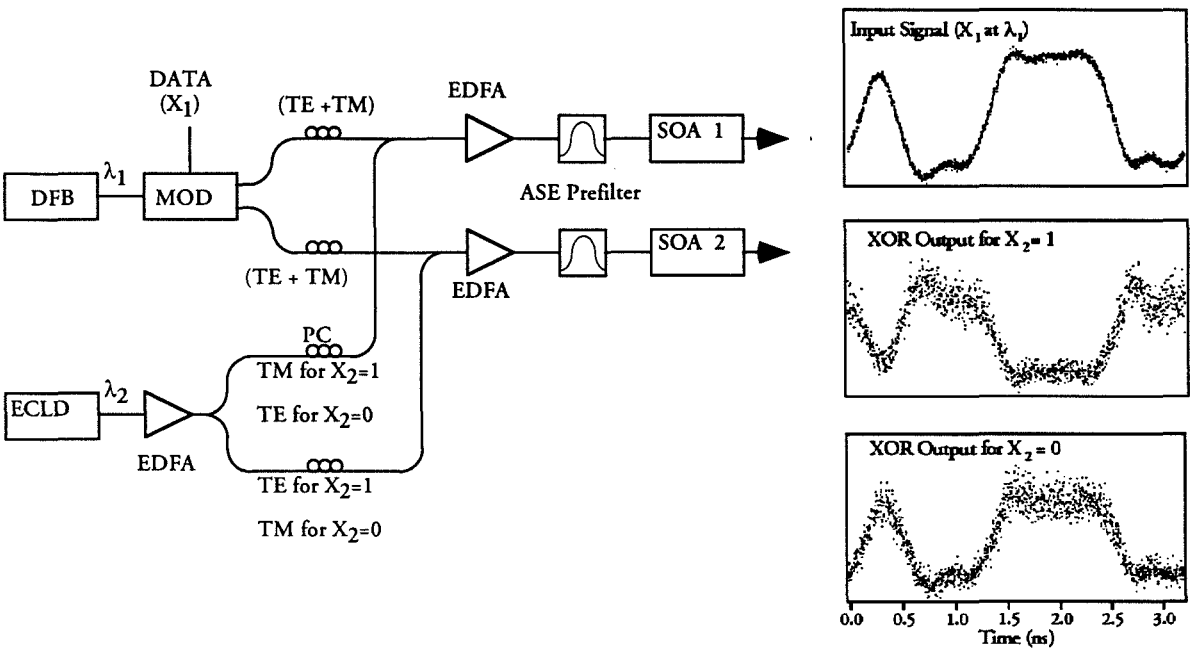

Figure 8.6: Experimental layout of the preliminary XOR gate demonstration and outputs from the mixers.

conversion efficiency; this explains the additional noise on the lower two traces. We emphasize that this is only a preliminary demonstration.

8.4 Practical issues

To be of any use, space requirements of these gates will obviously have to be reduced from the current one optical table per logic gate! All the optical processing involved in the logic operation is integrable on a photonic waveguide circuit, hence the implementations of the gates can be monolithic and compact. They will require on-chip polarizers, wavelength taps, amplifiers and mixers. The easiest implementation of the linear part involving polarization control wavelength separation and signal amplification can be done with glass-based materials, namely silica on silicon waveguides. This technology is reviewed in [8], implementations of polarization mode conversion are covered in [9], promising amplifier performance (4.1 dB/cm gain with only 21 mW of pump power) has been reported recently [10] and finally, ASE pre-filtering can be done with Bragg gratings [11]. Most of this technology is now commercially available (except for on-chip amplifiers). The mixing components are best implemented with SOAs, for their compactness as well as for the fast and strong optical non-linearity.

Other important issues are : the bit skew on the wavelength bus due to group-velocity dispersion, the necessity of using polarization maintaining fiber, and the polarization walk-off between the zero and one states for given bit in the information channel. The group velocity dispersion and its consequence on the clock offset between WDM channels was a serious concern in the estimate for the aggregate bit-

rate of a byte-wide WDM system [5]. More recently however, dispersion management technologies have been made widely available, and a dispersion compensating schemes based on chirped fiber Bragg gratings or dispersion managed fiber can be used to cancel the bit walk-off within the WDM byte. The necessity for PM fiber is certainly a disadvantage of the scheme presented here. The implementation will require either replacing fibers or managing polarization changes due to the environment, as was recently demonstrated in [12]. Finally the polarization walk-off between logical zeros and ones needs to be addressed. Since the polarization eigenmodes propagate at different speeds in PM fiber, the zero states need to be re-syncronized with the one states after propagating trough the fiber. For the PM fiber we used in our experiments (Panda fiber from Fujikura), the polarization beat length is 3.5 mm. At 2.5 Gb/s, this means that after propagating for 180 m the walk-off equals a full bit length. As solution to this problem is to perform an inversion (logical NOT) in the middle of each fiber segment and before entering the next gate. Inversions can be done by simply splicing the fiber at 90 degrees, so that the fast axis becomes slow and conversely.

Bibliography

[1] A. Jourdan, P. Doussiere, D. Leclerc, S. Gurib, F. Masetti, C. Joergensen, T. Durhuus, B. Mikkelsen, S. Danielsen, *Fiber and Integrated Optics*, **15**, pp. 942, (1996)

[2] B. Lavigne, D. Chiraoni, L. Hamon, C. Janz, A. Jourdan, *OFC'98 Proceedings*, Paper ThO7, San Jose California (1998)

[3] J. K. Lucek, *Optics Communications*, **126**, pp. 143, (1996)

[4] K. L. Hall and K. A. Rauschenbach, *OFC'98 Proceedings*, Post-deadline Paper PD5, San Jose California (1998)

[5] M. L. Loeb and G. R. Stilwell, *Journal of Lightwave Technology*, **6**, No. 8, pp. 1306, (1988)

[6] D. Nesset, M. Tatham, D. Cotter, *Electronics Letters* **31**, No. 11, pp. 896, (1995)

[7] E. Desurvire, *Wiley Interscience*, (1994).

[8] M. Kawachi, *IEE Proceedings in Opto-electronics*, **143**, No. 5, pp. 257, (1996)

[9] Y. Inoue, Y. Ohmori, M. Kawachi, S. Ando, and T. Sawada, *IEEE Photonics Technology Letters*, **6**, No. 5, pp. 626, (1994)

[10] Y.C. Yan, A. J. Faber, H. de Waal, P. Kik and A. Polman, *Appl. Phys. Lett.*, **71**, No. 20, pp. 2922, (1997)

[11] Y. Hibino, T. Kitagawa, K. Hill, F. Bilodeau, B. Malo, J. Albert, and D. Johnson, it IEEE Photonics Technology Letters, **8**, No. 1, pp. 84, (1996)

[12] T. Ono, *OFC'98 Proceedings*, Invited Paper FE4, San Jose California (1998).

Glossary

ASE: Amplified spontaneous emission

BER(T): Bit error rate (tester)

BPF: Bandpass filter (same as OBF)

CDP: Carrier density pulsation (same as carier density modulation)

CDM: Carier density modulation (same as carrier density pulsation)

CH: Carrier heating

DBR: Distributed Bragg reflector laser

DFB: Distributed feedback laser

ECLD: External cavity (tunable) laser diode

EDFA: Erbium doped fiber amplifier

EDFRL: Erbium doped fiber ring laser

EXOR: Exclusive OR, same as XOR

FWM: Four-wave mixing

LO: Local oscillator

MOD: Modulator

MZI: Mach-Zehnder Interferometer

NRZ: Non return to zero (data modulation format where the signal does not vanish in between bits of information)

MTA: Microwave transition analyzer (a very fast digital oscilloscope)

OBF: Optical bandpass filter (same as BPF)

PBS: Polarization beam splitter

PRBS: Pseudo-random bit stream

PC: Polarization controller

PF: Polarization filter (same as a polarizer)

PIN: Photodiode : p-n junction diode with and intrinsic (undoped) light-absorbing layer inside the junction.

RFSA: Radio-frequency spectrum analyzer

SOA: Semiconductor optical amplifier

SHB: Spectal hole burning

TE: Polarized light : $\vec{E}$ filed is perpendicular to growth axis (in the plane of the quantum wells)

TDM: Time division multiplexing (multiplexed)

WDM: Wavelength division multiplexing (multiplexed).